7-11-2013

EXPERIMENTAL CHARACTERIZATION AND MODELING OF ASPECT-RATIO-DEPENDENT DIFFUSION OF NANOCRYSTALS IN NANOCHANNELS

Louis Tribby

Louis J. Tribby
Candidate

Chemical and Nuclear Engineering
Department

This dissertation is approved, and it is acceptable in quality and form for publication:

Approved by the Dissertation Committee:

Sang M. Han , Chairperson

Steven R. J. Brueck

Frank van Swol

Cornelius F. Ivory

EXPERIMENTAL CHARACTERIZATION AND MODELING OF ASPECT-RATIO-DEPENDENT DIFFUSION OF NANOCRYSTALS IN NANOCHANNELS

By

Louis J. Tribby

B. S., Chemical Engineering, University of New Mexico, 2005

DISSERTATION

Submitted in Partial Fulfillment of the
Requirements for the Degree of

Doctor of Philosophy
Engineering

The University of New Mexico
Albuquerque, New Mexico
May, 2013

ACKNOWLEDGEMENTS

Naturally, I have many people to acknowledge throughout my life in the sciences and in particular to this doctorate of engineering. First, I have to thank my mentor, Dr. Sang M. Han, for his patience, guidance, wisdom, and his devotion to his students. Secondly, I have to thank my parents, Richard Tribby and Elizabeth Witte, for bestowing life upon me and providing the guidance, vision, and opportunities that I hope to one day bestow on my children.

Next, I would like to thank my dissertation committee for taking the time and interest in my research, your insight is greatly appreciated. I would also like to thank some people that I have had the pleasure of working with throughout the years: Henry Gerung, Youn-jin Oh, Darin Leonhardt, Josephine Sheng, and Swapnadip Ghosh. You guys have always provided different insights into research topics, and as a result have broadened my general knowledge of science and engineering.

EXPERIMENTAL CHARACTERIZATION AND MODELING OF ASPECT-RATIO-DEPENDENT DIFFUSION OF NANOCRYSTALS IN NANOCHANNELS

By

Louis J. Tribby

ABSTRACT OF DISSERTATION

Submitted in Partial Fulfillment of the
Requirements for the Degree of

Doctor of Philosophy
Engineering

The University of New Mexico
Albuquerque, New Mexico

May, 2013

ABSTRACT

The investigation of aspect-ratio-dependent diffusion and equilibrium partitioning of semiconductor nanocrystals in rectangular nanochannels has been undertaken. The nanocrystals are terminated with hydrocarbon ligands and suspended in toluene, considered an aprotic solvent. Time-dependent concentration profiles are measured as a function of distance from the channel entrance by the calibrated fluorescence intensity of the nanocrystals. Both the forward diffusion of the nanocrystals and their reverse diffusion are characterized. Nanocrystals are first allowed to diffuse forward from a reservoir into the nanochannels over a long period ($\geq$ 3 days) until the inlet concentration reaches a steady state. Subsequently, these nanocrystals are allowed to diffuse out, in reverse, from the nanochannels back into the reservoir that is filled with neat toluene. The experimentally observed concentration profiles during forward diffusion are compared to the profiles resulting from a continuum transport model accounting for diffusion and wall-adsorption of nanocrystals.

The transport model provides estimates on the diffusion constant, equilibrium coefficients, and the adsorption/desorption rate constants. For the aspect ratios ranging from 1 to 6, the observed concentration within the nanochannels is significantly higher ($\geq \times 4$) than the initial bulk concentration within the reservoir, indicating wall adsorption of nanocrystals. Despite the significant level of fluorescence intensity originating from the wall adsorbed NCs, the fractional surface coverage of nanocrystals remains below 1 monolayer. Using a two-site adsorption model, the diffusion constants from the forward diffusion profiles range from 10^{-8} to 10^{-9} cm^2 s^{-1}, while the adsorption rate coefficients range from 0.36 to 1.60 ($x10^{-15}$ cm^2 s^{-1}). In general, we observe an attractive van der

Waals force between the NCs and the channel walls that allows for a reversible wall adsorption that strongly affects the apparent diffusion of NCs within nanochannels.

TABLE OF CONTENTS

LIST OF FIGURES

LIST OF TABLES

CHAPTER 1 INTRODUCTION

1.1 Semiconductor Nanocrystals

Semiconductor nanocrystals (NCs) have found numerous applications in both physical and life sciences. Much of the scientific attention stems from their unique optical and electronic properties that are a function of their size and shape. For macroscopic semiconductor materials, a constant band gap or energy gap between the valence band and conduction band exists due to the overlap of numerous atomic energy states. For quantum confinement within a sufficiently small NC, the quantized energy levels are proportional to the number of atoms within the NC. Thus, the band gap for a NC can be directly tuned by the size of the NC. By changing the size of the NC, the variation in the band gap energy results in a corresponding variation of the emitted photonic energy when the excited electron recombines with a valence hole, see Figure 1-1(A) for a process diagram. The resulting photonic emission can be experimentally observed for the cadmium selenide semiconductor NC system, shown in Figure 1-1(B).

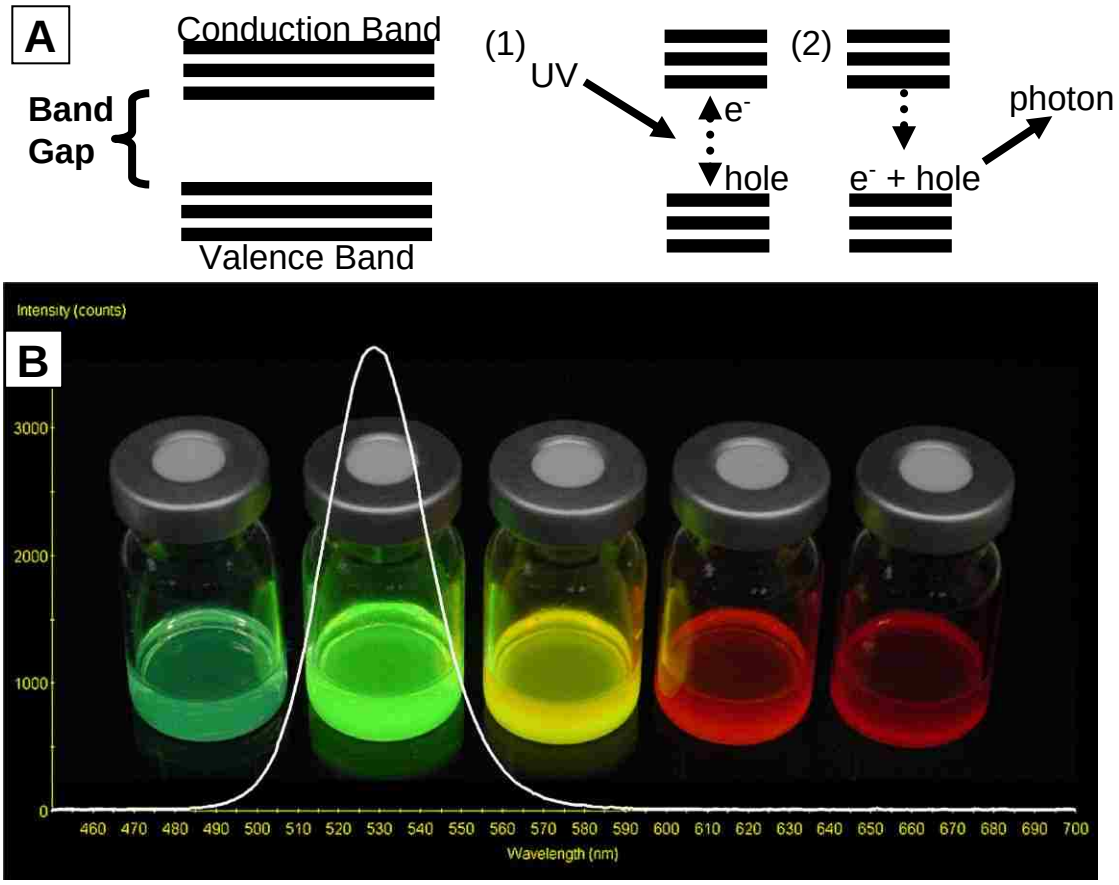

Figure 1-1. (A) A process diagram illustrating: (1) the UV excitation resulting in the electron and hole to split, with the electron promoted to the conduction band while the hole remains in the valence band, (2) the decay of an electron to the valence band that pairs with a hole, resulting in the emission of a photon. (B) The emission properties of small CdSe NCs under a general UV excitation source. The far left container has the smallest NCs while the far right container has the largest NCs. An overlay of the emission wavelength (white line) for the second container of CdSe NCs is also shown.

During the early 1990's, solution-based synthesis routes to semiconductor NCs became widely reported, resulting in inexpensive and easily reproducible synthesis methods for scientists and engineers to utilize in developing novel applications. Some of the earliest work included the cadmium-selenium system, a II-VI semiconductor material, which was found to have size-dependent photoluminescence in the 500-700 nm range. Today, CdSe NCs are one of the most heavily researched semiconductor systems and are commercially available for a wide variety of applications.

Over the past two-decades, emphasis on controlling the nucleation and growth conditions for colloidal semiconductor NCs has evolved to include additional surfactants to alter the growth rates of specific crystallographic planes. Through the use of these surfactants and general conditions, a variety of shapes have been produced: spheres, teardrops, rods, tetrapods, and multi-armed tetrapods, see examples in Figure 1-2. Recently, the focus has been on increasing the quantum yield and robustness of the NCs by further modifying the NC's surface with additional semiconductor layers [1, 2], water-soluble ligands [3], or bio-linkers [4] and bio-agents [5, 6]. These surface modifications allow one to tailor the NC's desired properties for specific applications, thus giving NC's the flexibility to be used in a wide assortment of applications. As a result, semiconductor NCs serve as important materials for light-emitting diodes [7], photovoltaic devices [8], transistors [9, 10], sensors [11, 12], biological labels [13, 14], and fluorescent probes [15-17].

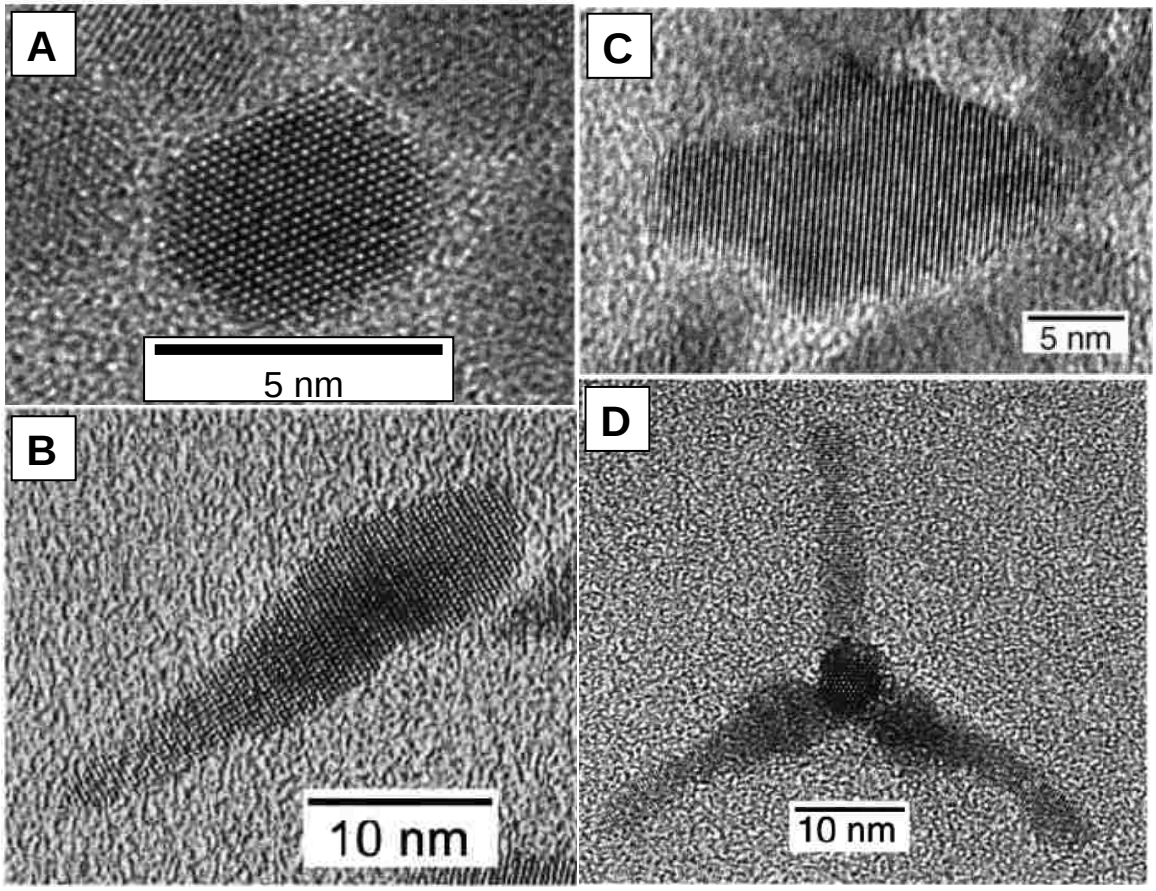

Figure 1-2. Several HR-TEM images of CdSe semiconductors that have a shape of: (A) faceted quantum dot, (B) tear drop, (C) arrow, (D) tetrapod [18].

1.2 Nanofluidics

Over the past decade, advancements in semiconductor-based fabrication techniques of uniform nanofluidic channels with one or more dimensions at or below 100 nm, has allowed for rapid progress in discovering unique nanofluidic phenomenon. Several key review articles summarize many of the nanofluidic transport phenomenon that have been experimentally identified and modeled [19, 20]. At the critical dimension of 100 nm, the channel's width is comparable to or smaller then the electric double layer. The electric double layer describes the charge region that naturally occurs around a solid

when it is placed into a liquid. A solid's surface charge can attract or repel ions that come near the surface resulting in electrostatic forces, and within a nanochannel creates a significant charge screening effect, see Figure 1-3.

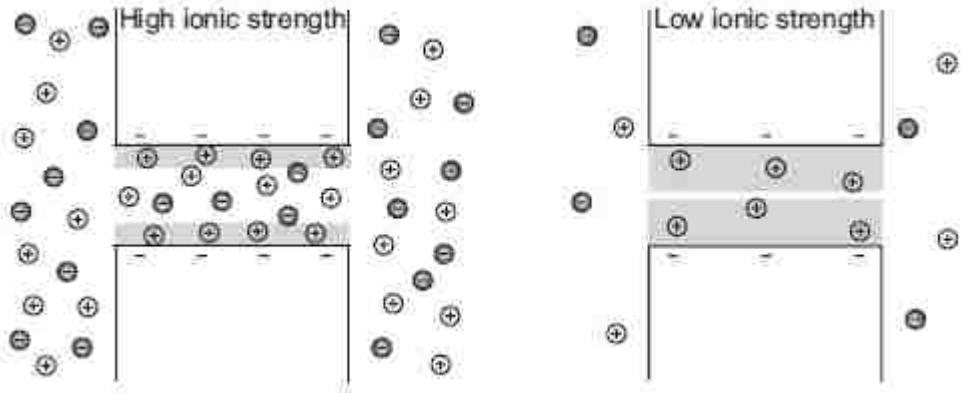

Figure 1-3. Shown in the two diagrams is a representation of the electric double layer (grey) for the situation of a high ionic concentration and low concentration. At low ionic concentrations the nanochannel is counter-ion selective [20].

Furthermore, by applying an external parallel electric field to the nanochannel, the movement of the ions adjacent to the surface provides a viscous drag, that results in a bulk liquid flow. For example, if the surface is negatively charged the positive ions on the surface will drag the liquid towards the cathode. This process is called electro-osmotic flow. In this same electric field, a molecule will experience electrophoresis, which moves the counter-ions on the molecule's surface creating essentially a polarized molecule. This polarization allows the molecule to have mobility opposite the direction of the electro-osmotic flow. By carefully selecting the systems conditions, selective particle and molecule transport can lead to a variety of separations and detection schemes.

Other methods of molecule and particle transport can be accomplished by shear-driven flow [21] or by an externally applied pressure [22, 23], although these processes become less effective at these scales.

To take full advantage of these unique nanofluidic capabilities, the integration into well-established microfluidic processing platforms like the lab-on-a-chip architectures, allows the coupling of multiple arrays of parallel nanochannels to provide both reasonable volumetric processing, enhanced chemical sensing and specificity [24]. As a consequence, the interest in developing nanofluidic devices to explore molecular confinement [25-27], single molecule detection [19, 24], and separation processes [28-31], has grown vastly in the past decade.

Today, there are many methods available to fabricate uniform fluidic channels with a critical diameter near or below 100 nm. Since conventional UV lithography equipment costs are substantially more expensive for sub-micron features, less-expensive approaches have been developed to fabricate nanochannels. Most top-down approaches use conventional UV lithography to pattern a photo resist layer to serve as a soft mask to accurately place where the final nanochannel(s) will be located. The soft mask can then be followed by an etching or deposition step to define the dimension of the nanochannel(s). For example, the fabrication steps for depositing a layer of amorphous silicon (aSi) at a height of 50 nm leads to a corresponding void between the two microchannels [32], as shown in Figure 1-4 (A1). Conversely, two common ways of etching materials to create a nanochannel is by wet etching or plasma etching. For example, many authors have used diluted hydrofluoric acid to wet etch a nano-trench into a SiO_2 layer [21, 26], where the etched channel's height is on the nanoscale while the

width is defined by the patterned photoresist mask. Once the photoresist mask is removed, the trench can be enclosed by bonding a pyrex cover slip to the surrounding material to complete the channel. Solution etching results in simultaneous lateral and perpendicular etching, making a closely packed array of channels very difficult to fabricate by wet etching techniques.

If a higher density of channels is needed, a periodic hard mask can be fabricated and then anisotropically plasma etched into the desired material, see Figure 1-4 (B1). Plasma etching an array of closely packed channels is preferred over wet etching because of the ability to vertically etch high aspect ratio channels while minimizing the lateral etching. However, plasma etching requires a much stronger mask to minimize the degradation of the original pattern. Metal hard masks are often sufficient in resisting the plasma etch chemistry and are easily produced by standard metal evaporation techniques.

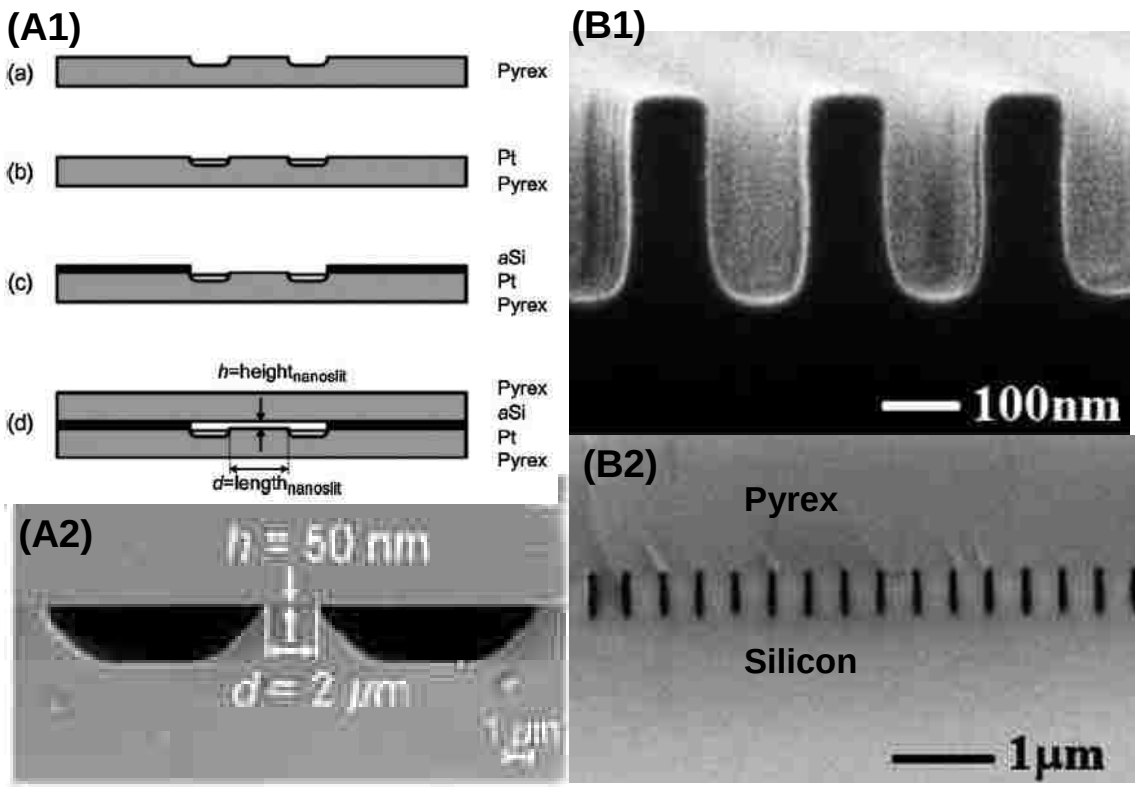

Figure 1-4. (A1) A cross-sectional diagram showing several fabrication steps for producing a 50 nm high spacer layer (aSi) between two parallel microchannels that are completed by bonding a pyrex cover slip. (A2) A cross-sectional SEM image showing the resulting microchannels that are bridged together by a nanochannel void. (B1) A cross-sectional SEM image showing the resulting anisotropically plasma etched array of silicon nanochannels [30]. (B2) The array of nanochannels is completed by bonding a pyrex cover slip.

There are many types of lithography capable of fabricating a hard mask that can be used to produce an array of nanochannels. Several lithography processes worth mentioning are scanning beam, edge or shadow-edge, and interferometric. Scanning beam lithography uses an electron beam to pattern the photoresist one-line at a time; this process is typically carried out on an SEM instrument and has a resolution below 50 nm. The downside of scanning beam lithography is the inherently slow processing times required to produce a sample. In shadow-edge lithography [33], conventional lithography can be used to produce a micro-featured topology on a substrate surface. The micro-features on the substrate are then angled during metal evaporation to produce much smaller nanoscaled metal lines. The edge of the micro-feature serves to block most of the evaporated metal from reaching the substrate's surface, thus resulting in a smaller width mask. The downside of this shadow-edge procedure is that the angle of deposition changes as a function of distance from the substrates' center point, resulting in non-uniform line widths across the wafer's surface.

Alternatively, interferometric lithography uses a coherent UV laser beam to pattern large areas of photoresist. The process requires that the laser beam is split into two beams, and then recombined by a mirror onto the photoresist surface. The constructive and destructive interference pattern is developed in the photoresist. Metal evaporation followed by a lift-off process allows a suitable hard mask for etching to be fabricated. This particular method allows for a wide range of pitches to be developed in the photoresist gratings, and allows for arrays with consistent features to be produced over large areas.

Several methods have been developed to further transfer and propagate the etched nano-features onto hard surface substrates or flexible polymer materials without having to repeat the previous fabrication steps. Nano-imprint lithography and nano-transfer printing are two processes that start with a master mold or stamp to reproduce the pattern in other substrates [34, 35]. Nano-imprint lithography can uses pressure-induced transfer of a rigid mold into a polymer film that further requires either a UV or heat source to cure the plastic, see Figure 1-5 (A). This process allows for large patterned areas to transfer in a single step, and has been able to reproduce feature sizes as small as 5 nm, see Figure 1-5 (B1 and B2). Nano-transfer printing is a technique that transfers a thin layer of material, typically a metal, on a master stamp to another substrate; see Figure 1-5 (C). The stamp may be either a hard or soft material, but the substrate typically requires a self-assembled monolayer of a receptor chemical group. In the case of transferring nano-patterned metals, a monolayer of dithiol works well to link the patterned layer of metal to the substrate, see Figure 1-5 (D1 and D2). A draw-back of this procedure is inherently in the use of the linking chemical layer and is not suitable for all applications.

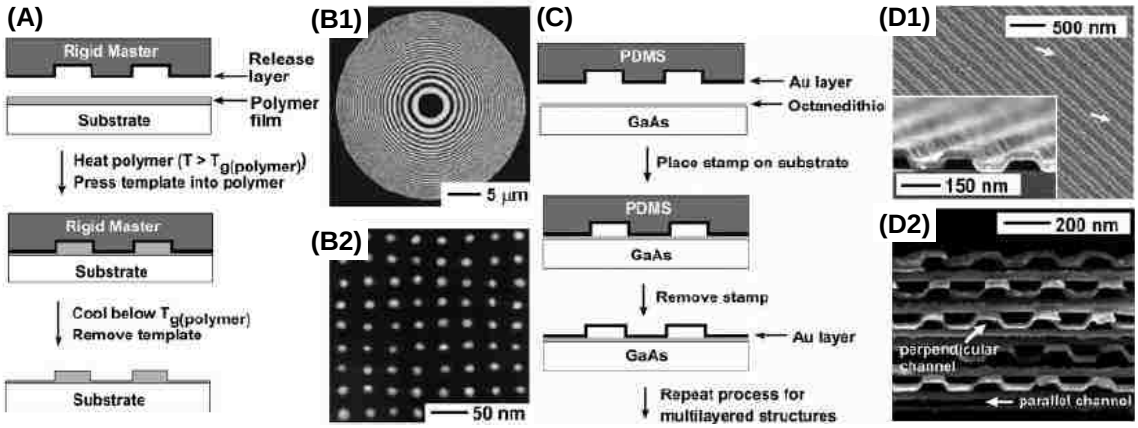

Figure 1-5. (A) A diagram of the steps for nano-imprint lithography. (B1) A reproduced Fresnel zone plate with a 125 nm minimum line width [36]. (B2) Metal dots with a 10 nm diameter and a periodicity of 40 nm. (C) A diagram of the steps for nano-transfer printing. (D1) A 20 nm gold layer transferred to a substrate functionalized with 1,8-octanedithiol. (D2) A multi-layer stack of gold with each 20 nm thick layer orientated perpendicular to the previous layer [37].

Additionally, a broader category of template techniques include: templated vertically grown nanotubes, coating and removal of a sacrificial template material [24, 38], or self-assembly processes that produce ordered nanochannel templates. Vertical growth of Si wires by chemical vapor deposition on gold templated nanodots, followed by a multi-step fabrication process that includes oxidation, polymer deposition, and several etching steps results in silica nanotubes that can be harvested for nanofluidic channels [39, 40], see Figure 1-6 (A1 and A2). Methods using a sacrificial structure to fabricate nanochannels typically rely on conventional deposition techniques to encase the sacrificial template nanomaterial that is later etched or thermally evaporated. For example, an electrospun polymer fiber can be drawn out to a diameter as small as 50 nm

and placed across a microchannel trench [24]. The fiber can then be coated by SiO_2, or other materials, by plasma enhanced chemical vapor deposition or sputter coating. The coated polymer is then thermally removed, leaving behind a hollow nanotube as shown in Figure 1-6 (B1 and B2). Alternatively, it has been found that the combination of liquid-crystal templating and self assembly by sol-gel processes can result in ordered nanochannels within a micro-structured silica particle [41, 42]. For example, if the silica is condensed on the interface of nematic liquid crystals, an array of open-ended silica nanochannels can form a larger hexagonally shaped fiber several microns in length, see Figure 1-6 (C1 and C2). Although, many of these templating techniques have been used to explore nanofluidics, there remains a concern of easily integrating these structures into microfluidic channels, or other devices, such that the process is amenable to manufacturing.

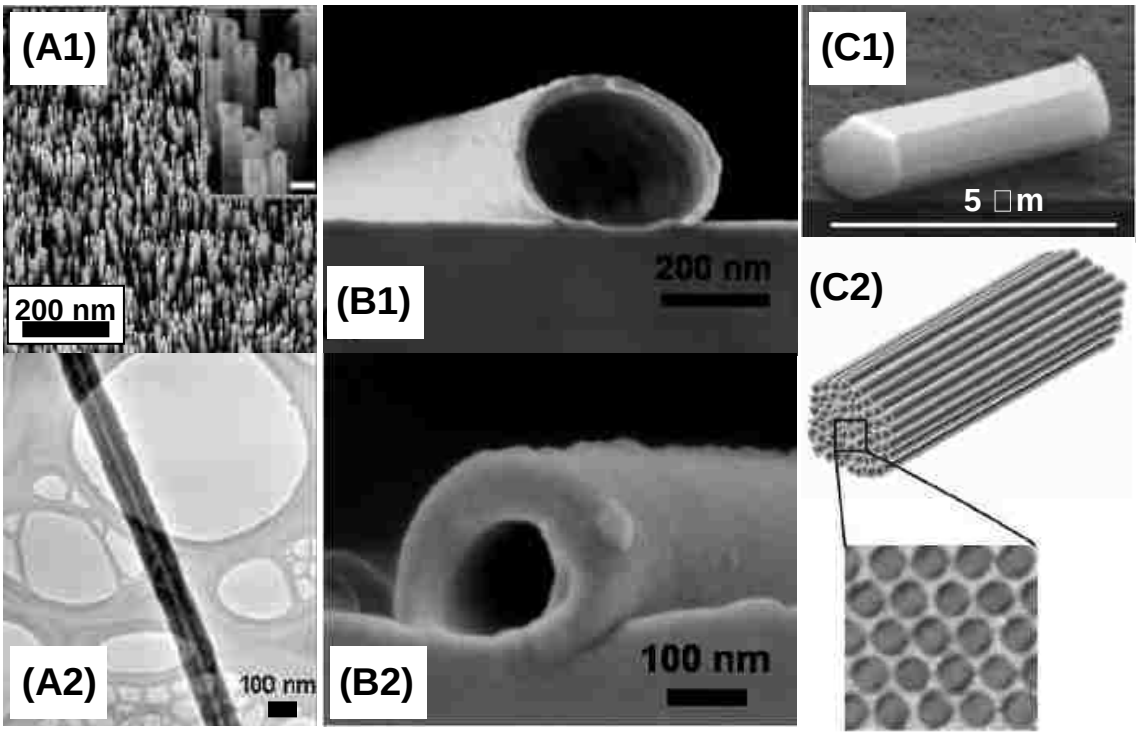

Figure 1-6. (A1) A SEM image of the final processed silica nanotubes that are originally synthesized from a chemical vapor deposition process [39]. The inset shows a higher magnification SEM image with a 100 nm scale bar. (A2) A TEM image of a silica nanotube on a holly carbon substrate. (B1) A cross-sectional SEM image of the resulting aluminum nanotube that was processed by Al evaporation onto an electrospun polymer fiber template [24]. (B2) A cross-sectional SEM image of the resulting PECVD glass channel that used the electrospun polymer fiber as a template. (C1) A SEM image of a single silica particle that was prepared by a templated sol-gel process that condensed silica on the interface of nematic liquid crystals [41]. (C2) A diagram showing the hexagonally packed array of silica nanochannels with a TEM image showing the channel periodicity of ~3.6 nm with individual channels having a diameter of ~2.9 nm.

1.3 Importance of Characterizing Diffusion within Nanochannels

Particle and molecular transport in nanochannels is largely characterized by their diffusive properties, especially in the absence of electrokinetic driving forces. Due to the large surface-to-volume ratio and limiting volume within nanochannels, diffusion becomes the dominant transport mechanism, rather than pressure-driven convective transport [21, 43]. Thus, many of the important nanoporous systems, such as molecular sieves [44], membranes [45, 46], templated mesoporous thin films [47, 48], nanoporous drug-delivery particles [49, 50], etched channels [27, 51], and carbon nanotubes [52-54], have all been characterized by their diffusive properties.

Although biological and physiological membrane transport processes have been observed and modeled before the 1970s, the more modern conceptual understanding of hindered diffusion wasn't constructed until later in that decade. Specifically, the seminal papers from Anderson *et al*. (1974) and Brenner *et al.* (1977) describe the rigorous hydrodynamic calculations of a Brownian solute molecule diffusing into a pore of a comparable size [55, 56]. Both of these papers were predicated on the mass transfer experiments of their time, which had propagated from the ability to produce uniformly sized straight pore membranes. It was revealed by Anderson *et al*.'s analysis of the upper limit of hindered diffusion for small radius ratios of particle to pore, that a considerable correction to the previously generalized centerline estimate for diffusion coefficients was warranted. Figure 1-7 shows the published correction that result from averaging the wall's frictional effect over all radial positions for a spherical particle. Brenner *et al.* soon relaxed many of their predecessor's strict conditions to produce a more generalized analysis for particles and molecules of arbitrary shape. Figure 1-8, shows the published

comparison of Brenner *et al.*'s analysis to Anderson *et al.*'s formulation for hindered diffusion. Brenner *et al.*'s analysis is the modern formulation of steric hindrance that is typically considered in nanofluidic experiments.

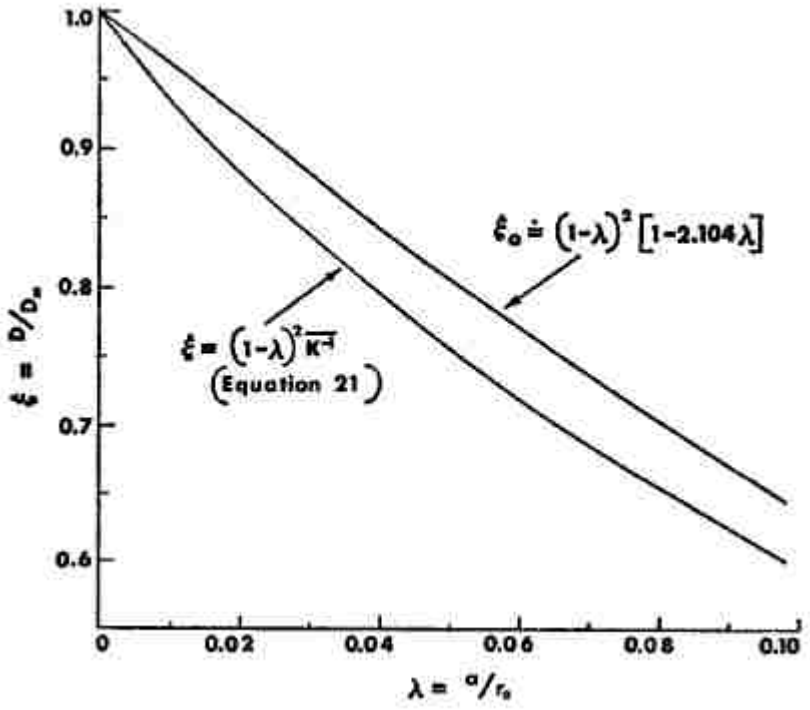

Figure 1-7. Anderson *et al.*'s comparison of the hindered diffusion as predicted from the centerline friction (ξ_o) and from the radially-averaged friction (ξ) for small particles.

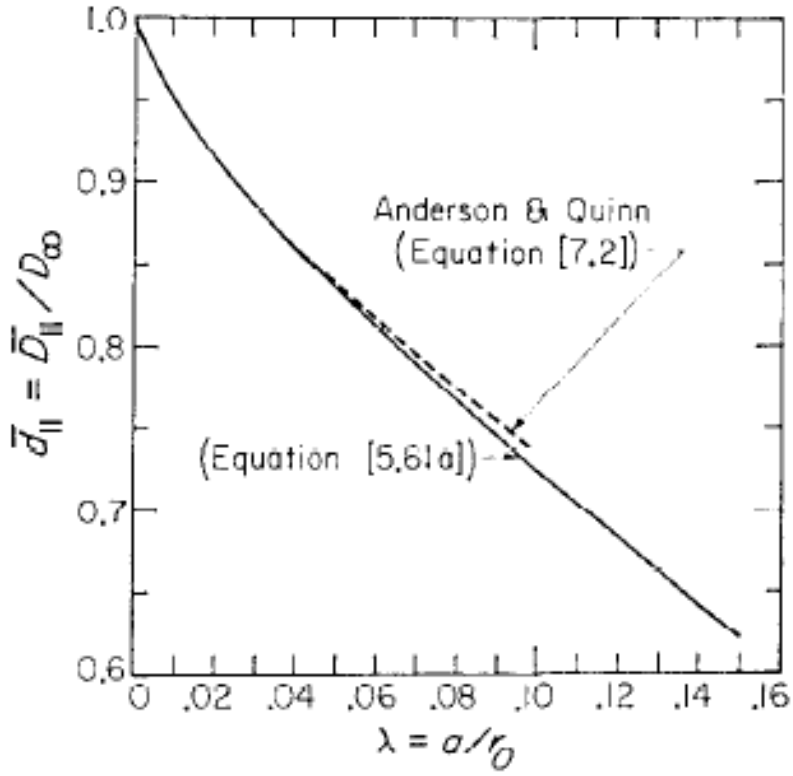

Figure 1-8. Dimensionless mean axial molecular diffusion coefficient vs sphere/cylindrical pore radius ratio. Shown is Brenner *et al.*'s extended analysis in context with a similarly derived equation from Anderson *et al.*'s paper.

Currently, many of the experimental nanofluidic systems have been concerned with providing adequate methods to observe the diffusional hindrance of particles and molecules within these confined systems. As a result, several experimental methods have emerged to track particle or molecular diffusion in nanofluidic systems: e.g., NMR spectroscopy [57-60], a variety of fluorescence microscopy techniques [61-64], UV-Vis absorbance spectroscopy [41], and more recently laser spectroscopy for single particle and molecule tracking [15, 24]. Investigations based on these techniques have revealed that diffusion coefficients in nanofluidic systems are substantially lower than those

observed in bulk solutions. Reasons for the observed hindered diffusion often include hydrodynamic factors [21, 61, 65-67], electrostatic interactions [15, 20, 68], surface morphology, and hydrophobicity of the system [69]. Many of these same studies have concluded that particle-wall or molecule-wall interactions are the likely cause for the observed diffusion coefficients that are substantially lower than those classically predicted: e.g., reversible adsorption or inelastic collisions.

One of the first papers to consider the inelastic effects of a molecule coming into contact with a nanochannel's wall, thereby hindering the molecule's diffusion, was published by Pappaert *et al.* (2005) [21]. It was observed for fluorescently tagged single strand DNA (ssDNA) and smaller tracer molecules (FITC) that when a channel's critical dimension was below a micrometer that the molecular diffusivity significantly decreased by as much as 30 to 40%, as shown in Figure 1-9. In an attempted to account for this significantly hindered diffusion, a simple calculation of the mean time (t_{col}) between two successive analyte-wall collisions can be equated by,

$$t_{col} = \frac{d^2}{12 D_{mol}}, \qquad \text{(Eq. 1-1)}$$

where d and D_{mol} represent the free diffusion space available, and the molecular diffusion coefficient in free space, respectively. From their analysis using Eq. 1-1, they reasoned that the smaller FITC molecules had 6 times more wall collisions then the ssDNA. If the molecule-wall collisions are based only on inelastic interactions, the FITC should experience a larger hindered diffusion when compared to the ssDNA, but this is not the case they experimentally observed. Experimentally, their results suggest that the significantly increased diffusional hindrance experienced by the ssDNA must be accounted for by a much longer adsorption time, rather then simple inelastic molecule-

wall collisions. Although the authors provided the diffusion coefficients for several lengths of ssDNA and FITC dye molecules at a critical dimension of 260 nm, no characterization of the molecule-wall adsorption event was provided.

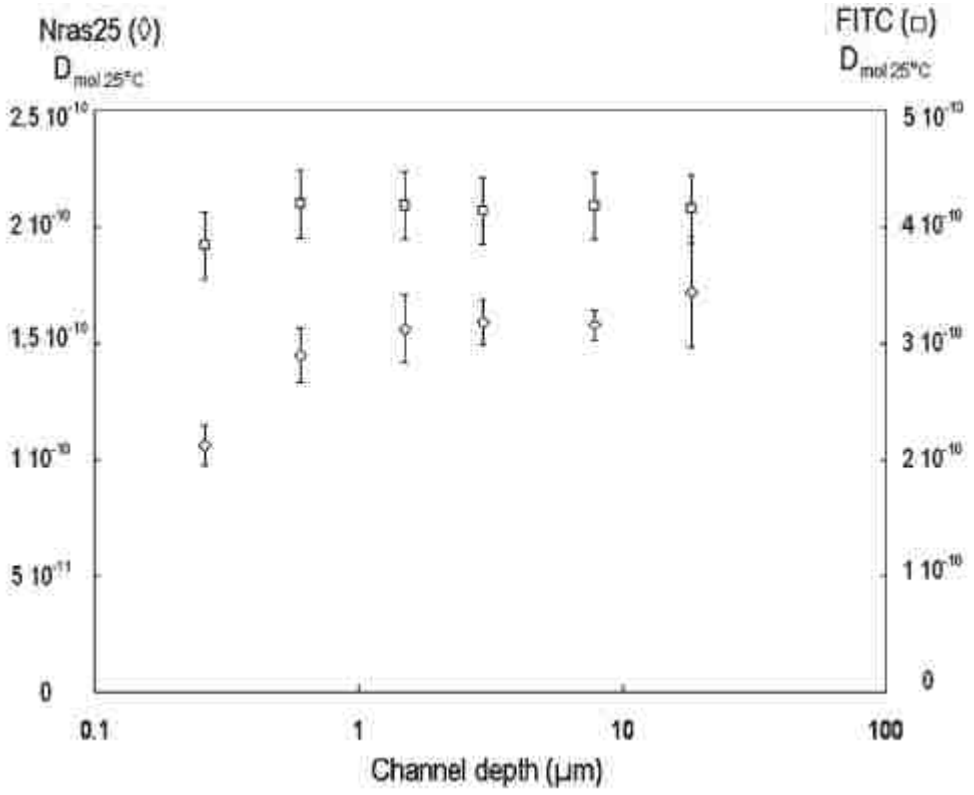

Figure 1-9. Measurements of D_{mol} (cm^2 s^{-1}) as a function of channel depth [21]. The observed diffusion coefficient at a channel depth of 260 nm decreases by ~5% for the small FITC (□) dye molecule, where as the larger ssDNA Nras25 (◊) decreases by 32%.

In a more compelling article by Karnik *et al.* in the following year (2006), a streptavidin-biotin system was devised to characterize the diffusion-limited patterning (DLP) of a nanofluidic channel [70]. The authors demonstrated the ability to pattern alternating bands of fluorescently labeled and unlabeled streptavidin in biotin-functionalized nanofluidic channels with a spatial resolution better then 1 μm. Figure 1-

10 shows the DLP processing steps and resulting fluorescent image. The streptavidin-biotin binding system is considered to be an irreversible adsorption system [70]. By assuming that the time scale of diffusion within the nanochannels is small, the concentration (c) gradient of streptavidin can be assumed to vary in a linear fashion. The resulting flux (J) of streptavidin would be given by

$$J = \frac{AD_{mol}c}{x}, \tag{1-2}$$

where A is the channel's cross-section area, D_{mol} is the molecular diffusivity, and x is the distance of the reaction front from the channel entrance. By further considering the rate of consumption of streptavidin by irreversible binding in a quasi-steady state as equal to the flux of streptavidin,

$$J = \frac{AD_{mol}c}{x} = P\gamma_o \frac{dx}{dt}\ , \tag{1-3}$$

where P is the perimeter of the cross-section and γ_o is the surface binding density of streptavidin. Their resulting solution of Eq. 1-3 can be solved for the D_{DLP} such that,

$$x^2 = \left(\frac{2D_{mol}Ac}{P\gamma_o}\right)t = D_{DLP}t\,, \qquad \text{and finally}$$

$$D_{DLP} \equiv \frac{2D_{mol}Ac}{P\gamma_o}. \tag{1-4}$$

Here the author's have defined the experiment's effective diffusivity, D_{DLP}, as a function of the concentration and channel dimensions, and as long as the concentration has a linear gradient ($D_{DLP} << D_{mol}$). The author's are quick to point out that Eq. 1-4 doesn't appear to accurately quantify their observed results; rather the equation is considered to be a qualitative approximation. The authors further relate a system's geometry and reaction kinetics by the Thiele length (spatial resolution of patterning) which takes the form of,

$$2\ x\ Thiele\ length = \sqrt{\frac{2hD_{mol}}{k\gamma_o}}\ , \tag{1-5}$$

where h is the channel's height and k is the association rate constant. Although the authors have provided some qualitative insights into adsorption within a nanofluidic channel, the lack of accuracy in quantitative analysis leaves much to be desired in understanding the fundamental governing forces and descriptive equations that apply to the adsorption phenomenon in nanofluidic channels.

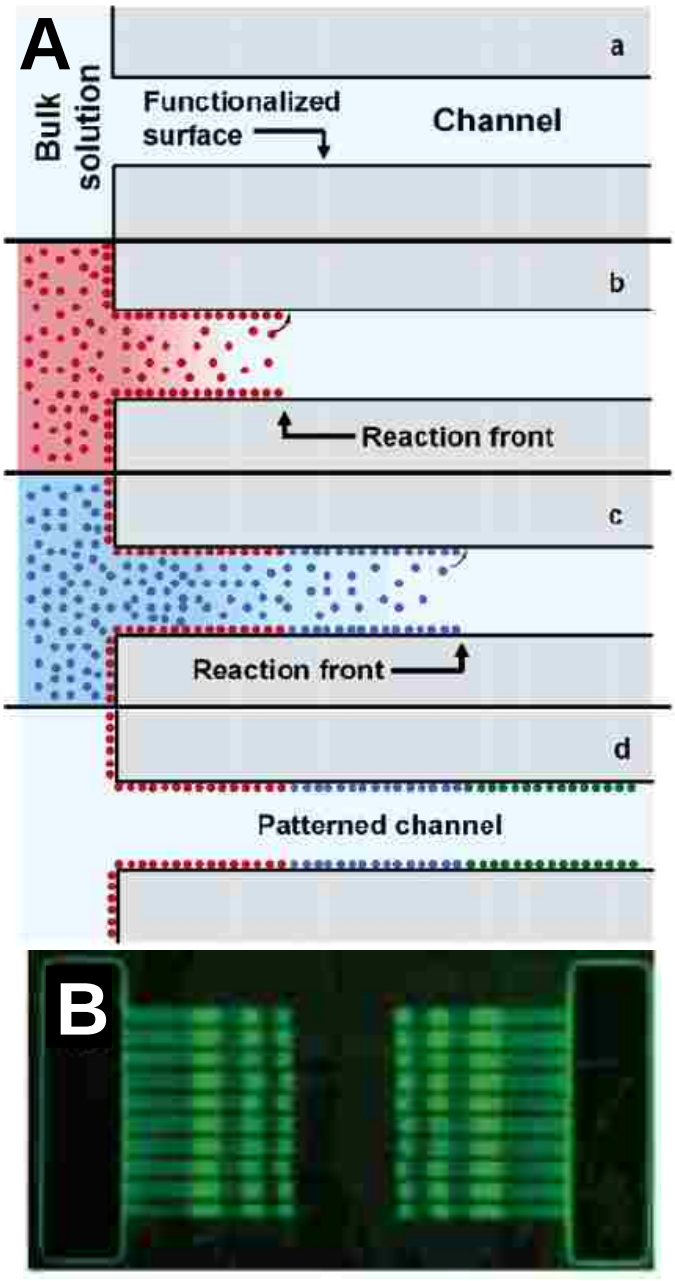

Figure 1-10. (A) The general DLP processing steps. (B) A fluorescent image of the resulting DLP processed nanochannels after alternating Alexa Fluor 488 labeled streptavidin and unlabeled streptavidin solutions.

Measuring the diffusion coefficient by an alternative system, Durand *et al.* monitored the lateral diffusion of fluorescently labeled proteins and dyes as they diffused from one microchannel to another parallel microchannel by a 50 nm tall and 10 μm wide gap [71], see Figure 1-11. In particular, the two molecules studied were fluorescently labeled wheat germ agglutinin proteins (WGA) and FITC dye molecules.

Despite the strong speculation in published articles on the topic of particle/molecule-wall interactions, there remain few reports of systems that allow quantification of the particle's adsorption or particle-wall collisions. Furthermore, experimental observations of unaccounted for hindered diffusion still remains unresolved [21, 70], and the need for experimental techniques and systems to adequately quantify this phenomenon have yet to be reported.

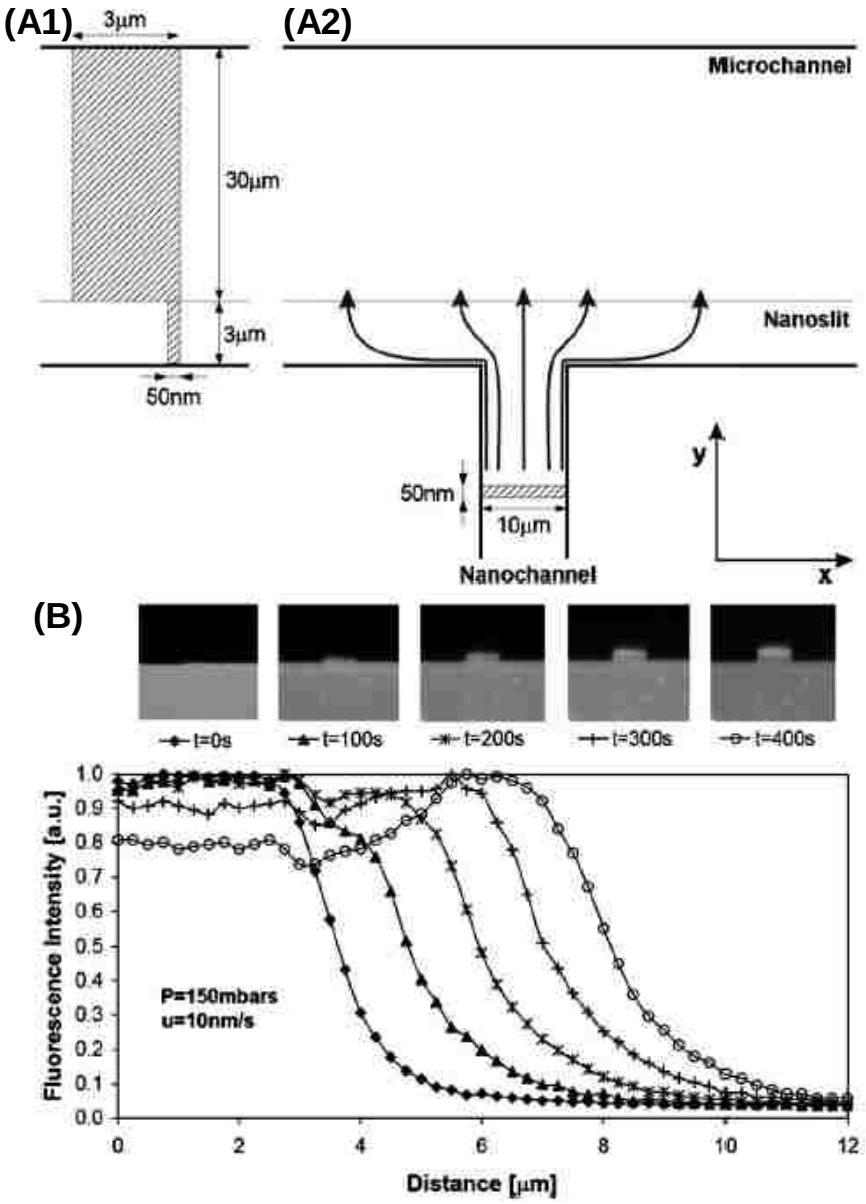

Figure 1-11. (A1) Diagram showing the side view of the nanofluidic device. (A2) Diagram showing a top-down view of the nanofluidic device. (B) A time line of the experimental images showing the fluorescent molecules movement. Below the images, is a plot of the fluorescent wave front as it propagates through the nanochannel region.

1.4 Hypothesis and Relevance of Our Investigation

In this study, we evaluate the diffusive properties of CdSe NCs with an aspect ratio (AR) ranging from 1 to 6; this ratio does not include the monolayer of organic passivation surrounding the NCs. These NCs are suspended in a neat solution of toluene and are allowed to diffuse into an array of nanochannels whose dimensions are 100 nm wide, 400 nm deep, and 1.5 cm long. These nanochannels are etched into a Si substrate and the channel walls consist of thermally grown SiO_2. In order to gain valuable insight into AR-dependent adsorption and diffusion of NCs into and within these confines, we use an aprotic solvent that requires no further modification of the NC's surface for dissolution and allows the system to have negligible electrostatic interactions. Because we seal our nanochannels with a Pyrex cover slip, and CdSe NCs are fluorescent, we are able to track the NC's concentration profile directly by laser scanning confocal fluorescence microscopy (LS-CFM).

Our initial hypothesis was that the NCs would diffuse into the channels at different concentrations because of the significant physical variation of the NCs. Specifically, we expected the diffused concentration within the nanochannels to be a fractional amount of the reservoir's initial concentration due to entrance partitioning, the physical blocking of NCs at the channel's entrance that should vary as a function of AR. We also believed the diffusion profile would follow similarly to the complementary error function solution for an infinite reservoir diffusing into a medium with initially no NCs and a fixed concentration at the boundary. These expected results were predicated on the belief that the combination of the NC's surfactant layer and the solution being aprotic in nature, would allow the NCs to simply interact in a stochastic manner within the

nanochannels. This hypothesis was quickly disproven upon analysis of the experimental results for the NC's profile and concentration within the nanochannels. The experiments in fact reveal a more complicated system where the dynamics of the system are governed by the van der Waals force, leading to unexpected AR trends in the adsorption and diffusion of NCs within the nanochannels.

Our experiments follow the progress of the forward diffusion of NCs into the nanochannels, as well as the reverse migration of the NC's out of the nanochannels back into a reservoir filled with toluene. Observing the NC's concentration as a function of time in both cases, we are able to quantify the particle's equilibrium coefficients, adsorption/desorption rate coefficients, and the effective diffusion coefficient. To date, there has been no published experimental data that quantifies the NC's adsorption/desorption and wall interactions as a function of AR within nanochannels. We provide a method to ascertain the NC concentration as a function of time and distance within the nanochannels. From the data obtained in our experiments, we can further quantify the equilibrium coefficient for the aprotic system of diffused NCs. We will also present a two-site transport model of the system that accounts for NC-wall interactions in the form of reversible adsorption with first order kinetics. The model is used to fit the experimental concentration profiles as a function of time and position. The fitting parameters of the model include the diffusion coefficient, adsorption and desorption rate constants, and two equilibrium coefficients.

The relevance of our analysis of NCs in an aprotic nanofluidic system is experimentally unique. However, the experimental techniques and analysis methods within this work are far more universal. It is expected that these same techniques can be

applied to aqueous nanofluidic systems to quantify the particle and molecule wall interactions that are clearly lacking in much of the current literature. As will be discussed, the transport model proposed in this work, in many respects, provides a much improved accounting of experimental diffusion and adsorption observed within the nanofluidic system.

CHAPTER 2 CHARACTERIZATION TECHNIQUES

2.1 Introduction

In this chapter we will discuss briefly the instruments implemented in characterization of the nanocrystals (NCs) and nanochannels used in this report. For NCs, it is important to accurately access their size, shape, fluorescence, and general chemical makeup. The NC's physical properties are especially vital to the experimental task of understanding their transport properties. For the nanochannels, the fabrication process and final physical dimensions are probed by scanning electron microscopy. The diffusion experiments hinge on the laser scanning confocal microscope providing the necessary fluorescence based images that allow for the tracking and quantification of the NCs.

2.2 Powder X-ray Diffraction

Powder x-ray diffraction (PXRD) is a valuable tool to gauge a powder sample's average crystallinity, composition, and particle size. It is important to realize that PXRD averages the bulk powder's properties and is not meant to give spatially resolved information. When the x-ray beam's wavelength interacts and penetrates into a crystalline material's lattice with a specific atomic spacing, the crystal will diffract the beam, shown in Figure 2-1. The governing relationship of this interaction is called Bragg's Law, and is as follows

$$n\lambda = 2d \sin\theta \tag{2-1}$$

where n, λ, d, and θ are the integer multiplier (usually 1), wavelength of the incident beam, the atomic spacing between lattice planes, and the Bragg angle, respectively.

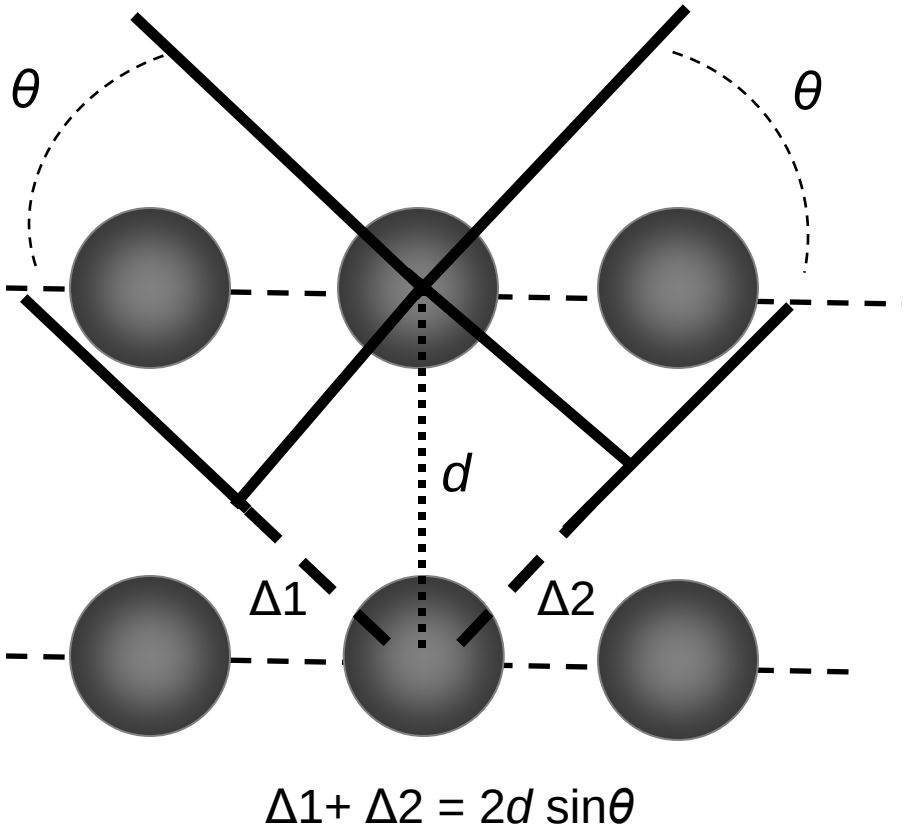

Figure 2-1. A schematic of the x-ray beam's penetration and diffraction.

Since XRD probes the atomic structure of a material, one can also gain information about the composition and phase of the material. Since each phase and composition of a material yields a unique signature, large databases have been constructed to aid in the identification of unknown materials. When looking at randomly distributed crystalline particles, PXRD will produce an average of all the allowable diffraction patterns from each crystallographic plane. This is much different than single crystal XRD which may only give the diffraction from one facet or plane of the crystal. In the context of CdSe NCs, the PXRD spectra will give us data on multiple planes of the crystals, i.e. we should see characteristic peaks that represent the hexagonal planes of CdSe.

In the case of NCs, the average size can also be estimated by the peak broadening of the diffracted beam, which is a result of a sample's particle size (s) decreasing. The general correlation is summarized by the Scherrer equation,

$$s = \frac{0.9\lambda_s}{B\cos\theta_B} \tag{2-2}$$

where λ_s, B, θ_B, is the source's wavelength, the full-width half max of the peak fit, and the corresponding peak angle, respectively. Unfortunately, this method of calculation has a high error when applied to small NCs (<20 nm). This error stems from the angle resolution, and furthermore the use of this equation is for spherical particles and can not be applied to anisotropic particles. Therefore, this technique is mainly limited to monitor the elongation of the (0001) plane or c-axis, and confirm that the NCs are in the wurtzite phase.

2.3 Fourier Transformed Infrared Spectroscopy

Fourier transformed infrared spectroscopy (FTIR) was introduced by Michelson in 1891. The instrument is widely used today and is often referred to as the Michelson interferometer. As the name states, the instrument probes the infrared region (~.76 μm for near IR and ~1000 μm for far IR) and most desktop models are specifically useful for probing the bonds of molecules (2.5 to 15 μm or equivalent to a wavenumber range of 4000 to 660 cm^{-1}) that can be in the form of a gas, liquid or solid form. The basic working principle of the FTIR is the measurement of the path difference that causes interference between the two beams originating from a single source, typically a polychromatic infrared source. The source's beam is initially collimated and directed to a beam splitter. The beam splitter is usually made out of a thin film polymer, as glass is

not transparent in the IR region, and in practice only covers a specific region of IR; so, several types of beam splitters will be needed to cover the whole IR range. After the beam is split, one beam is reflected to a fixed mirror that simply reflects the beam back to the splitter, while the other beam is transmitted through the beam splitter and onto a moving mirror, which reflects the beam back to the splitter. The beams are recombined at the splitter, where the difference in path length creates constructive and destructive interference or an intensity variation as a function of path difference. The beam is then further sent through the sample to the detector behind it. The setup of this system is shown in Figure 2-2.

The collected data (light adsorption/transmission as a function of mirror position) then needs to be processed by a Fourier transform to produce the desired result of intensity as a function of wavelength. The collected data is represented by

$$I'(\delta) = \frac{I(\bar{\nu})}{2}(1+\cos 2\pi\bar{\nu}\delta) \tag{2-3}$$

where $I(\bar{\nu})$ is the source's intensity at frequency ($\bar{\nu}$) at any point where $\delta = n\lambda$; n is an integer. The interferogram, $I(\delta)$, of the modulated component is defined as

$$\begin{aligned} I(\delta) &= \frac{I(\bar{\nu})}{2}\cos 2\pi\bar{\nu}\delta \\ &= B(\bar{\nu})\cos 2\pi\bar{\nu}\delta \qquad , \textit{while } B(\bar{\nu}) = \frac{I(\bar{\nu})}{2} \end{aligned} \quad . \tag{2-4}$$

The interferogram is represented as the cosine Fourier transform of $B(\bar{\nu})$. The spectrum is therefore calculated by taking the cosine Fourier transform of the interferogram.

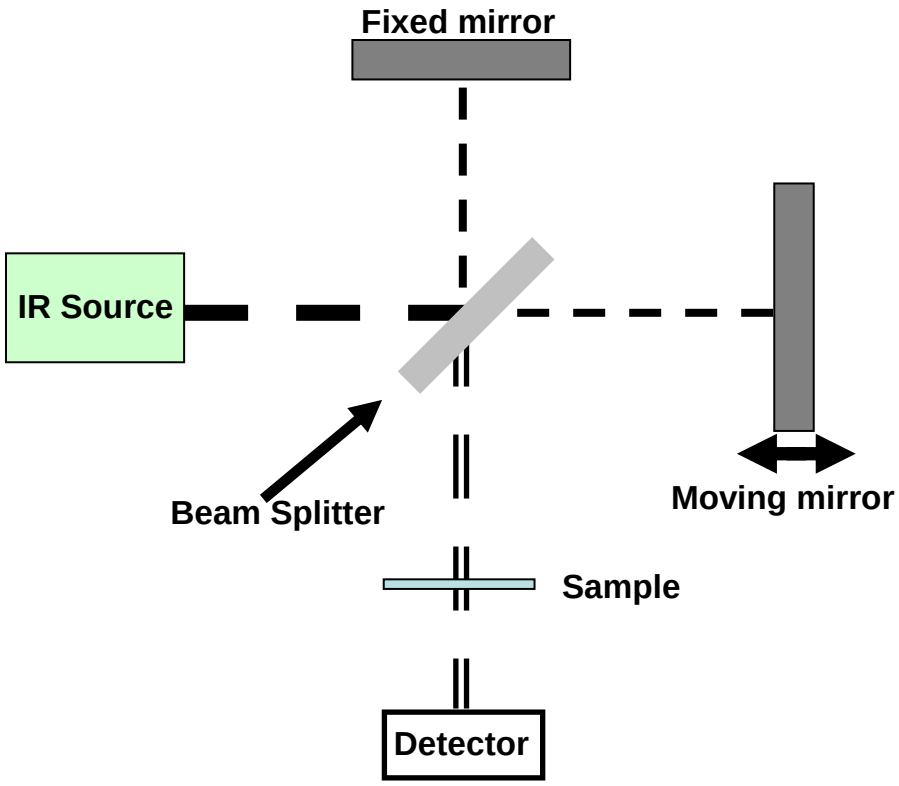

Figure 2-2. A diagram of the component's layout for a FTIR instrument.

2.4 Transmission Electron Microscopy

Transmission electron microscopy (TEM) is an important tool in imaging the structural properties of crystalline materials, especially when the material's size is on the order of nanometers. The TEM's atomic-resolution allows for the precise measurement of the crystalline material's dimensions and in the case of particles, further provides the details of the shape. The TEM system images thin materials by passing an electron beam through the material and onto a recording device. Today's TEM systems often utilize additional spectroscopic tools that allow for chemical, surface, and stress-strain mapping. Note that above the specimen is where the electron source and condenser lens is provided and these are not shown.

The TEM system, shown in Figure 2-3, requires an electron source, condenser lens, specimen stage, objective lens, magnification system, and data recording systems. Typically, the use of a tungsten filament is used to produce the required electrons to probe the specimen. An operating beam at 200 keV allows for a nearly temporally and spatially coherent electron image to be produced. There are two basic modes of operation: diffraction mode, also commonly referred to as dark field imaging, allows the crystallographic diffraction pattern to be imagined see, while the bright field mode allows the viewing of the direct electrons (the direct image).

In figure 2-3(a), the diffraction mode is shown to preclude the bright field aperture, which removes the center beam(s) from the back focal plane, and instead includes the use of an intermediate aperture to allow for selective-area diffraction (SAD). Naturally the diffraction pattern will need to be further focused on the imaging screen, done by adjusting the intermediate lens, and the central beams will need to be blocked so that the imaging system isn't overloaded. It should be noted that the beam is often times condensed to a specific area on the specimen to give a high resolution diffraction pattern. In this way, composite samples can have SAD performed on them with high spatial resolution, an inherent advantage over bulk crystallographic methods such as PXRD. The spatial resolution of an electron is less than 1 Angstrom, but a TEM's resolution is limited by a number of lens aberrations, and therefore the instrument's resolution is usually limited to ~1.5 nm. Newer instruments with aberration corrections can, and have, achieved sub-nanometer resolutions.

Bright Field imaging, shown in Figure 2-3(b), allows the user to directly image the particle's size and shape with atomic precision by using an aperture to block the outer

electrons; the outer electrons are from diffraction and make up the dark field image. The intermediate lens is again used to focus the center beam on the imaging system. The magnification is also controlled by changing the intermediate lens strength. Bright field images of the various aspect ratio NCs will be shown in Chapter 3.

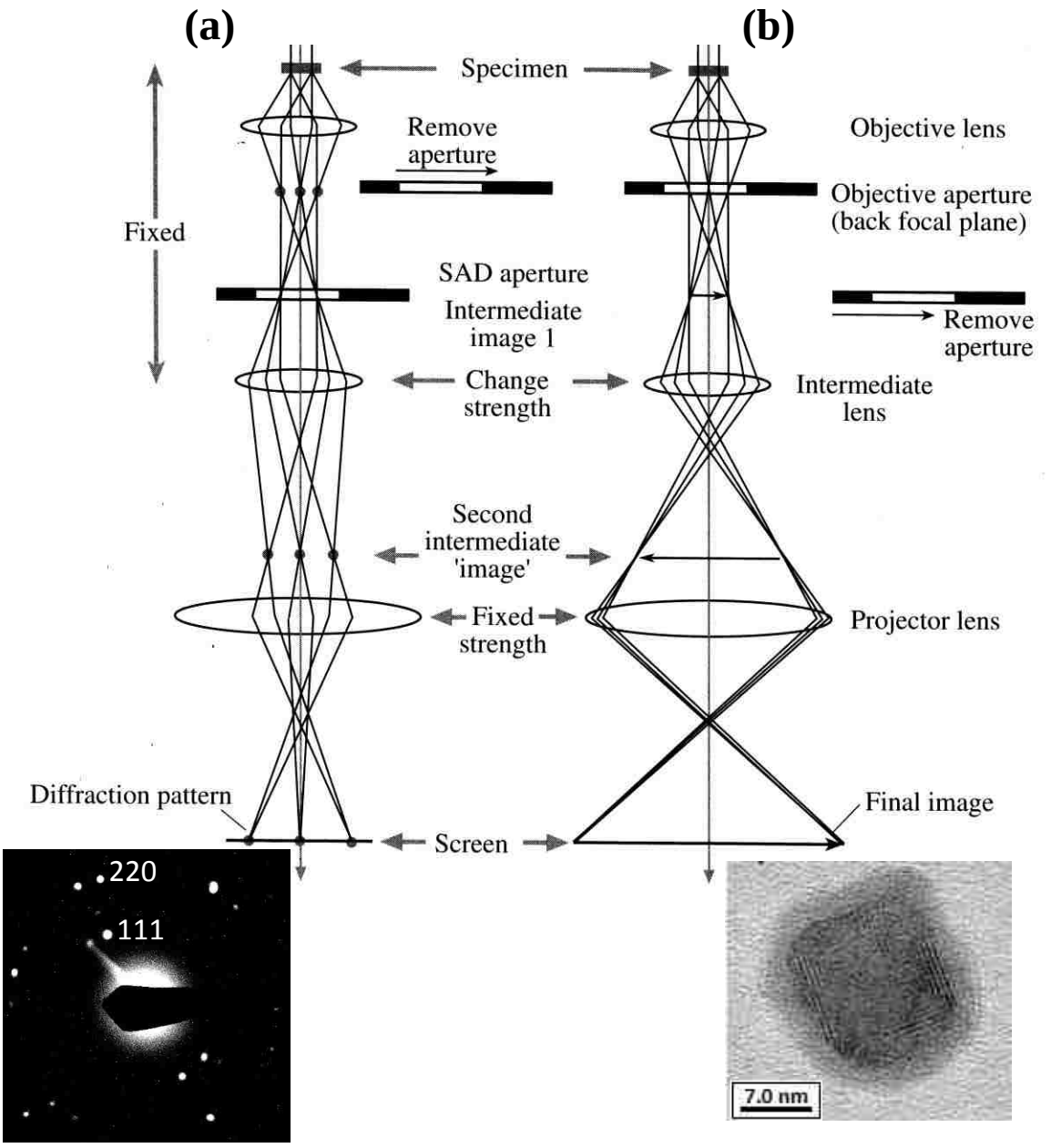

Figure 2-3. (a) The TEM's dark field imaging schematic that is used to capture the diffraction pattern by the imaging system [72]. Below (a). A dark field image is captured that shows the SAD pattern of a crystalline Ge nano-cube. (b) The TEM's bright field imaging schematic that is used to capture the direct image by the imaging system. The high resolution bright field image shows a Ge nano-cube surrounded by a thick amorphous surfactant.

2.5 Electron Dispersive Spectroscopy

The TEM that was used in the characterizing the NCs was also equipped with an electron dispersive spectroscopy system (EDS or EDX). When the electron beam, provided by the TEM, is scanning the specimen, x-rays are generated within the specimen due to the inelastic scattering of the probe electrons. The sample's x-rays are then collected by a detector, located above the sample plane, which converts the x-rays into an electronic signal, similar to PXRD. Depending on the sample's properties, the amount of x-rays collected will directly determine the quality of the data, specifically the noise-to-signal ratio. If a low amount of x-rays are counted then the inherent accuracy and chemical detection can be questionable. In order to achieve a desired accuracy, and adequate detection of the chemical species and quantities, the TEM magnification was lowered to gain a larger sampling of the CdSe NCs, discussed in Chapter 3. The collection of data was typically run for a minimum of 5000 carbon counts (~ 5 minutes of collection time) and provided sufficient intensity for the Cd and Se energy peaks to be resolved. The quantification of the Cd and Se atomic percentage in the samples was provided by the software's integration of the relevant peaks.

2.6 Scanning Electron Microscopy

Scanning electron microscopy (SEM) is used frequently in the fabrication of the nanofluidic channels. Mainly in this report, SEM is used to measure the physical dimensions of the channels, however just like TEM, a variety of additional instruments can be mounted on the sampling chamber, for example EDS. The SEM uses an electron

beam to raster over the sample and collects the scattered electrons to form an image of the surface. The SEM collects both the elastically scattered electrons, usually referred to as the backscattered electrons, and the inelastically scattered electrons, called the secondary electrons, to form an image of the surface. Since the electrons only need to interact with the surface, and not penetrate through the sample, the electron beam used to probe hard surfaces is usually 30 keV. Softer materials like polymers or biological samples usually require the beam to be reduced to 5-15 keV. Often times the samples are best prepared by putting a thin layer of Au or Pt (1-5 nm) on the surface to be imaged. By doing so, the absorption or charging of the sample is drastically reduced and a higher resolution image can be formed.

2.7 Laser Scanning Confocal Fluorescence Microscopy

The typical laser scanning confocal microscope (LS-CFM) platform can be a very versatile microscope setup, see Figure 2-4. Simple setups will usually have only one or two sources for the probing of specimens, typically a broad UV source like a Mercury lamp and a conventional incandescent light source. However, modern commercial setups can equip 2-3 lasers that offer unique excitation wavelengths (458, 543, 633 nm) that are connected to the optics by fiber-optic cabling. Naturally, the detection system to image the incoming fluorescence also has to be sensitive and well matched to the sources mentioned. Most of the higher cost systems make use of two or more detectors that are optimally matched to the spectral ranges of operation. Most LS-CFMs are equipped with a variety of objectives that can be used under dry conditions or special objectives for

oil/water immersion. These objectives further come in a variety of magnifications up to ×150 and may also be polarized.

The general operating principle of a LS-CFM is that a slit (or pinhole) is placed in between the source and a dichroic mirror, see Figure 2-5. The source's incoming light is split by the dichroic mirror, where part of the light is projected onto the sample, while the other portion is reflected towards the detector. The portion of light aimed at the sample passes through an objective to the focal plane, and is either scattered or adsorbed. The reflected light, composed of the original source's and the sample's fluorescent emission(s), are then collected by the same objective and passed through a second slit (pinhole) that is placed symmetrically with the first and resides in front of the detector. The second slit is in a conjugate plane with the first slit, and therefore only allows the focused light from the sample region to reach the detector. The collected light is used to produce a scanned line image of the specimen, where the scan line is usually held in position for several micro-seconds to allow for an averaging of the line's photo-luminescence. Note that the scanning wavelength (laser's wavelength) should always be blocked or spectral region removed, since the sample will partially reflect the beam back into the detector, thus usually overloading the detector at the source's wavelength.

Usually the software allows the user to select the image quality (pixels to define image), the number of scans to be averaged (usually 1 to 16 passes), the spectral range of interest (this can be further subdivided into multiple scans of specific spectral ranges of fluorescent tags and later recombined for a composite image), or further allows for successive pictures to be taken as a function of time (movie mode). A particularly great feature of the microscope is that the spectral range is segregated, by a spectral chopper,

into wavelengths as small as 10 nm ($\Delta\lambda$). This allows a user to view an image by a particular 10 nm wavelength slice and compare it directly to a different wavelength while maintaining all the reference points. Another distinguishing feature often found on these microscopes, is the ability to make incremental height adjustments as small as 0.1 μm. This allows the microscope to take multiple images of a sample as a function of height, and can produce 3D images that display discreet multi-photonic emissions that correlate to the various fluorescent tags employed. So, surprisingly complex imaging can be achieved with the ease of automation on these platforms.

In this report, we use the LS-CFM with an Argon laser to excite the NCs in the nanochannels. There fluorescence can be calibrated and tracked as the NCs diffuse into the nanochannels. The calibration methods and tracking results will be discussed in later chapters.

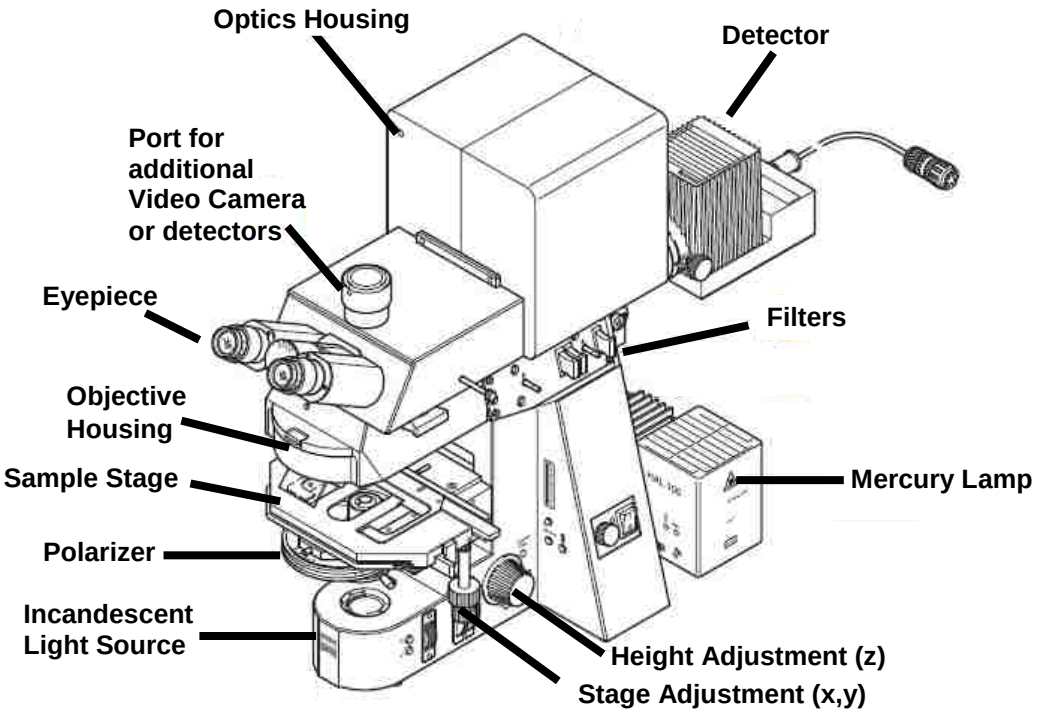

Figure 2-4. A diagram of a typical confocal fluorescence microscope [73]. The Objectives are removed in this diagram, but are usually attached to the underside of the Objective housing unit. Lasers are typically coupled to the backside of the Optics Housing by fiber optic cabling.

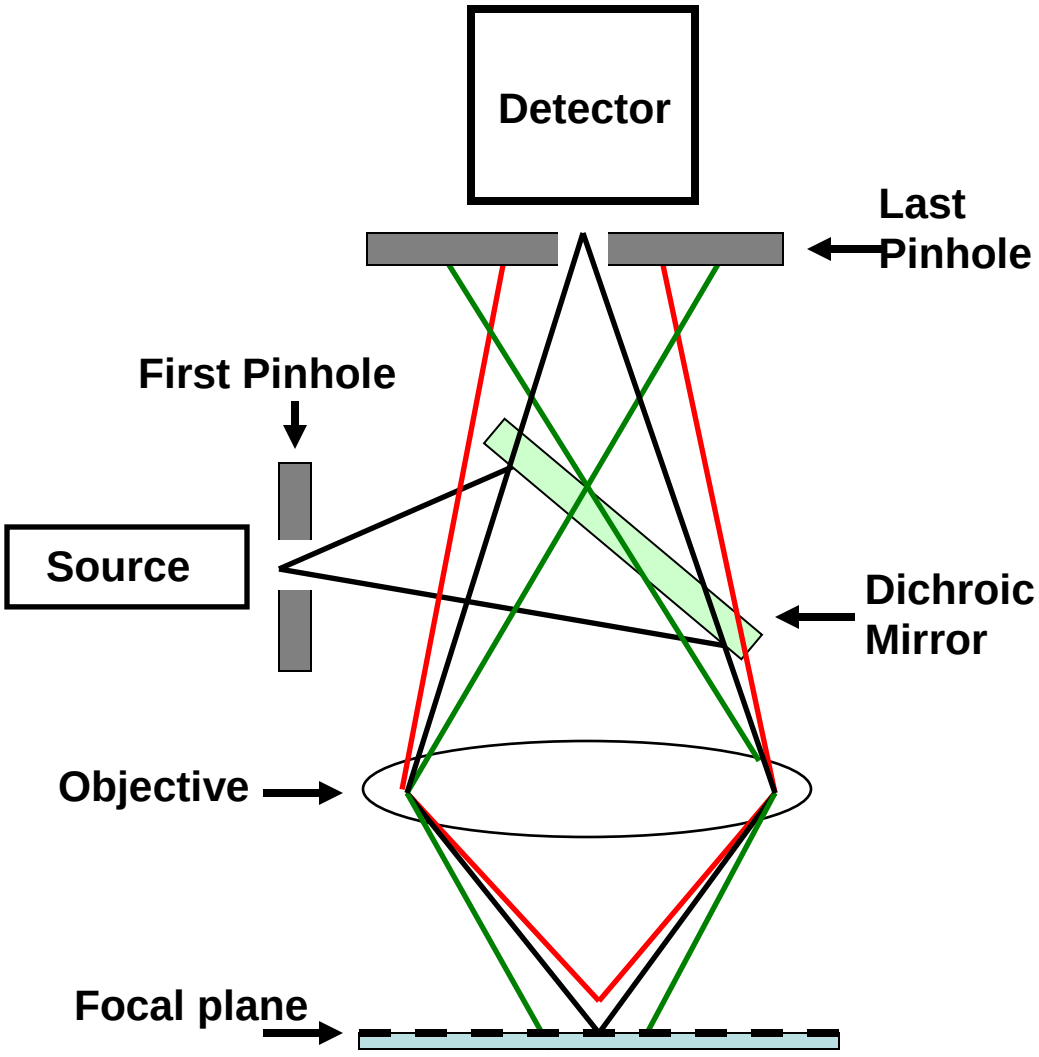

Figure 2-5. A diagram of the basic operating principle of a confocal fluorescence microscope. Only photons from the focal plane will be imaged by the detector.

CHAPTER 3 SYNTHESIS AND CHARACTERIZATION OF NANOCRYSTALS

3.1 Introduction to the Synthesis of Semiconductor Nanocrystals

Ever since the first reports on liquid-based synthesis of tunable photoluminescent semiconductor nanocrystals (NCs) [74, 75], there has been a considerable effort to produce high yield nano-bearing pathways for every semiconductor system. The range of applications includes optoelectronics [76, 77], photovoltaics [78-81], and biological imaging [82-84]. Much of the interest in these nano-sized materials, as compared to bulk materials, is inherent to the unique quantum confinement effects observed at this scale [85-88]. Because the number of atoms that make-up a NC is so few, only a couple of thousand, discrete energy states can be exhibited. Although the NCs typically retain their bulk crystal structure, the band structure is dependent on the NC size and thus allows the NC's size to tune the optical properties.

The synthesis of shaped NCs, i.e. pyramids, rods, dumbbells, tetrapods, and jacks can lead to potentially novel electrical and optical properties both at the micro- and macro-scale[89]. For example, CdSe rods have an optical polarization and dipole moment associated with their elongation of the c-axis that is inherent to the wurtzite crystal structure. In order for these properties to be exploited at the macro-scale, ordering of these anisotropic NCs by self-assembly techniques has been favorably examined [90] and without a high degree of rod ordering birefringence effects cannot be observed. In order to examine many of the physical attributes of shaped NCs, several important liquid-based synthetic pathways have been developed. The preferred solution-based methods typically include a mixture of weakly and strongly interacting surfactants that alter the growth rates of particular crystal facets. Temperature and concentration of the species

can be further controlled to yield variations in the shape and growth kinetics. Typically, parametric studies are often needed to gather sufficient information to predict the growth mechanisms involved in the formation of the final resulting particles. In the case of the CdSe material system, several morphologies have been described previously from parametric variations [18, 85]. Described within this section are the details as to how each AR NC was synthesized and the general results from several useful characterization techniques.

3.2 Synthesis of Various Aspect Ratio Nanocrystals

The hot solution precipitation method used in producing the various AR NCs is an adaptation of Manna, *et al.* synthesis scheme for CdSe rods [18]. The cadmium precursor used in their procedure is dimethylcadmium ($Cd(CH_3)_2$; 97%) and requires a glove box or inert atmosphere for storage and preparation. Selenium powder (99.999%) is used as a precursor because the available Se organic-based precursors have a lower metal and organic purity. The author's chose tri-n-butylphosphine ($C_{12}H_{27}P$ or TBP, 99%) for solvating the Se and Cd precursors for stock solutions. The bulk solution heated for the decomposition of the precursors consisted of tri-n-octylphosphine oxide ($C_{24}H_{13}OP$ or TOPO, 99%) and provides a liquid medium that can withstand the author's prescribed reaction temperatures (up to 360 ^oC). Their procedure further utilizes a hexylphosphonic acid ($C_6H_{15}O_3P$ or HPA, 95%) in a 20 mol% concentration to hinder the growth kinetics of the crystal facets, thereby allowing for anisotropic elongation in the (0001) direction of the NC (c-axis). The reported elongation process of aspect ratios (AR) above three typically requires additional injections of Cd and Se stock solutions to replenish their

respective concentrations for sustained growth. In this manner the authors reported the capability of producing NC rods that were up to 100 nm in length with an AR $\geq$ 30.

Our procedure uses cadmium acetate dihydrate ($Cd(CH_3CO_2)_2 \cdot 2H_2O$ or CdAc, >98%), which when stored under dry conditions is an acceptable alternative for the cadmium precursor and removes the need for glovebox related preparations. The use of n-hexadecylphosphonic acid ($C_{16}H_{35}O_3P$; >97%, HDPA) was available to purchase in a high purity form than the prescribed HPA. Instead of using TBP as a solvent, n-trioctylphosphine ($[CH_3(CH_2)_7]_3P$ or TOP, >90%) was used to produce the Cd and Se stock solutions. Additionally, the employed procedures differ in both the time and temperature of the reactions in order to further control the crystalline size and elongation process.

In general, the synthesis was performed in a 100 mL three-neck round-bottom flask under an argon atmosphere. Figure 3-1 shows the experimental setup where the flask sits on top of a heating mantle with a stir plate underneath, typically set at a stir speed of 600 to 1000 RPM. All stock solutions used in the synthesis of NC rods were stirred and degassed by heating above 120 ^oC under vacuum for ~15 minutes, after which time the solutions were backfilled with argon to ~1 atm and transferred to a suitable storage container. The temperature was measured by a K-type thermocouple and regulated by a variable voltage regulator (Variac).

Once NCs were produced, the removal of excess solvents, surfactants, and reactants was achieved by several washing steps. The NCs were separated into equal amounts into six centrifuge tubes (15 mL). To each tube, a small amount of chloroform (~1 mL) was added and mixed, and then methanol was added in a ~4:1 ratio as compared

to the original chloroform amount. The added methanol should induce precipitation of the NCs that can then be centrifuged at 5000 rpm for 5 minutes to separate the two phases. The resulting solution should be a light yellow or near colorless with a reddish solid on the side of the centrifuge tubes. At this point, the liquid portion is removed and ~2 mL of chloroform is added to disperse the NC solid. Again, methanol is added in a ratio of 4:1 to chloroform. The centrifugation process and continued washing are typically done a minimum of three times. After the NCs are properly washed, a size precipitation method can be invoked. All of the NCs are concentrated in chloroform and combined into one centrifuge tube. The goal in size precipitation is to remove smaller or larger NCs that deviate from the mean size. Larger particles are easier to precipitate then smaller particles because of the amount of surface surfactants. So, in order to remove smaller NCs, the goal is to impose a methanol to chloroform solution ratio that will precipitate a majority of the NCs but leave a small amount of NCs in solution or a "light" colored solution after centrifugation. For larger NC removal, a majority of the NCs will need to be solvated in chloroform with the addition of only a small amount of methanol to precipitate out the larger NCs. For each AR NC, the described methods may vary in the ratio of chloroform to methanol required for this cleaning process mainly due to the differences in the NC's AR and solution concentrations, and therefore will not be reported in detail.

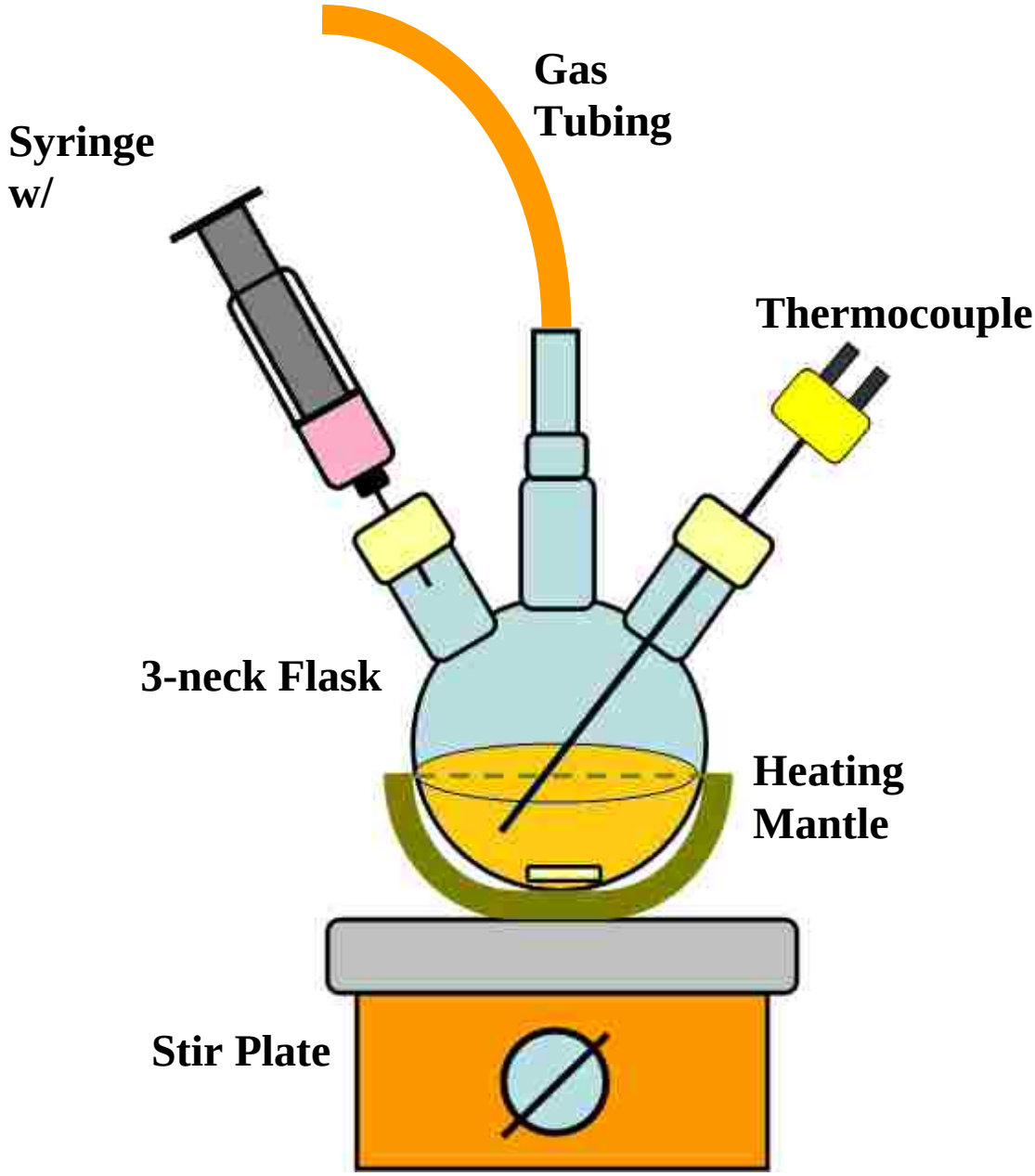

Figure 3-1. A diagram of the experimental synthesis setup with the heating mantle partially removed.

The synthesis steps of CdSe NC dots are:

Step 1. Degas a mixture of 1 mmol CdAc and 10 mmol TOPO in a 3-neck flask and backfill with argon to ~1 atm. Heat the solution to 300 ^{o}C and then stabilize the temperature to 265 ^{o}C.

Step 2. Separately, heat and stir a solution of 0.75 mmol Se and 2 mmol TOP in a vial until fully dissolved. Allow the solution to cool and load into a syringe.

Step 3. Once the temperature of the Cd solution stabilizes at 265 ^{o}C, the Se solution is quickly injected. The reaction's solution will change in color from light yellow to deep red and the typical temperature drop from injection will lower the temperature ~245 ^{o}C.

Step 4. The reaction is allowed to recover to the growth temperature of 265 ^{o}C (~30 sec) for a total time, from nucleation, of 2.50 minutes. After which the heating mantle is removed and the solution is stirred until cooled to room temperature.

Step 5. Washing and size precipitation methods can then commence.

Synthesis for AR 2 and 3 NCs was achieved simply by controlling the time of the reaction with the addition of the HDPA surfactant. The steps for synthesis of CdSe AR 2 and 3 rods are similar for both reactions and only differ in *Step 4*.

Step 1. Degas a mixture of 1 mmol CdAc, 10 mmol TOPO, and 2 mmol of HDPA in a 3-neck flask; afterwards backfilling with argon to ~1 atm. Then heat and stabilize the solution to 300 ^{o}C.

Step 2. Separately, heat and stir a solution of 0.75 mmol Se with 2 mmol TOP in a vial until fully dissolved. Allow the solution to cool and load into a syringe.

Step 3. Once the temperature of the Cd solution stabilizes at 300 ^{o}C, the Se solution is quickly injected. The reaction's solution color will change from light yellow to deep red with a temperature drop to ~280 ^{o}C.

Step 4. A growth temperature of 280 ^{o}C is maintained for 1 minute for AR 2 rods or 2.5 minutes for AR 3 rods. After which the heating mantle is removed and the solution is stirred until cooled to room temperature.

Step 5. Washing and size precipitation can then commence.

The method of synthesis for higher AR rods (> 3) includes the preparation of two stock solutions that will be used to prolong the growth conditions. The two stock solutions used are as follows:

Cadmium stock solution (CdSS) includes 4.40 mmol CdAc with 12 mL of TOP (approx. 32 mmol). The solution was mixed in a 3-neck flask, degassed, and then backfilled with argon to ~1 atm. The solution is then heated until the CdAc is fully dissolved. The solution was allowed to cool and poured into a vial for storage.

Selenium stock solution (SeSS) includes 1.60 mmol Se with 12 mL of TOP. The solution was degassed in a 3-neck flask, backfilled with argon to ~1 atm, and then cooled to room temperature. The solution was transferred to a vial for storage.

To prepare NCs that are greater then AR 3, an additional injection volume of the CdSS and SeSS are needed in *Step 4* in the previously described reactant limited procedures. In general, *Step 1* through *3* are the same and only *Step 4* will be discussed in detail as it relates to AR 3.5, 4, and 6.

Aspect ratio 3.5 (*Step 4*). A growth temperature of 280 ^{o}C is maintained for 2 minutes, at which time the drop-wise addition of 0.50 mL SeSS and 0.50 mL of CdSS, both mixed and added to one syringe, is injected over a period of 1.50 minutes. After the last drops are added, the heating mantle is removed and the solution is stirred until cooled to room temperature.

Aspect ratio 4 (*Step 4*). A growth temperature of 280 ^{o}C is maintained for 2 minutes, at which time the drop-wise addition of 1 mL SeSS and 1 mL of CdSS, both mixed and added to one syringe (2 mL total), is injected over a period of 4 minutes. After the last drops are added, the heating mantle is removed and the solution is stirred until cooled to room temperature.

Aspect ratio 6 (*Step 4*). A growth temperature of 280 ^{o}C is maintained for 2 minutes, at which time the drop-wise addition of 2 mL SeSS and 2 mL of CdSS, both mixed and added to one syringe (4 mL total), is injected over a period of 8 minutes. After the last drops are added, the heating mantle is removed and the solution is stirred until cooled to room temperature.

3.2 Characterization of Nanocrystals

Once NCs are produced, the characterization of their physical and optical properties needs to be clarified before their use in diffusion experiments. One of the best ways to probe the NC's physical dimensions is to use high-resolution transmission electron microscopy (HRTEM). Figures 3-2 through 3-7 show example images for each

of the ARs used in the diffusion experiments. The NCs were prepared for imaging by diluting a drop of the final NC solutions, after size precipitation was completed, with 0.1 cm^3 of neat hexanes. One drop of this diluted solution was then put onto a 200 mesh Cu holly carbon TEM grid and allowed to dry. At high resolution, the crystalline structure allows for the imaging of the lattice fringes. When NCs appear to be in a closely packed arrangement, the thickness of the passivating ligands can be approximated by the average spacing between the NCs, thus allowing the calculation of the NC's total diameter and length. In our description of "aspect ratio" (AR), we only consider the physical crystal dimensions and do not consider the added length of the surfactants in our calculation. Figure 3-8 shows a dense amount of AR 3 NCs that were packed together during solvent evaporation. The inset of Figure 3-8 shows a HRTEM image that measures the rod to rod distance of ~2.4 nm. The calculated thickness of the passivation layer is therefore ~1.2 nm, which is in good agreement for HDPA. Literature values for TOPO are typically at considered to be 5-6 Angstroms in length [91], and HDPA's hydrocarbon chain is twice as long. It is possible that the hydrocarbon chain can intermingle with another NC's and effectively reduce the measured inter-particle distance, but this is unlikely under these circumstances. At lower resolutions more of the NCs can be imaged at once, thus allowing for a statistical analysis of the bulk solution's average NC size. Additionally, the TEM has the ability for quantitative elemental analysis by the technique of energy-dispersive X-ray spectroscopy (EDS). Figure 3-9 shows the typical energy signature of CdSe NCs, note that the carbon energy peak has been removed for clarity. The quantitative analysis reveals a composition for Cd of 65.6 atomic % with 34.4 atomic %

Se. This ratio can give insight into the limiting reactant during the nucleation and continued growth of the NCs.

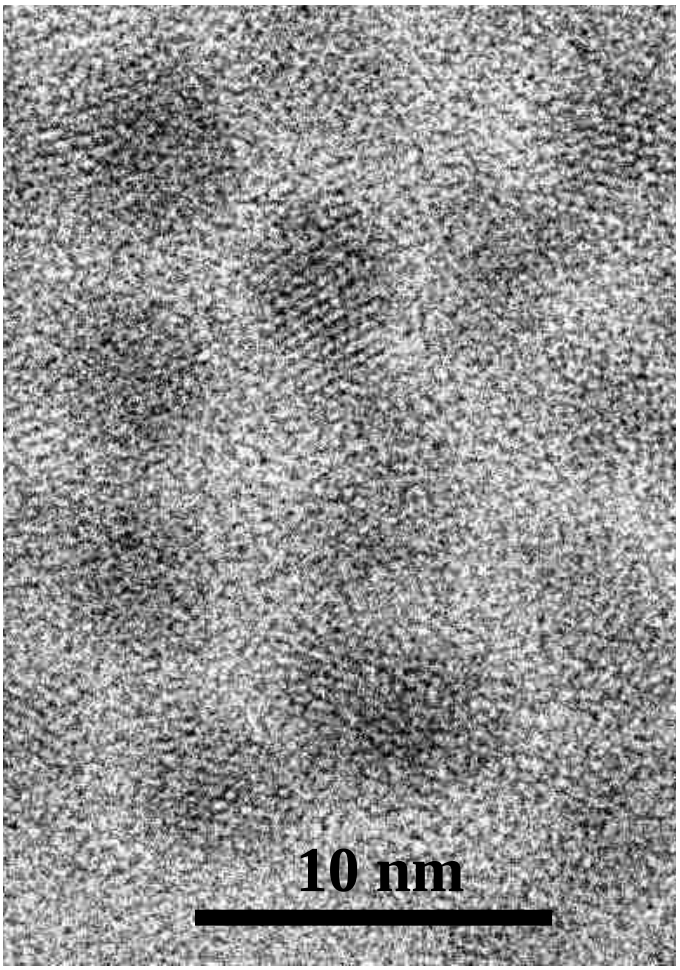

Figure 3-2. A HRTEM image of AR 1 NCs with an average width of 4.0 nm.

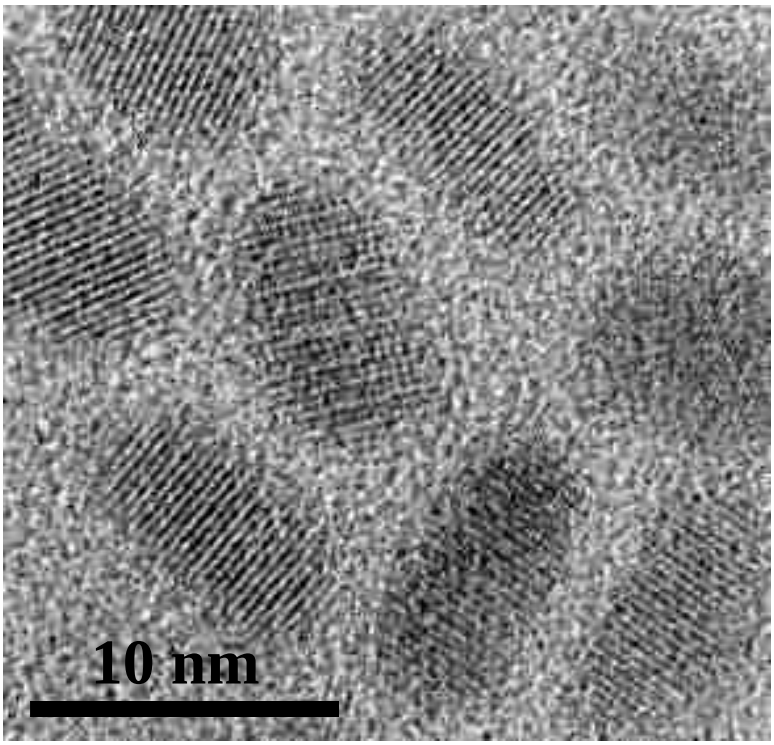

Figure 3-3. A HRTEM image of AR 2 NCs with an average width of 3.7 nm.

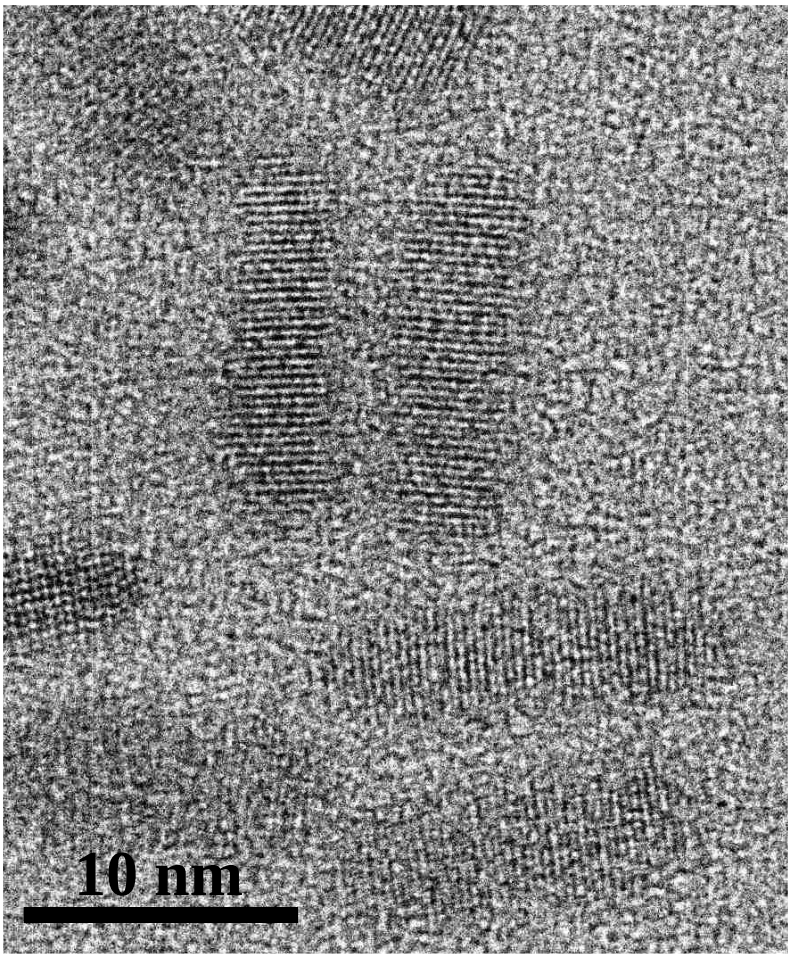

Figure 3-4. A HRTEM image of AR 3 NCs with an average width of 4.5 nm.

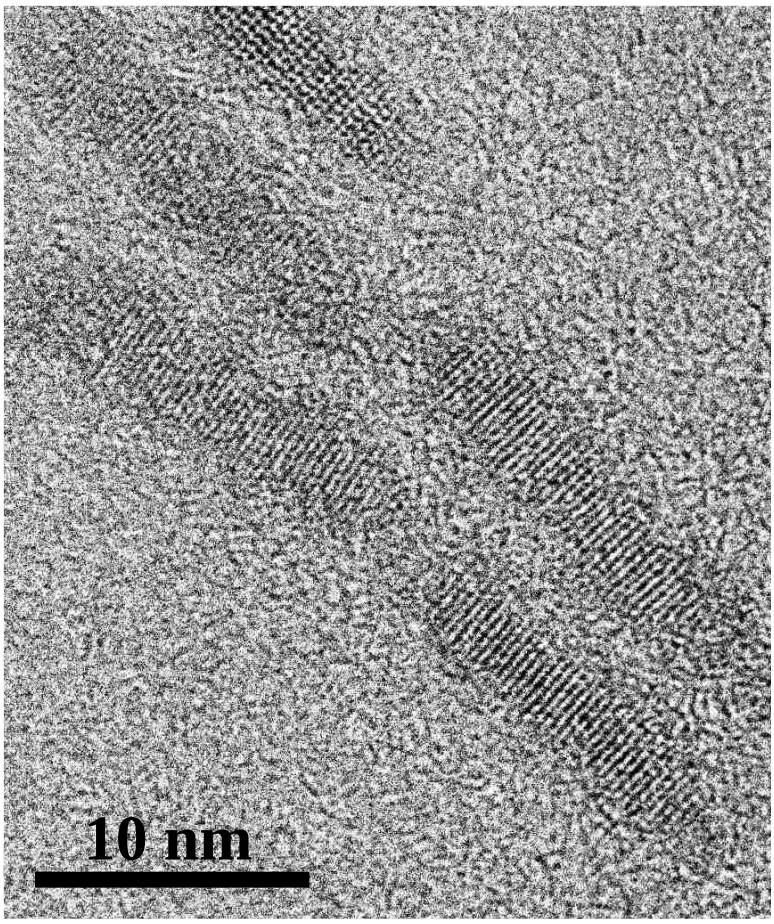

Figure 3-5. A HRTEM image of AR 3.5 NCs with an average width of 4.5 nm.

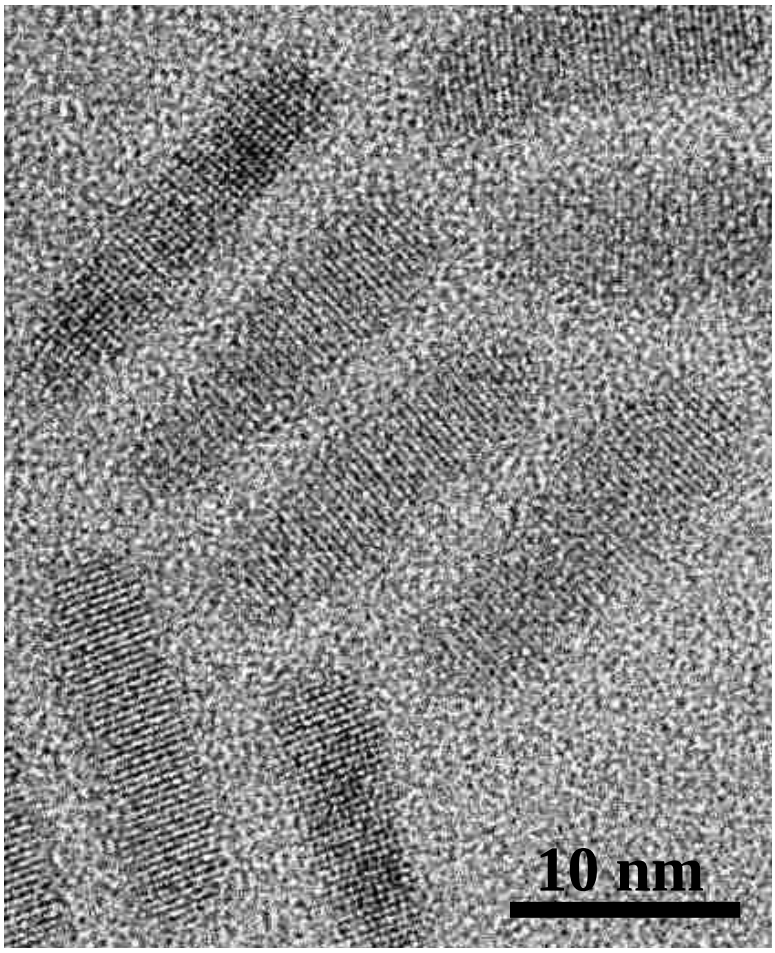

Figure 3-6. A HRTEM image of AR 4 NCs with an average width of 4.4 nm.

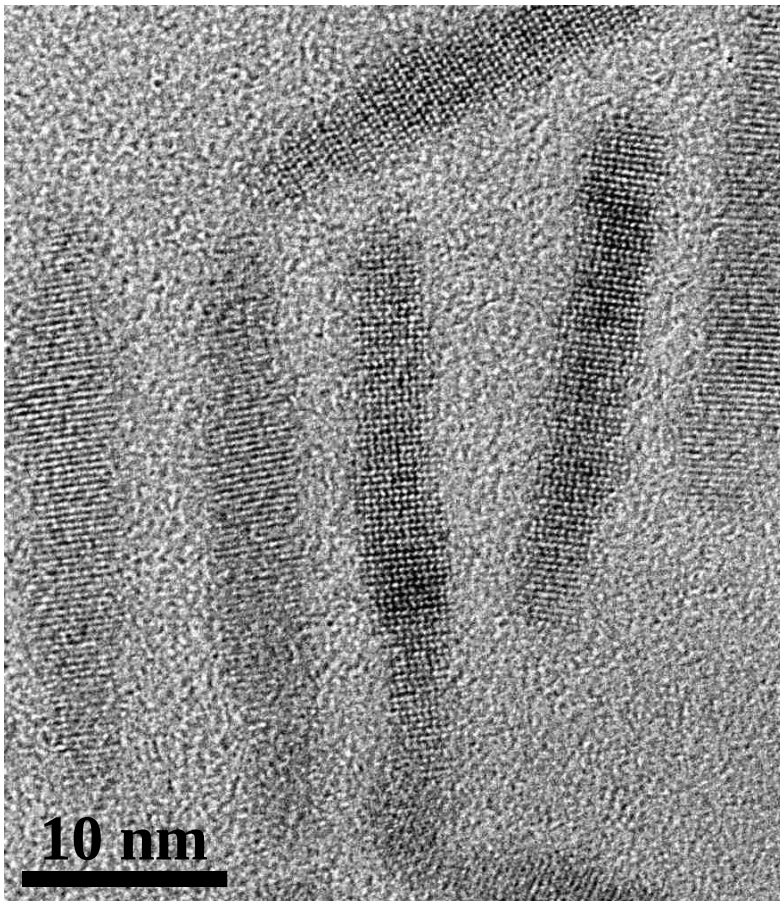

Figure 3-7. A HRTEM image of AR 6 NCs with an average width of 4.5 nm.

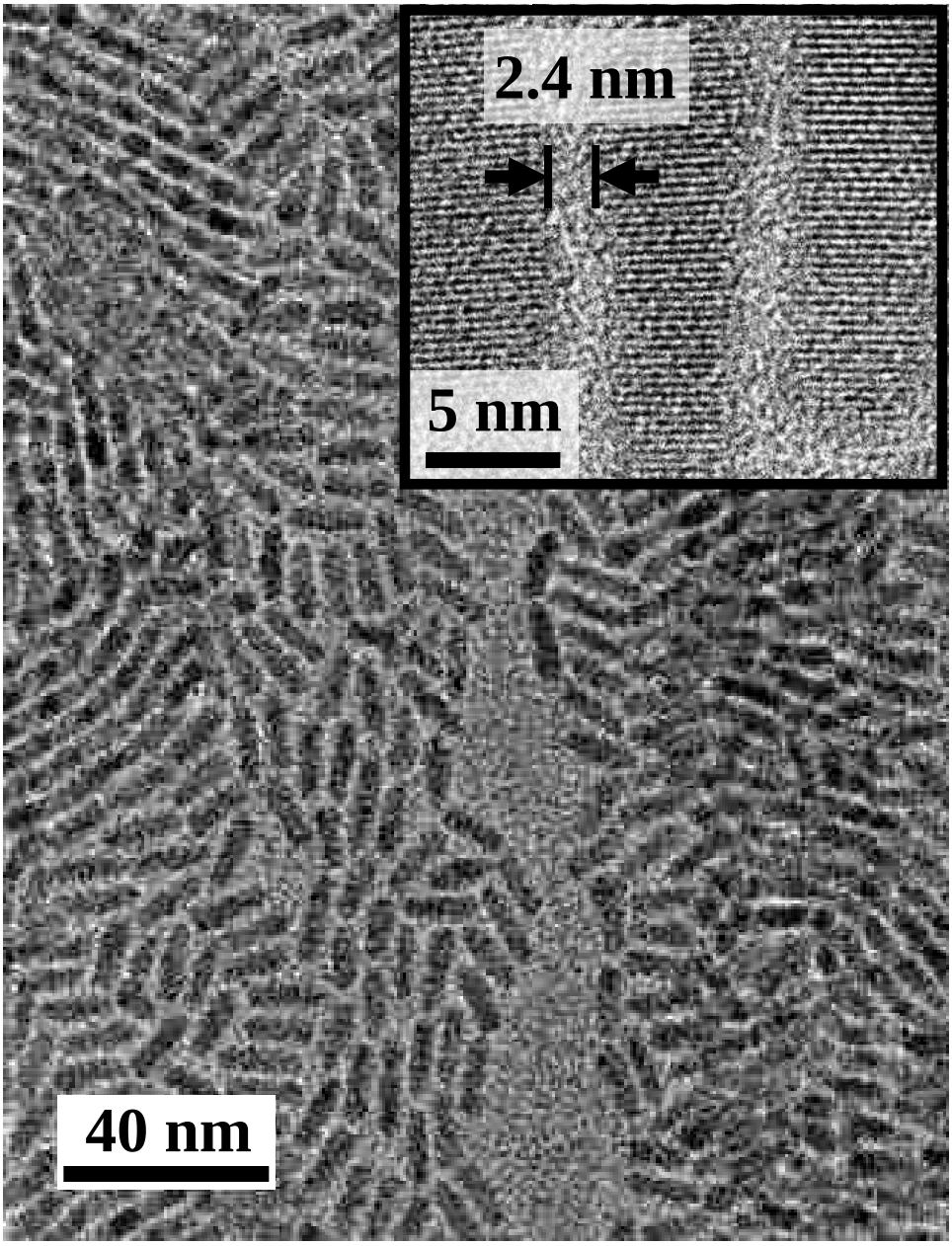

Figure 3-8. A TEM image showing areas of close-packed rods with the inset showing a HRTEM image with the rod to rod separation measured.

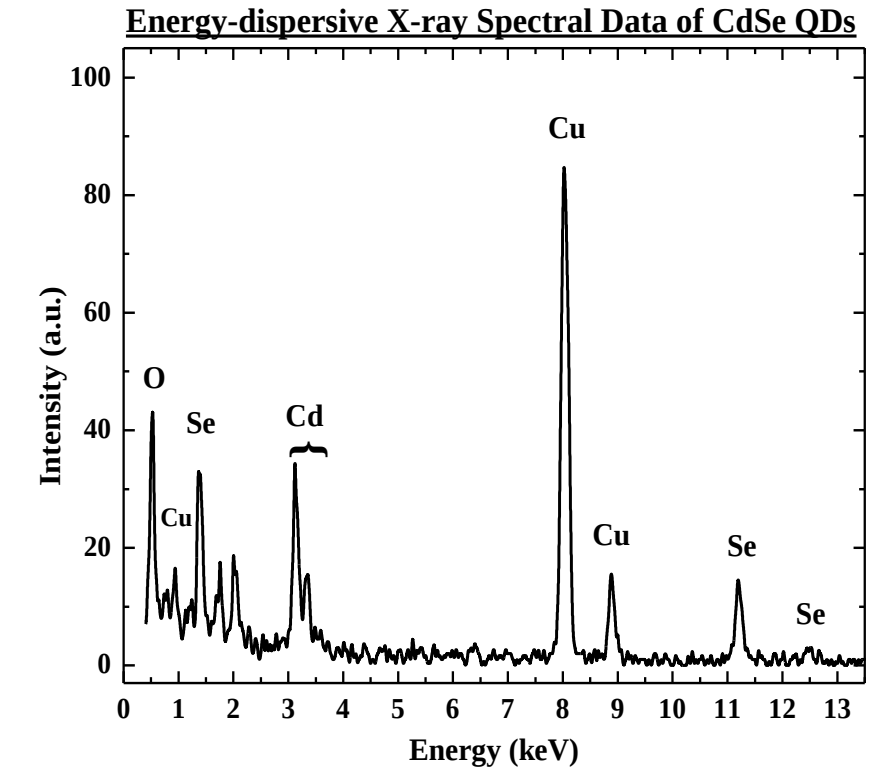

Figure 3-9. A plot of EDS data collected from CdSe NCs for AR 1.

A powder form of NCs can be characterized by using powder X-ray diffraction (PXRD). This technique can provide analysis of the bulk material present and provide insight into the average size of the nanocrystals, crystalline phase, and composition. The wurtzite crystal structure of CdSe is naturally anisotropic with the elongation in the hexagonal (0001) direction. Shown in Figure 3-10, the (0001) surface is Cd rich (light grey atoms) and conversely the $(000\bar{1})$ surface is Se rich (dark grey atoms) as compared to the side surfaces like the $(10\bar{1}0)$ and $(11\bar{2}0)$ facets which have alternating Cd-Se surface atoms [92]. In the PXRD data plotted for CdSe rods in Figure 3-11, the elongation of the crystal is observed as the (0002) peak with both the $(10\bar{1}0)$ and $(11\bar{2}0)$ peaks relating to the width of the NCs. The growth of the crystal is in an alternating Cd

and Se atomic planes that comprise an ABABAB stacked layer [93]. The growth is accelerated in the c-axis due to the phosphoric acid's affinity to bind stronger to Cd than Se atoms, or more simply put the sides are strongly passivated as compared to the ends of the NC.

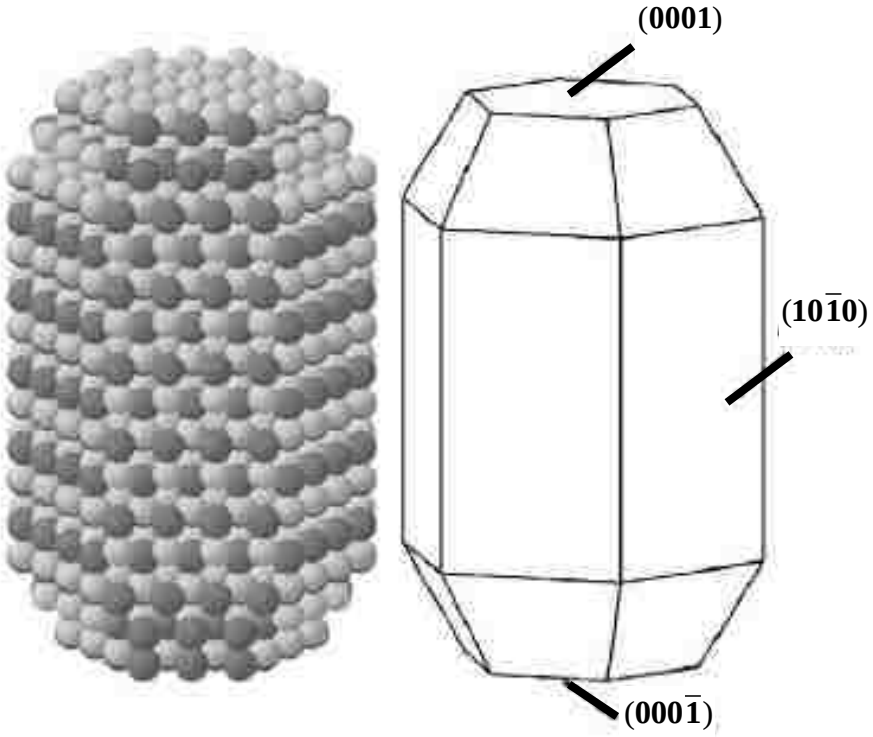

Figure 3-10. A diagram of the CdSe wurtzite structure, where Cd and Se atoms are shown in light grey and dark grey, respectively.

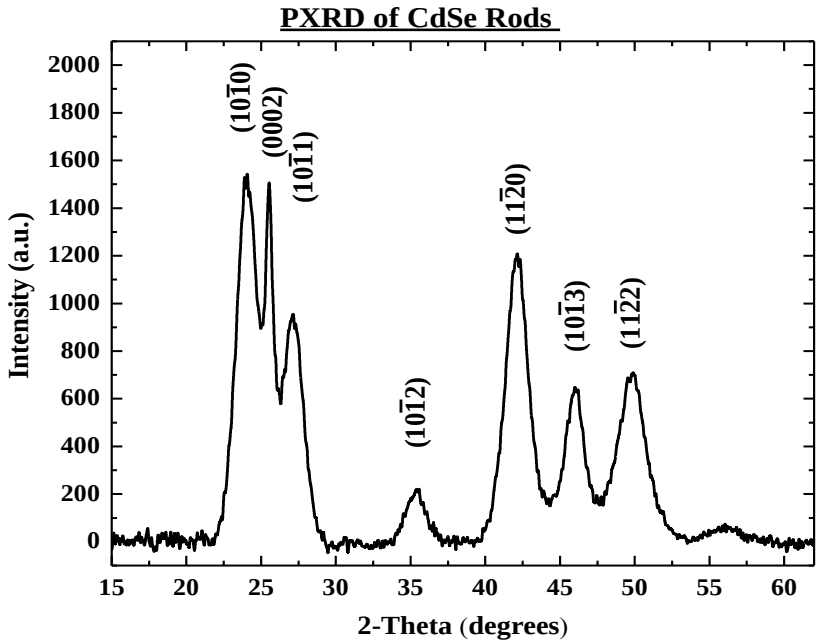

Figure 3-11. Plotted PXRD data for CdSe QRs that shows the characteristic elongation in the (0002) direction.

Another important property of the NC is the surface composition. During the synthesis of the NCs, surfactants are primarily used to control the growth kinetics, hinder particle agglomeration, and passivate the surface atoms from oxidation. The surfactant's pendant moiety also dictates the NC's miscibility in different solvents. In the case of TOP, TOPO or HDPA, all have a hydrocarbon chain that allows the NCs to be soluble in hexanes, chloroform, or toluene. Since the NC has a high surface area to volume ratio, characterization of the NC's surfactant is therefore crucial. One method for probing the chemical bonds of the NC's capping surfactant is by Fourier transform infrared spectroscopy (FTIR). Figure 3-12 shows the resulting FTIR spectra in the region of the C-H hydrocarbon chain for AR 1 NCs that are passivated with TOP and TOPO. For spheres, it has been previously reported that both TOP and TOPO passivate the NC's

surfaces with TOP having a stronger affinity for Se atoms while TOPO prefers Cd atoms [94]. The FTIR data was obtained by first taking a background of the KBr window, followed by drop casting of NCs suspended in toluene on to the KBr window. The toluene was allowed to evaporate, leaving behind the dry NCs. The four characteristic peaks from the TOP/TOPO C-H stretching modes are noted in Figure 3-12 as 2952, 2920, 2872, 2851 cm^{-1}. This region, among several others, is particularly different than the NCs that were produced with the addition of HDPA. General observation of the chemical structure of TOPO, TOP, and HDPA, in Figure 3-13, provides some insight into the molecular differences of the three species. In a similar FTIR sample preparation, AR 6 NCs were also analyzed. In the case of AR 6 NCs shown in Figure 3-14, the C-H stretching modes were observed at 2957, 2923, 2852 cm^{-1} and shows some distinction between TOP/TOPO and HDPA passivation. However, FTIR details that appropriately distinguish between TOP/TOPO and HDPA capped NCs would be observed in the region containing the O-H groups that the HDPA possess. Understanding how the HDPA binds to the surface would naturally be indicated by how the O-H groups behave. Several possibilities for how HDPA binds are: through the P=O group only (leaves both O-H groups protonated), through one O-H group (leaves one O-H group protonated), through both O-H groups (both de-protonated), which means that the HDPA could potentially have three bonds (tridentate binding). Basically, if an O-H group is unbound to the surface and considered to be non-interacting with the surface then a broad stretching peak would be observed at ~3500-3600 cm^{-1}. In the case of an O-H group participating in intermolecular binding, i.e. O-H-Cd, then a shift to 3200-3400 cm^{-1} would be observed. If the O-H groups were de-protonated, i.e. O-Cd or O-Se, then no broad peaks would be

observed in these regions. In Figure 3-14, it appears that some of the O-H groups of HDPA remain protonated (broad peak at 3000-3450 cm^{-1}) and actively participate in intermolecular bonding with the surface, which further suggests that the HDPA bonds differently on the atomically different crystal facets. Additional observed peaks for P=O at 1261 cm^{-1}, P-O a broad doublet at 1022 and 1092 cm^{-1}, and P-C at 802 cm^{-1}, all would be expected for NCs passivated by HDPA.

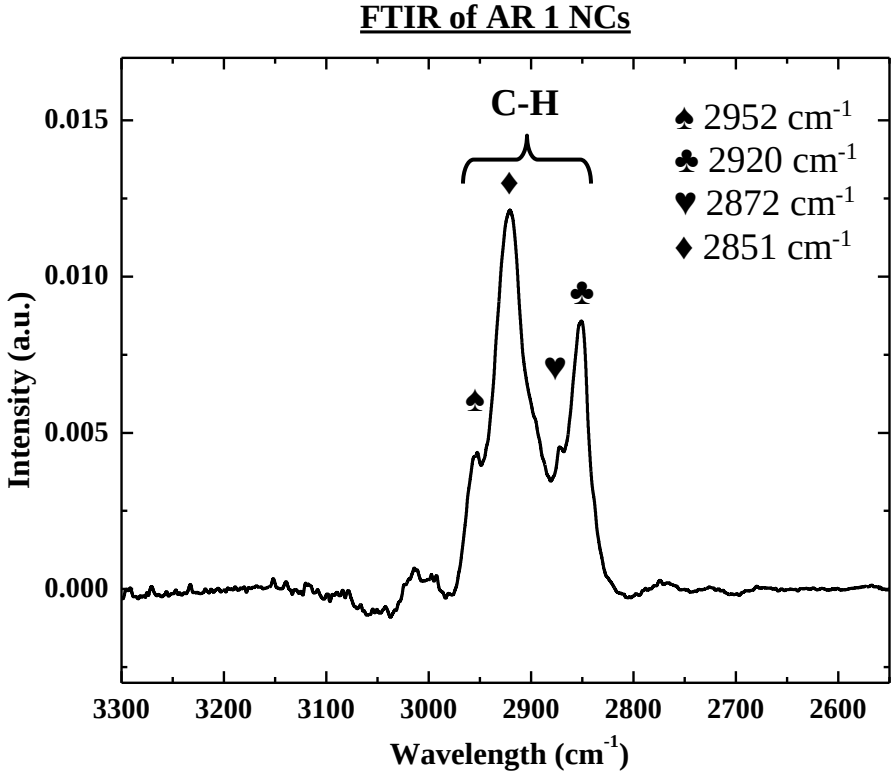

Figure 3-12. Plot of FTIR data showing the C-H stretching modes from AR 1 NCs passivated with TOP/TOPO.

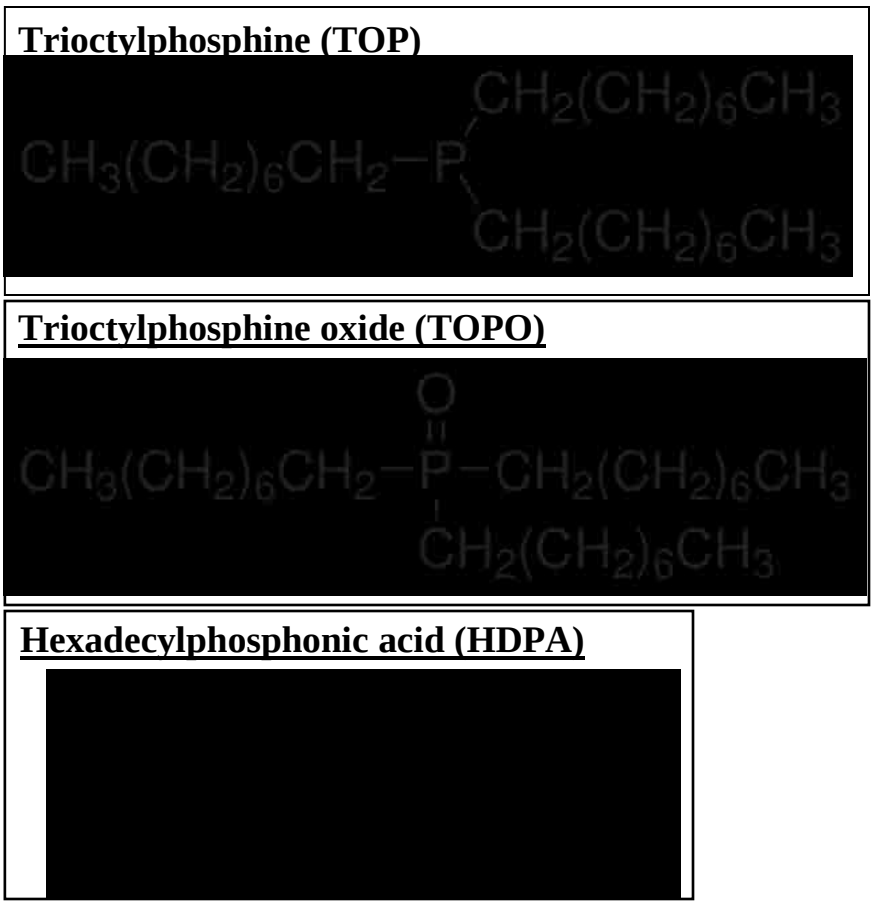

Figure 3-13. A comparison of the chemical structure of TOP, TOPO, and HDPA.

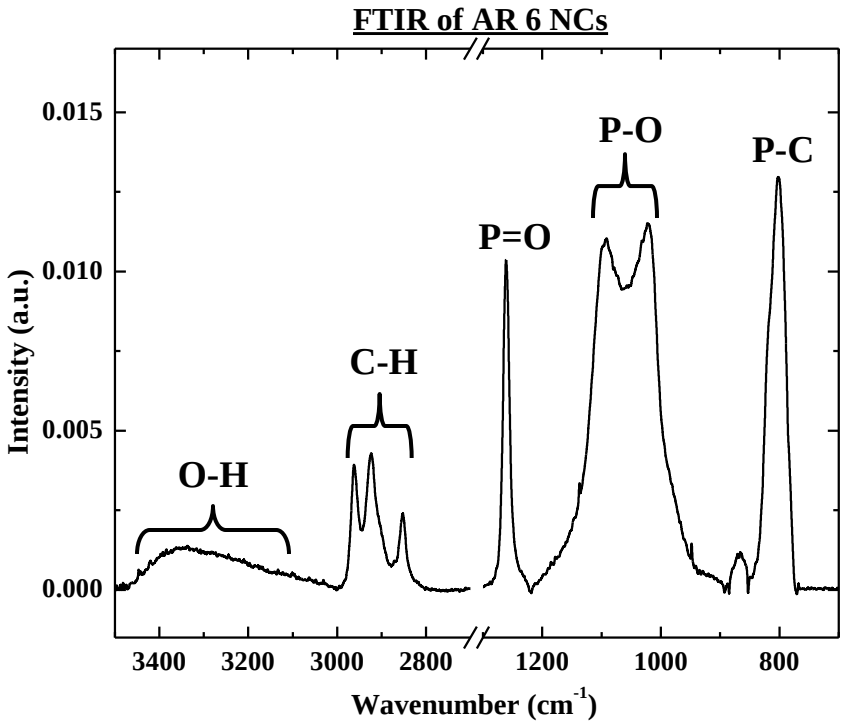

Figure 3-14. Plot of FTIR data showing several important stretching modes from AR 6 NCs passivated with HDPA.

Characterization of the optical properties of CdSe NCs is important to the fluorescent tracking capability by a laser-scanning confocal fluorescent microscope (LS-CFM). The emission properties from the NCs are best suited to be at higher wavelengths than the auto-fluorescence of the Si/SiO_2 nanochannels. For clear observation, the synthesis of CdSe NCs with a crystalline diameter of >4 nm provide emission wavelengths that are distinguishable from the background auto-fluorescence. Figure 3-15 plots the auto-fluorescence of the Si/SiO_2 nanochannels with the various AR NCs' emission when excited by a 488 argon laser. A clear distinction between the nanochannels auto-fluorescence and the NC's average fluorescence can be observed.

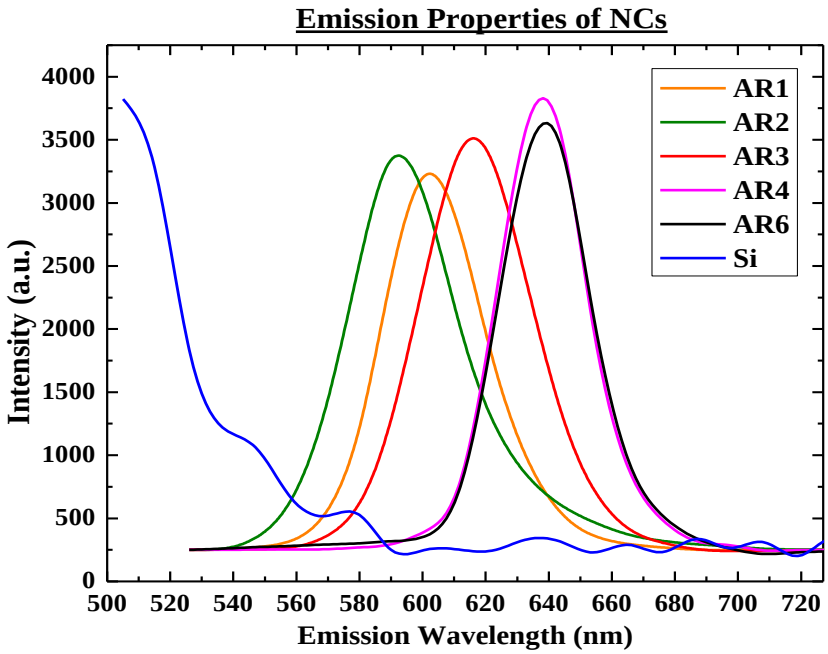

Figure 3-15. Collected fluorescent intensity from Si nanochannels and CdSe NCs under 488 nm excitation.

3.3 Summary of Synthesis and Characterization

The colloidal synthesis of CdSe NCs with differing AR has been developed. The importance of characterizing the NC's physical, surface, and optical properties is reported. Specifically, TEM is used to characterize the physical attributes of the NCs, PXRD and EDS confirm the chemical make-up of the NCs, FTIR is used to probe the surface chemistry, and LS-CFM is used to record the emission properties of the NCs. When combined, these methods provide a detailed understanding of the NCs synthesized and allow for their further use in experiments.

CHAPTER 4 FABRICATION OF NANOCHANNELS

4.1 Introduction to Fabrication Methods of Nanochannels

The interest in incorporating nano-scaled channel features by top-down or bottom-up methods has lead to considerable ingenuity in fabrication techniques [95, 96]. Several interesting methods of producing nanochannel structures have been previously described: electron-beam lithography [97-99], focused ion beam lithography [100, 101], nano-imprint lithography [102, 103], self-assembly lithography [104, 105], and interferometric lithography [106, 107].

Electron beam (e-beam) lithography has been widely used to produce nano-scaled features because the e-beam resolution is on the order of a few nanometers. The e-beam can be used to directly pattern photo-resist or other polymers by the beam of electrons, thus allowing the use of the patterns as masks, that can be etched, or serve as the nanochannels themselves. Similar to e-beam lithography, focused-ion beam (FIB) lithography can be used to directly etch nano-features into a substrate or mask. Typically, gallium ions are accelerated and focused into a beam that is used to etch the pattern into a substrate. The main draw-back of both processes is the slow, serial processing that is required for large area patterning. As a consequence, both methods are mostly used in the field of research and are not considered a viable option for commercial production.

Nano-imprint lithography requires a mold to be produced that allows the transfer of nano-features to be duplicated in substrates; the mold can be reused multiple times. The process in transferring the pattern can use a combination of thermal, pressure, or chemical methods to successfully transfer the pattern into a softer material, typically a plastic. Nano-imprint lithography does have several draw-backs. One of these issues is

when a pattern or feature size needs to be changed; a new mold must be created. Also, it is well known that the lifetime of any mold cannot be considered infinite as the stamp's feature quality will eventually degrade. It has also been noted that there are still challenges in producing different scales of feature sizes on a single mold. These issues do raise questions as to the application of nano-imprint lithography for commercial fabrication purposes.

Self-assembly lithography is considered to be a bottom-up approach to building nanofluidic channels. By using di-block copolymers to assist in the self assembly of the desired mask features or as an assembled sacrificial layer, the features of interest can be transferred to a substrate by etching. This technology is still relatively new in comparison to the previously mentioned methods and shows promise as an alternative approach to building nanochannels. The low cost process and scalability would suggest that this will become a popular method of fabrication.

Interferometric lithography (IL) is one of the most established methods of fabricating nanochannels. This technique is a maskless, inexpensive, and quick method to pattern large areas on substrates. Furthermore, IL easily allows the user to change the pitch size and channel width by changing the exposure angles and time. Additional exposures at different substrate orientations to the initial exposure can create other 2D and 3D repeating architectures, i.e. pillars, holes, and photonic lattice structures. The IL method is involved in the fabrication of the nanochannels used in the diffusion experiments and will be discussed in further detail.

4.2 Theory of Interferometric Lithography

Interferometric lithography is a robust fabrication technique for large area, maskless, periodic patterning of substrates. The basic principle of this technique is to use a coherent laser beam and reflect part of the beam, by a mirror, onto itself in the plane of a substrate. The crossing of the beams produces an interference pattern with a periodicity that can be modulated by the angle of the crossing beams. Figure 4-1 shows a top-down diagram of the setup used, and Figure 4-2 shows a near head-on view of the mirror and stage arrangement.

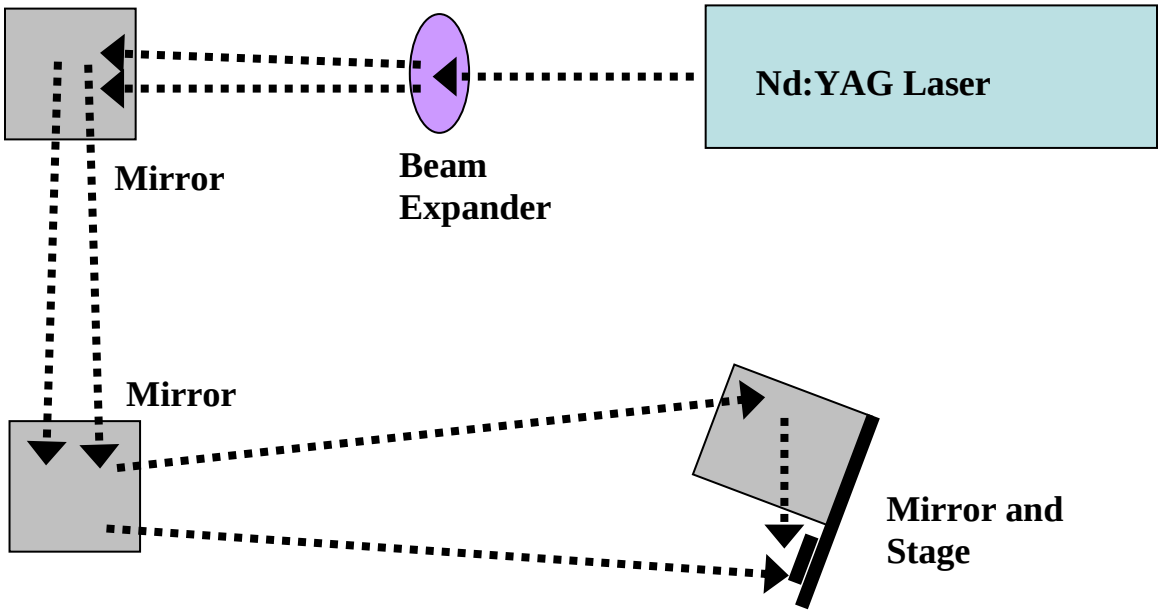

Figure 4-1. Schematic of interferometric lithography setup.

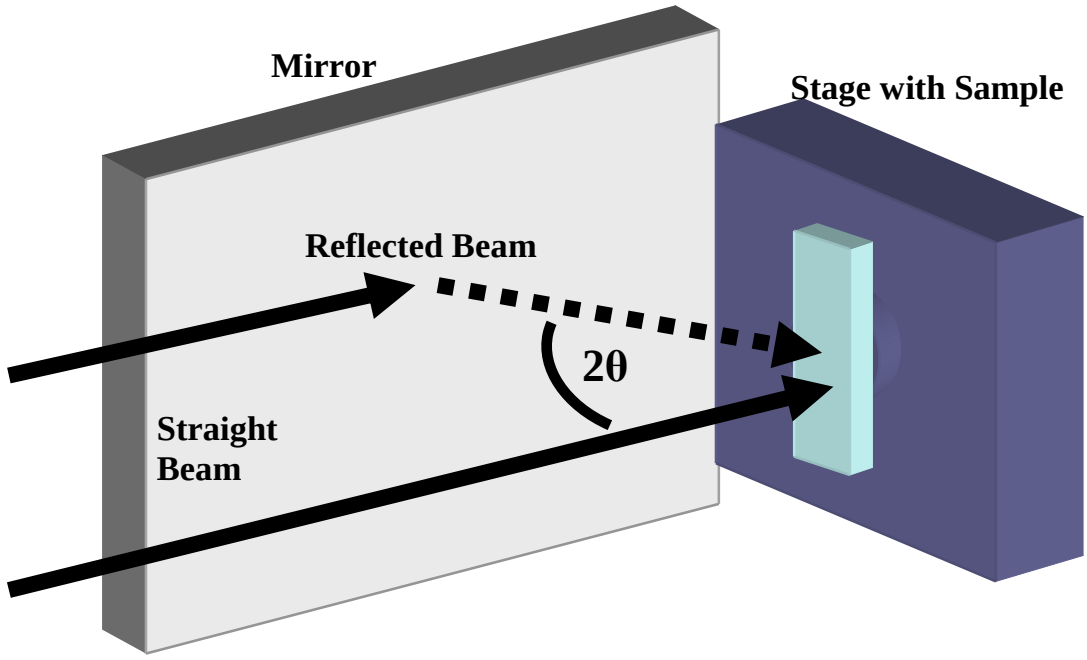

Figure 4-2. Schematic of the crossed beam on the substrate.

The mathematical description of the produced periodicity can be described by,

$$d = \frac{\lambda}{2\sin\theta} \tag{4-1}$$

where our experimental pitch (d) is 320 nm, and by using the third harmonic of a Nd:YAG laser with a wavelength (λ) of 355 nm, results in a crossing angle of 33.69°. Prior to exposing a substrate, the zero point for the perpendicular angle needs to be established by moving the stage in such a way as to produce no overlap of the reflected and straight beams. At this particular angle, the stage can then be properly aligned to the calculated crossing angle.

4.3 Fabrication of Nanochannel Chips

The fabrication process starts with a silicon wafer <100> that is diced into squares that measure 3 by 5 mm and will be called a substrate. These substrates are then cleaned by a typical RCA process, i.e. first rinsing with de-ionized water (DI H_2O), then a five minute dip in piranha acid (3:1 concentrated sulfuric acid: 30% solution of hydrogen peroxide) to remove organic contaminants and produce a thin chemical oxide on the silicon surface, followed by a two minute diluted (1:20, HF: DI H_2O) or a commercially available buffered (BOE 1:20) hydrofluoric acid dip that removes the thin oxide layer, and finally a DI H_2O rinse. The substrates are then blown dry by nitrogen gas. In general the substrates have two spin-coated layers applied before the IL exposure. All of the spin-coating is done at 4000 rpm for one minute, also referred to as recipe 1 on the spin-coaters. The first spin-coated layer is of NR7 anti-reflection coating (ARC), which is post baked in an oven at 175 ^{o}C for three minutes, allowed to cool to room temperature, and then a SPR-505A photo-resist (PR) that is diluted (1:5) by EC-11 is spin-coated. The PR is then baked on a 90 ^{o}C hot-plate for three minutes. At this point the substrates are ready for IL exposure as shown in step 3 of the process flow diagram (Figure 4-3).

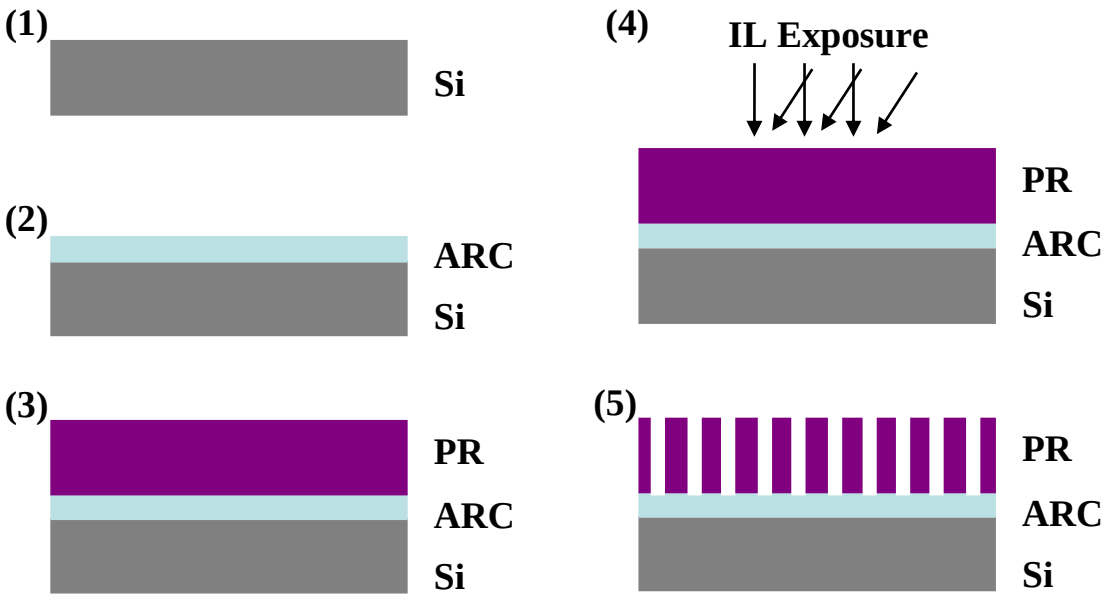

Figure 4-3. Fabrication diagram showing the steps up to development of the IL exposed sample.

Prior to the IL exposure of samples, the laser parameters need to be entered into the computer that controls the laser. Although the user can change many of the settings and still have successful IL patterns, the typical setting for repetition rate, energy, and exposure time were 60 Hz, 150 mJ, and 5 to 7 sec, respectively. It should be noted that prior to the substrate exposure, the exposure time and development is checked by using dummy samples that are viewed by the SEM. After the proper exposure time is set, the substrates are then exposed. After exposure the substrate is then heated at 110 ^{o}C on a hot plate for one minute. The substrate is allowed to cool to room temperature and then submerged into MF-702 developer for 45-60 sec, rinsed with DI H_2O, and blown dry by nitrogen resulting in Figure 4-3 (step 5).

Several important notes need to be detailed about the ARC layer and PR layer. The ARC layer effectively eliminates the standing wave that is generated during an IL

exposure, thus improving the wall geometry for the subsequent deposition of the metal hard mask. Figure 4-4 typifies the observed standing wave in the developed PR, while Figure 4-5 shows the usefulness of the ARC layer in eliminating the standing wave in the above PR layer.

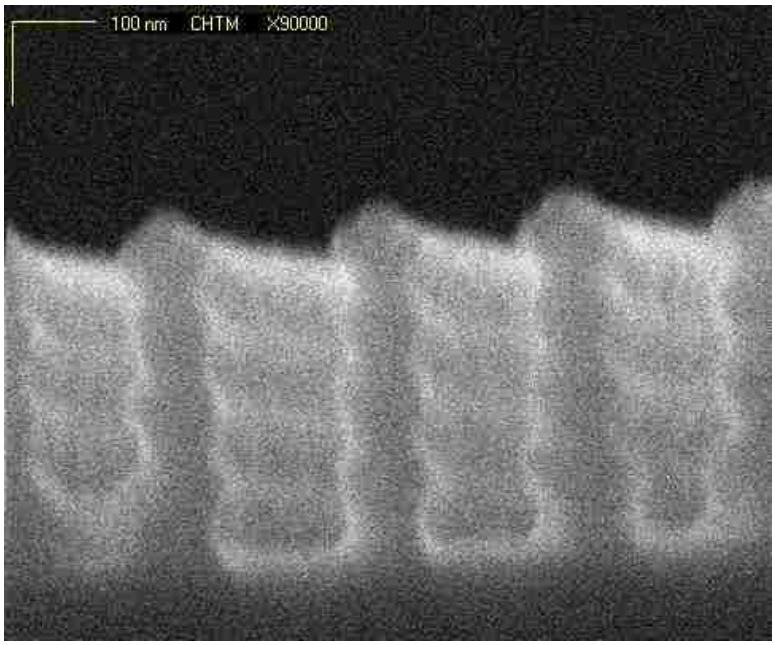

Figure 4-4. The photo-resist shows the standing wave that has developed on the sides of the walls because no anti-reflective coating was used.

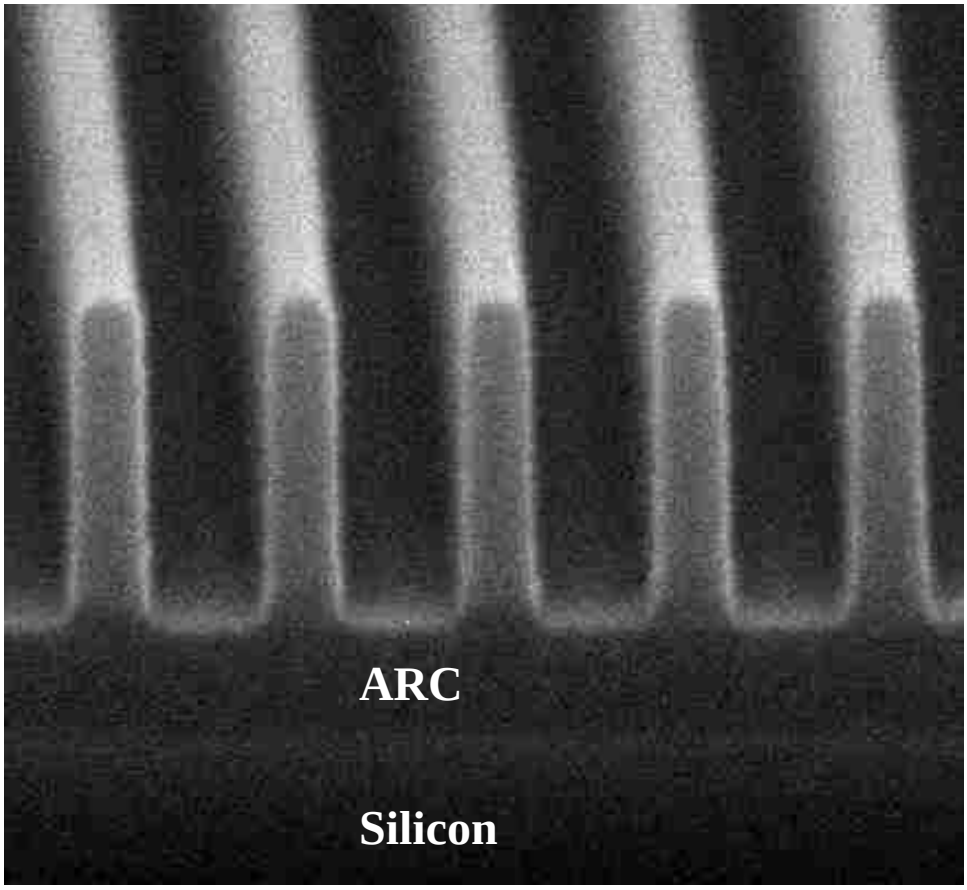

Figure 4-5. The anti-reflective coating has reduced the propagation of the standing wave in the developed photo-resist layer.

One of the biggest obstacles of the IL process is in the development of the trenches. In particular, an issue arises when the SPR-505A PR is spin-coated as received from the manufacturer in the described IL process. The as received spin-coated thickness is about 500 nm, and when developed the PR walls have an aspect ratio of five (thickness/width). At this aspect ratio the walls are subjected to capillary forces, from drying, that are strong enough to collapse the walls. A cross-sectional view of the wall collapse is shown in Figure 4-6 and a top-down view is shown in Figure 4-7. In order to improve the outcome and overall yield of nanochannel chips, the thickness of the PR was

optimized by diluting the SPR-505A with five parts of EC-11. The resulting spin-coated thickness was about 300 nm. The similarly developed thin PR can be seen in Figure 4-8.

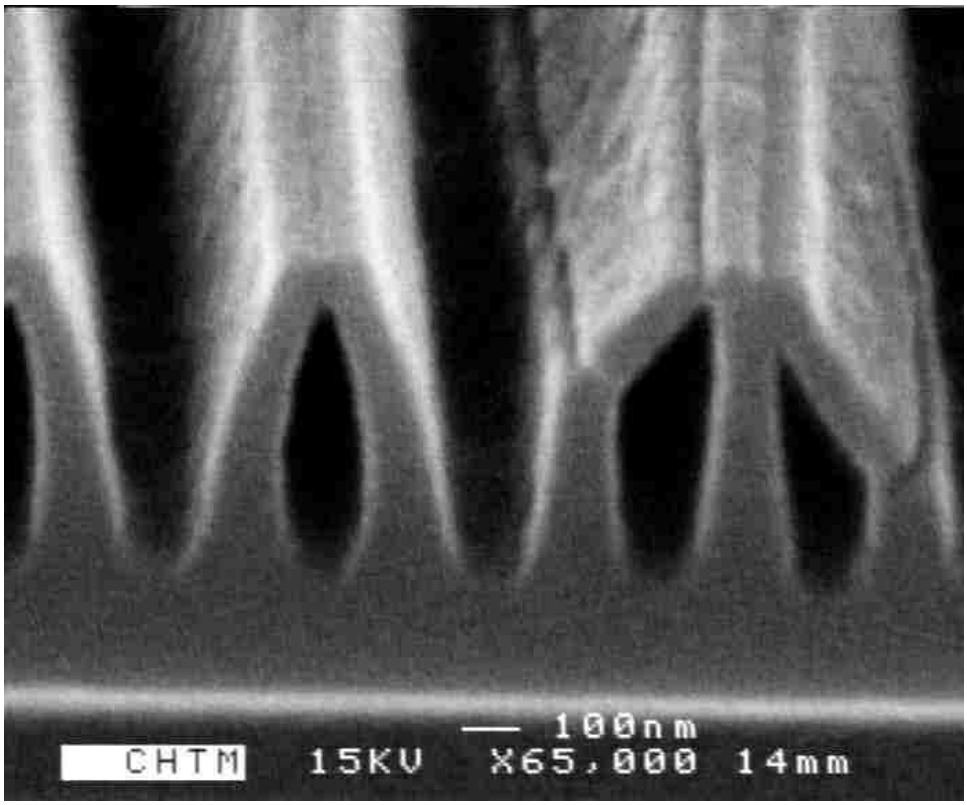

Figure 4-6. Cross-sectional SEM image of the thick photo-resist's collapse due to capillary forces experienced during drying.

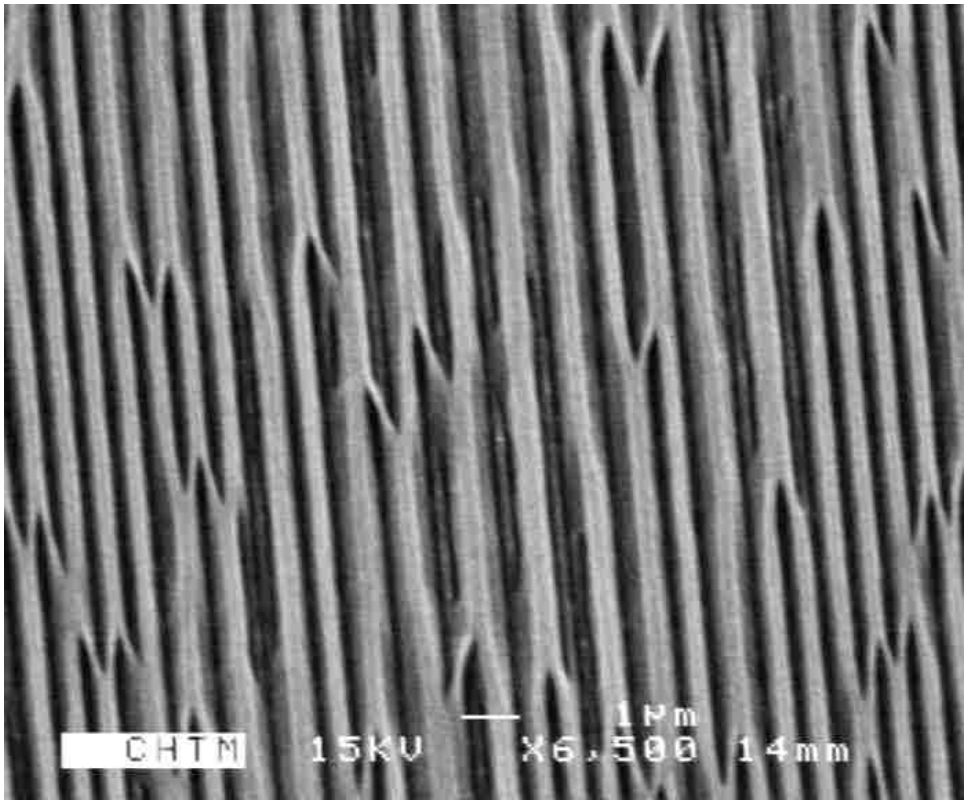

Figure 4-7. Top-down SEM image of the thick photo-resist's wall collapse.

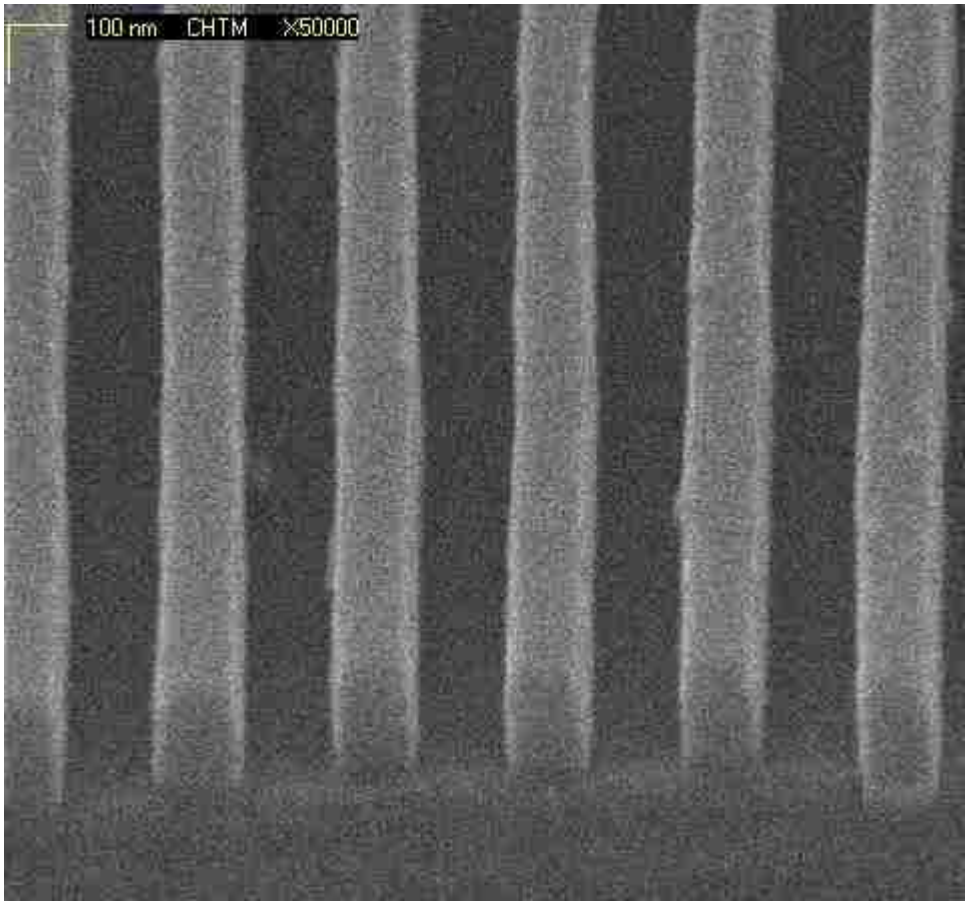

Figure 4-8. Cross-sectional SEM image of the diluted photo-resist after the IL exposure, development, and drying process.

After successful IL exposure and development, a metal evaporation step is required to produce a hard mask that is suitable for etching the channels into the silicon substrate. Metal evaporation is achieved by rastering an electron beam in a circular motion on the bottom of a carbon crucible containing the desired metal. The metal evaporation is operated within a chamber at $2E^{-6}$ torr with a deposition rate of 1 Å/sec until 40-50 nm of chrome is deposited. The metal evaporation chamber has a configuration where the substrates are mounted about two feet above the crucible with a shutter system in-between, and outfitted with a dielectric crystal that senses the

deposition rate at the substrate level, thus allowing for precise control of the deposition thickness, see Figure 4-9. The deposition of 50 nm of chrome produces a hard mask that is suitable for reactive ion etching (RIE), step 6 in Figure 4-10. Once the chrome has been deposited, a lift-off process removes the PR layer by an acetone spray gun. After the lift-off process shown, anisotropic RIE allows for the nanochannels to be etched into the underlying substrate, step 8 in Figure 4-10.

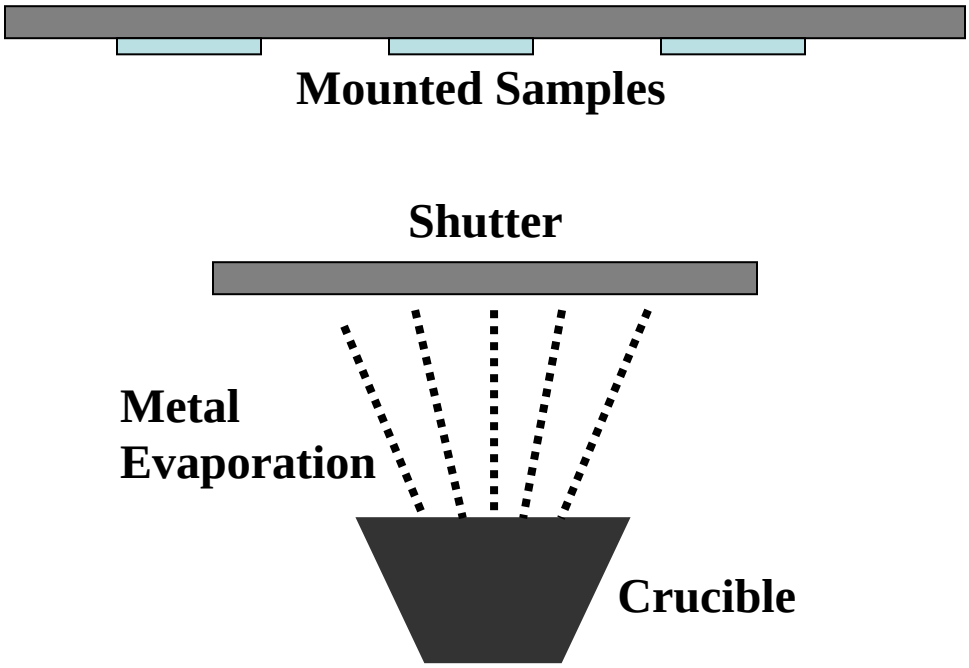

Figure 4-9. Schematic of the metal evaporation system.

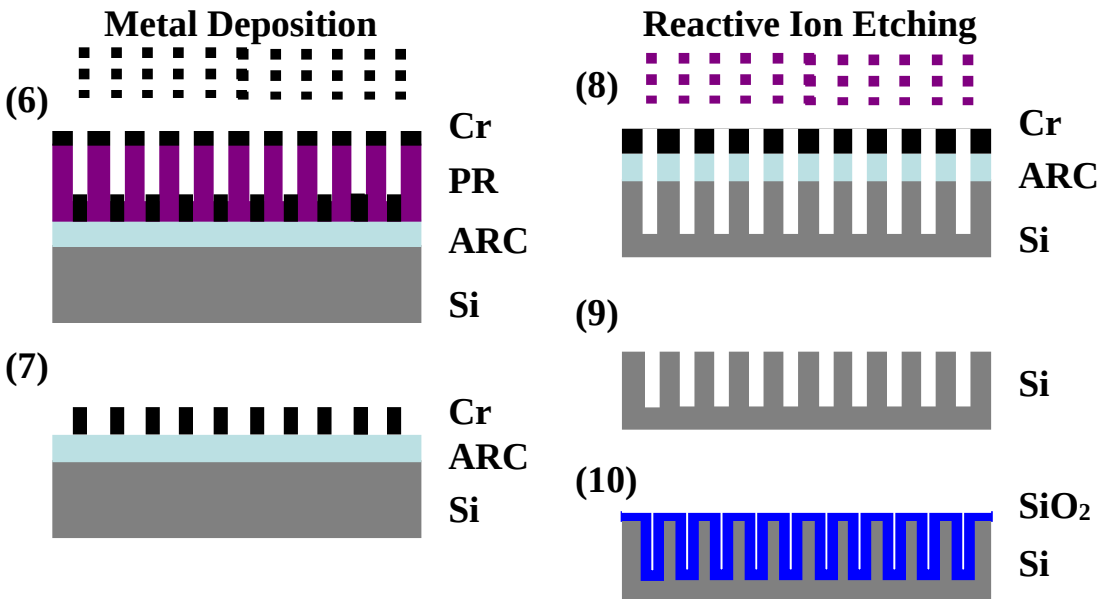

Figure 4-10. Diagram showing the fabrication steps up to the final oxidation of the etched channels.

Reactive ion etching of the chrome hard mask will only result in anisotropic features when the etching conditions for the tool are properly optimized. Optimization of the operating pressure (throttle), flow of etching gases O_2 and CHF_3, ion energy, and minimizing the reflected plate potential have the biggest impact on the quality of the resulting etch. The typical recipe used in etching the anisotropic channels into the substrate is a throttle of 20 mtorr, 90% CHF_3, 5% O_2, and a supplied power of 33.3% (100 mJ). The etch time is typically 32 minutes to produce 450 nm deep channels. After the etching is complete, the chrome mask and arc layer are removed by submerging the substrate into a piranha solution. The bare Si substrates are now individually inspected under the SEM to gauge the oxidation required to produce 100 nm wide channels. The substrates are appropriately segregated and then under-go a RCA clean before entering an 1100 ^{o}C oxidation furnace. The oxidation step, Figure 4-10 step 10, is then verified by

SEM imaging of the channel widths by a top-down view, Figure 4-11, although a cross-sectional view is also provided, Figure 4-12.

Figure 4-11. A top-down SEM image of the thermally oxidized Si nanochannels.

Figure 4-12. A cross-sectional SEM image showing a thick thermally grown oxide layer on the Si channels.

At this point the nanochannel substrate only requires the bonding of a pyrex cover to complete the nanofluidic channels. The pyrex covers are first diced into 1 cm x 3 cm rectangles and thermally bonded to a glass slide by crystal bond. The diced pyrex then has 4 mm holes drilled into both ends by using a diamond drill bit and a drill press. The pyrex covers are then thermally released from the glass and excess crystal bond is removed by a warm acetone solution. A rigorous cleaning is performed by alternating between piranha and DI H_2O solutions several times in order to remove crystal bond and

pyrex particles. The pyrex covers are then rinsed by DI H_2O and carefully applied to the nanochannel substrate. The capillary force between the pyrex and substrate holds them together while an anodic bonding setup is prepared, see Figure 4-13. The best anodic bonding process requires a temperature of 350 ^oC, supplied by an aluminum hot plate, and a polished aluminum top contact plate. The voltage supplied to create atomic bonding between the SiO_2 interfaces was found to be optimal at 1300 V held for 30 seconds. The bonding process produces hazing at the top of the pyrex that needs to be polished off before the nanofluidic chips can be used. The nanofluidic chip is first filled with DI H_2O in both wells before lapping with a 15 μm pad (2 min), a 9 μm pad (3 min), a 6 μm pad (3 min), a 3 μm pad (3 min), and finally a 1 μm pad (5 min). The nanofluidic chip is then cleaned by alternating between piranha and DI H_2O several times with the cleaned chip being stored in a fresh DI H_2O solution.

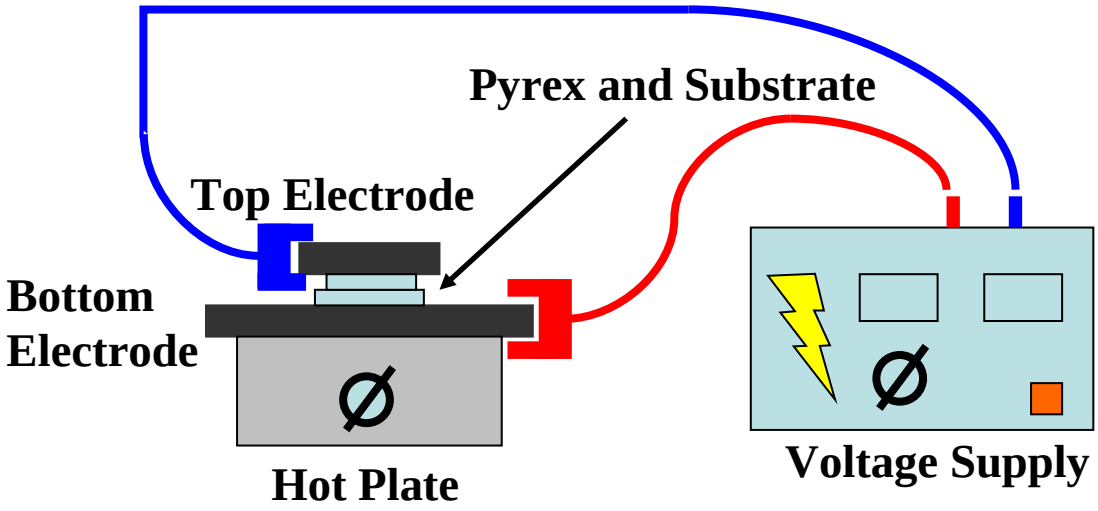

Figure 4-13. Schematic of the anodic bonding setup.

4.4 Summary of Fabrication

Interferometric lithography is a reliable technique used to fabricate large areas of nanochannels on a substrate. By optimizing several of the discussed processes, i.e. IL and RIE, the production of high quality and high yield nanofluidic channels is successfully accomplished. The flexibility of the IL can also allow smaller fluidic channels to be fabricated, if so desired, by changing the pitch of exposure and subsequent oxidation. Future fabrication of nanofluidic devices appears to have a strong outlook when using the techniques, tools, and processes described within this chapter.

CHAPTER 5 EXPERIMENTAL SETUP FOR DIFFUSION STUDIES

5.1 Introduction

In an attempt to better understand how the NC's physical dimensions behave in nanofluidic confines, a fundamental study of the diffusion process was examined by using elongated hydrophobic NCs suspended in a toluene solution. Although the design and operating principles of the nanofluidic apparatus are relatively simple, the experiments should be able to quantify how the NC's aspect ratio influences the diffusion coefficient and the amount of NCs within the nanochannels as a function of distance and time. To monitor the diffusion process and quantify the amount of NCs in the nanochannels, a laser scanning confocal fluorescent microscope (LS-CFM) is used to aid in imaging the photoluminescent (PL) NCs as they proceed into the nanochannels as a function of time. This section describes how the diffusion experiments were setup, run, and calibrated to quantify the results.

5.2 Calibration of Detected Fluorescence versus Concentration

In order to accurately account for the NC's concentration as observed by the LS-CFM, a calibration of the NC's fluorescent intensity compared to different dilutions needs to be correlated. By accurately weighing the NCs and adding the appropriate amount of toluene solution to produce an initial 1 mg/cm^3 solution, additional step-wise dilutions can be observed under the LS-CFM. Shown in Figure 5-1 is a representative data set (AR 4) of several dilutions that were imaged by the LS-CFM with the corresponding PL intensity plotted. Each of the images captured (2000 μm^2) at a specific dilution, several examples shown on the right side of Figure 5-1, are probed with a 50 μm

in diameter circle that averages the area's pixel intensity at each scanned wavelength. Typically, 4 scans are taken from wavelengths of 520 nm to 740 nm with a resolution of 10 nm and the pixels are then averaged for each captured image. The intensity data gathered at each dilution can then be integrated and plotted, thus producing a linear calibration of the intensity verse concentration as shown in Figure 5-2. The area averaged calibrations are typically used for plotting time dependent data such as the entrance concentration (concentration vs time). Additional calibration at a specific wavelength can also be fitted and used effectively for spatial dependent plots such as the diffusion curve (concentration vs distance). Because the quantum yield of the NCs differs from synthesis to synthesis, all of the various AR NCs need to be calibrated. Although the bulk dilutions are imaged in the reservoirs of the nanochannel chips, the calibration can not be directly applied to volumes of a smaller scale, such as micro- or nanochannels.

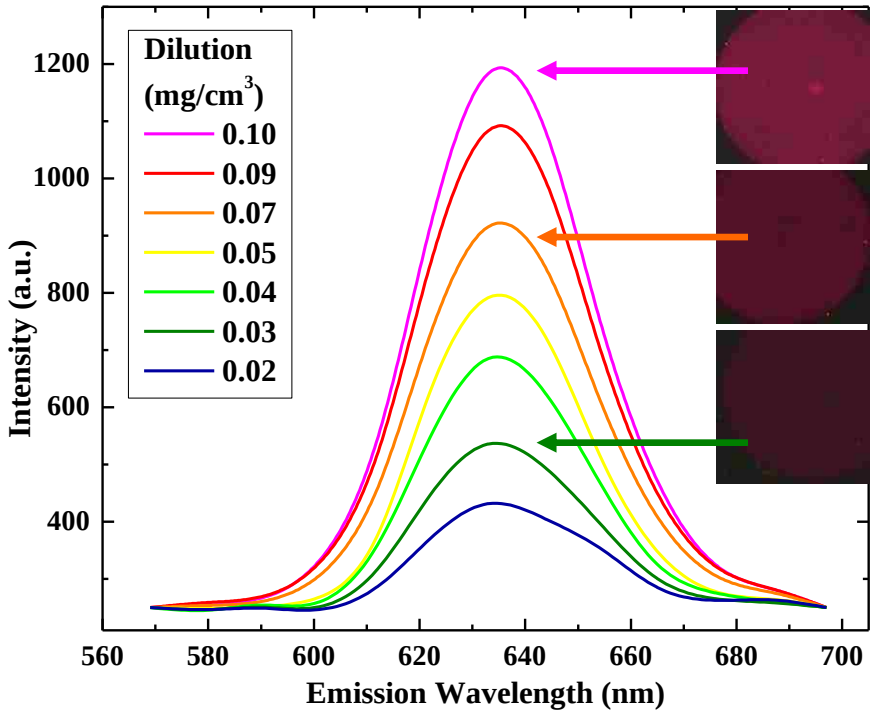

Figure 5-1. Plot of intensity data from LS-CFM for several dilutions of AR 4 NCs. On the right side are the corresponding LS-CFM images of the bulk reservoir.

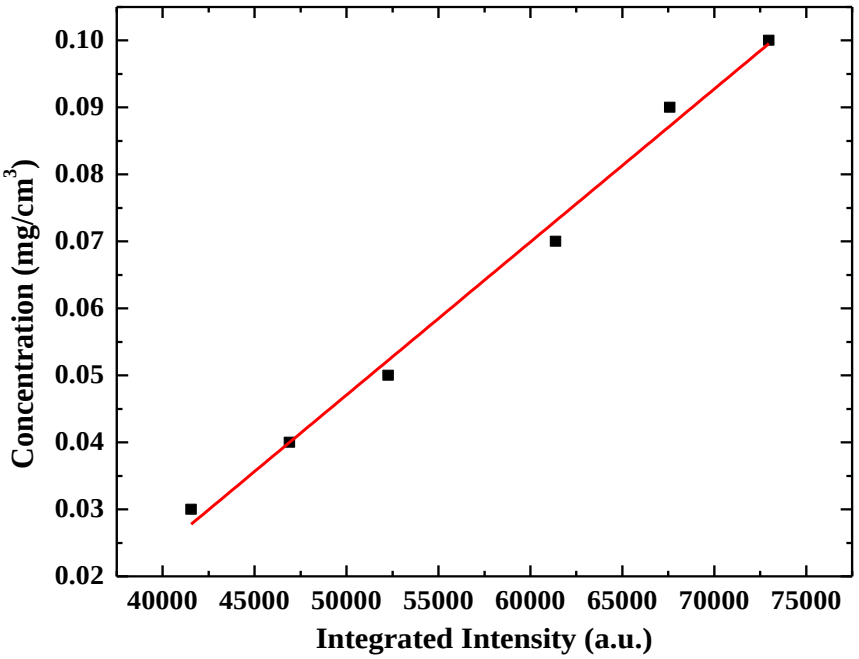

Figure 5-2. A plot of AR 4 NC's calibration data (black squares) from probing different dilutions and integrating the emission intensity. Shown in red is the fitted linear relationship between the concentration and intensity that produces a bulk calibration equation.

To properly and quantitatively measure the NC concentration in the nanochannels, one must account for the limited depth of the nanochannels compared to the reservoir's depth used in calibration. We note that the well depth (~2 mm) is much greater than the probing depth of LS-CFM (~16 μm), the latter of which is much greater than the nanochannel depth (400 nm). In order to probe the effective difference in depth as it relates to intensity, the PL intensity of Rhodamine B (~1.6 nm in diameter) in a chloroform solution (2×10^{-5} M) is measured in the reservoir and then from a 400-nm-deep by 50-μm-wide microchannel. The introduction of the Rhodamine B solution to a

dry microchannel allowed for the bulk solution to be pulled into the microchannel by capillary force. The ratio between the bulk reservoir and the microchannel's integrated intensities was determined to be on average 43±4, thus giving credence to the depth correction factor (f_d) of 40 and further resolving the LS-CFM's penetration depth as ~16 μm. The reason for measuring the intensity from a microchannel rather than from an array of nanochannels is to prevent possible partitioning of the dye molecules at or near the nanochannel entrances. Additionally, nanochannels have a much larger surface area that could allow for significant wall interactions, for example adsorption, to interfere with the true calibration of the depth.

In addition to the depth correction, the PL intensity from the nanochannels is measured from a limited volume due to the periodic channel sidewalls that occupy a "non-fluorescent" dead volume. Therefore, one must make an additional geometric correction to the calibration to account for the non-fluorescent volume. To illustrate, for 100-nm-wide, 400-nm-deep, 320-nm-pitch nanochannels shown in the inset of Fig. 1(b), the geometric correction factor (f_g) is the pitch-to-channel-width ratio (~3). Thus, for the same observed PL intensity from the reservoir and from the nanochannels, the NC concentration would be 120 ($f_v = f_d \times f_g$) times greater in the nanochannels than in the reservoir. Rhodamine B was experimentally observed in these same nanochannels to have an f_v on average of 435±64, approximately 3.5 times greater then the physical dimensions would indicate, suggesting that <30% of the reservoir concentration is allowed into the nanochannels and therefore a partitioning effect is observed for small dyes. The correction term of 120 (f_v) is considered to be constant in all of our analysis of AR NCs and our general linear calibration equation takes the form of:

$$Concentration = f_v \; x \; Slope \; x \; Intensity \; - \; Intercept \, , \tag{5-1}$$

where our typical value for the *Intercept* is 0, the *Slope* value is the slope from the linear fitting of the NC's bulk calibration, and *Intensity* is from the experiment's integrated value above background noise.

5.3 Nanochannel Preparation

Before the diffusion experiments are started, the preparation of the nanochannel chip needs to be discussed. After the nanochannel chip is fully fabricated and cleaned, as discussed previously, the chip needs to be thoroughly dried. This is an important step in assuring that water molecules are completely removed prior to the introduction of toluene. The chip is therefore put on a hot plate at 160 ^{o}C for one hour. After one hour, the chip is removed and allowed to cool on an aluminum block for five minutes. Once the chip has cooled, the chip is observed under a Nomarski microscope as toluene is added to one reservoir. Although the nanochannels themselves are beyond the diffraction limit of light and therefore cannot be individually observed under an optical microscope, the 50 μm patterned areas can be collectively viewed as a fluid is introduced. The difference in the image's contrast from the empty microchannel region, containing only air, and the toluene filled region allows for observation of the filling process, shown in Figure 5-3. Specifically, the difference in refractive indices between the pyrex (n = 1.47) and the vacant channel (n = 1.00), area containing air, was filled with toluene (n = 1.49) and subsequently reduces the contrast. The capillary force induces the toluene to fill the 50 μm patterned nanochannel areas within one minute, which averages to a filling speed of

approximately 0.02 cm/sec. At this time it is noted whether or not there are any issues with the channels, i.e. blockage of the channels, slow flow resulting from dirty channels, misalignment of the nanochannels with respect to the micro-patterned viewing region or pyrex bonding issues. After five minutes under these conditions, toluene is added to the opposite reservoir.

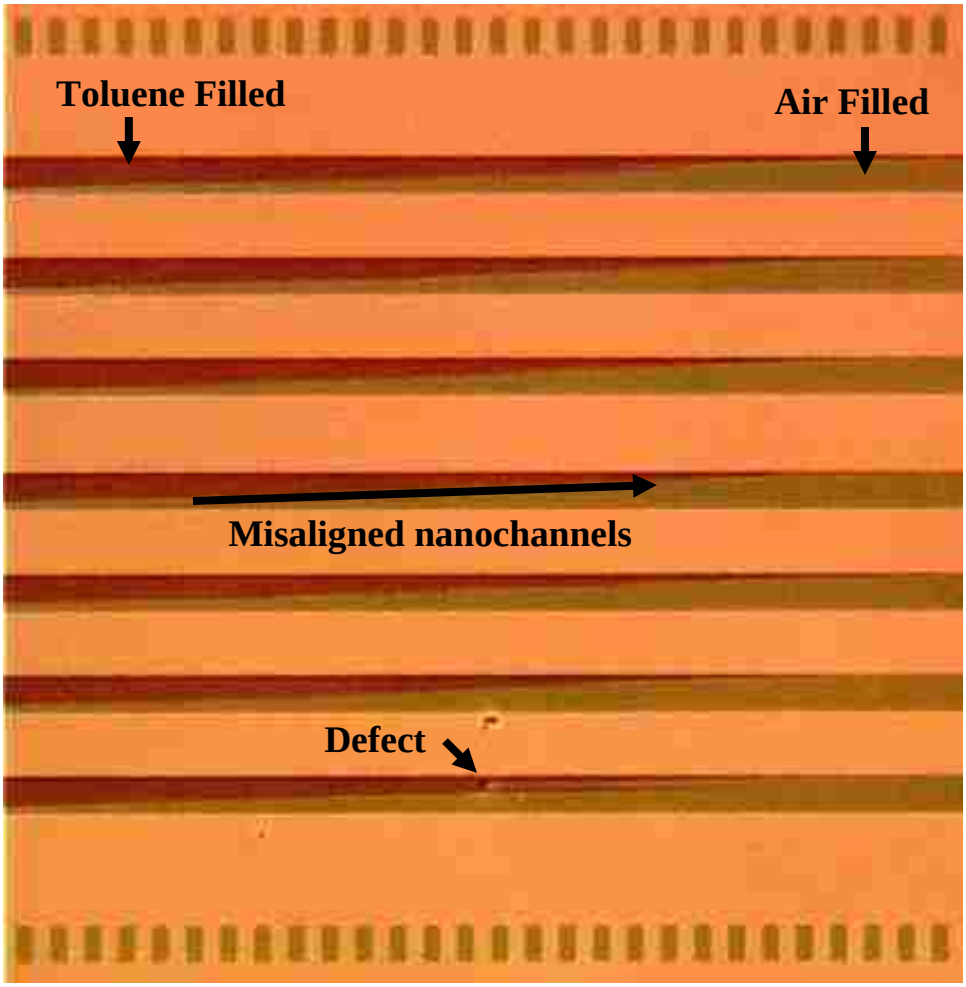

Figure 5-3. A Nomarski microscope image capturing the capillary filling from left to right of the 50 μm wide viewing area that contains the horizontal nanochannels. In this case, the channels are slightly misaligned and a defect that impedes the flow is shown in the bottom channel; this nanochannel chip was not used in the diffusion experiments.

5.4 Procedure for Initial Forward Diffusion Experiments

Once properly filled chips have been established, full submersion in toluene for an additional 72 hours allows for equilibrium to be fully established between the nanochannel walls and the toluene solution. This extra time in toluene further ensures the repeatability of the diffusion experiments by allowing for possible out gassing of trapped air. The forward diffusion experiments consist of the prepared nanochannel chip, where the reservoirs are still filled with toluene, which is gently submerged into a screw-top vial containing the prepared NC solution. The vial and nanochannel chip are stored in a horizontal position so that the NC solution covers the chip's reservoirs completely, as shown in Figure 5-4. Periodically, the nanochannel chip is removed from the solution and viewed under a laser scanning confocal fluorescent microscope (LS-CFM) and pictures are recorded of the diffusion process.

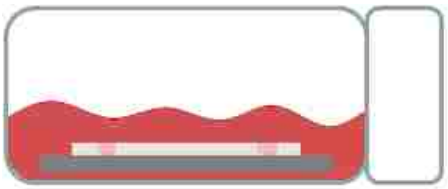

Figure 5-4. A diagram of a screw-top vial containing the nanochannel chip submerged in the NC solution and stored in this position during the diffusion process.

5.5 Procedure for Reverse Diffusion Experiments

Following the forward diffusion experiment, we can then study the diffusion of the NCs in the nanochannels as they back diffuse into a toluene reservoir. This reverse diffusion process is started by diluting the reservoir, that previously contained the NC solution, to a point where the reservoir is considered to be only neat toluene. Specifically, the whole nanochannel substrate is submerged into a series of three neat toluene batches over a 5 minute period to rinse the exterior surface of the substrate and to remove residual NCs from the entrance reservoirs. Following the rinse step, the nanochannel substrate is submerged into another neat toluene solution contained in a screw-top vial. At this point, LS-CFM images are taken periodically as a function of time to track the out-diffusion of the NCs from within the nanochannels. The experimental conditions are the same as the forward diffusion experiments.

5.6 Summary

Several diffusion experiments have been undertaken to try and extract valuable information as to how the variation of a NC's aspect ratio affects the diffusion and wall adsorption processes. This section has laid out the experiments used to try a garner a better understanding of the system involved. In order to de-convolute the data and to further understand the possible mechanisms in the diffusion and adsorption process, modeling of the system needs to be undertaken.

CHAPTER 6 MODELING

6.1 Introduction

In brief, the experimental system includes aspect-ratio-dependent diffusion of CdSe NCs suspended in toluene as they advance into 100-nm-wide by 400-nm-deep slit-like nanochannels. Toluene is considered to be an aprotic solution in the system and therefore minimizes any wall-NC and NC-NC charge-based interactions. The aprotic condition allows the focus of the experiments to be on the geometric dependence of the NCs' diffusion. The fluorescent intensity of CdSe NCs is used to quantify the NC concentration within the nanochannels, thus allowing the concentration to be observed as a function of time and distance from the channel inlet. In general, the observed time evolution of the concentration profile would suggest that NCs readily adsorb on the SiO_2 walls. The wall adsorption process accounts for the significant increase of NCs observed within the nanochannels as compared to the initial bulk reservoir solution outside of the channels.

In the following sections, several models of increasing complexity will be presented to demonstrate the development of the final two-site adsorption model. The modeling starts with Fick's second law as the mathematical description for NCs solely diffusing into the nanochannels. We further explore several possible boundary conditions to account for the observed experimental profiles, such as the empirical boundary condition used in the single site model. Simulation by Mathematica 7.0 is used to test the possible models and respective parameters to produce a best fit for the observed forward diffusion profiles. The resulting two-site model extracted parameters include two equilibrium constants, two desorption constants, a single adsorption constant, and the

diffusion coefficient. The results of the single-site and two-site model will be discussed in detail in the Results and Discussion (Chapter 7) portion of the paper.

6.2 Simulation of Several Diffusion Models

Since we observe a significant increase in the concentration within our nanochannels, typically >4 times the reservoir concentration, we consider several transport equations and boundary conditions (BCs) that could be used to mimic these concentration profiles. To capture the various observed diffusion profiles, we have simulated several possible diffusion models by: (i) adding a BC that mimics a possible diffusional hindrance or partitioning at the channel's entrance, (ii) including an expression for wall adsorption as a heterogeneous BC using an empirically derived fit for the saturation concentration as a function of time, and (iii) directly including the wall adsorption as a homogenous term in the transport equation, and allowing the concentration at the BC to be expressed from the empirically fit data in terms of a characteristic concentration and rise time.

In the case of our experimental system, we are observing a non-steady state diffusion process with no convective forces or gravitational effects. The NC number concentration in the reservoir is on the order of 10^{14} to 10^{15} cm^{-3} for the described 1.0 mg cm^{-3} mass concentration used in our experiments. Poniewierski reported a reduced number density (c_b) of 4.19 that is required for spherocylinders to have sufficient NC-NC interactions that lead to both ordering at the channel walls and the isotropic-nematic phase transition observed in the bulk solution [108]. Mao *et al.* further studied high AR spherocylinders and defined the reduced number density (c_b) as

$$c_b = \rho \times d \times l^2 \ , \tag{6-1}$$

where ρ, d, and l denote the NC's number density, diameter, and length, respectively [109]. If we consider the total number density of both the adsorbed NCs and freely diffusive NCs within our channels near equilibrium conditions, we calculate the c_b range to be 10^{-3} to 10^{-2}. Mao *et al.* suggest that when c_b is well below 2, it is reasonable to neglect possible NC-NC interactions within the nanochannels and reservoir solution. Therefore, our model neglects NC-NC interactions.

To describe the NC's diffusion into the nanochannels, we start with Fick's second law that expresses the time-dependent concentration as,

$$\frac{\partial c}{\partial t} = D_c \frac{\partial^2 c}{\partial x^2}, \tag{6-2}$$

where c, t, D_c, x, and represent the NC concentration in the nanochannels, time, effective diffusion constant, and distance into the nanochannels. In order to solve Eq. 6-2, two BCs are needed to describe the physical conditions. At the boundary of the reservoir and nanochannels, x = 0, the concentration with respect to time can be considered to be constant, $c(t) = c_o$. We also need describe the starting condition of the NC's diffusion at t = 0, where the channels are free of NCs, $c(x)$ = 0. Under these BCs, the solution to Eq. 6-2 is of the form

$$c(x,t) = c_o \ \times \ erfc\left(\frac{x}{2\sqrt{D_c t}}\right). \tag{6-3}$$

The classic complimentary error function (*erfc*) result is revealed when the spatial and time dependent concentration is solved. Mathematica 7.0 is used to aid in the simulation of Eq. 6-2 with the appropriate BCs and the results are plotted in Figure 6-1. The plot illustrates that the NCs near the channel entrance as a function of time are pinned at the

initial reservoir density (c_o) (1.0E15 cm^{-3}) as the diffusion progresses, which is not observed in any of the experimental profiles. Furthermore, the model can not account for the observed experimental profile for AR 1, which has a characteristic bell-shape curve and is shown in Figure 7-8. This indicates that a more rigorous mathematical model needs to be developed.

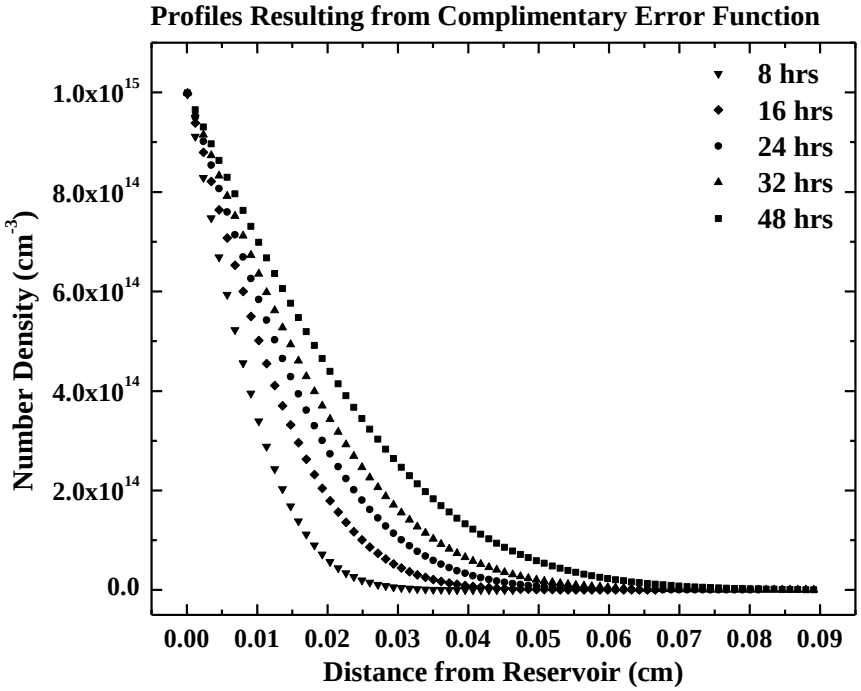

Figure 6-1. Plotted solution of *erfc* at several times when the reservoir concentration is 1.0E15 NC cm^{-3} and the diffusion coefficient is 2.0E-9 cm^2 s^{-1}.

Taking into consideration the experimental profile's characteristic rise time to a saturation density, which is discussed in Chapter 7, an empirical BC can be used to try and replicate the observed increase in inlet concentration. Specifically, the forward

diffusion model in Eq. 7-4 and the results listed in Table 7-1. Figure 6-2 shows the resulting profiles for solving Eq. 6-2 while using the empirically derived BC of,

$$\text{at } x = 0;\ c(t) = c_{sat}[1 - \exp^{(-t/\tau_{sat})}] \quad \text{, and similar initial BC} \tag{6-4}$$

$$\text{at } t = 0;\ c(x) = 0. \tag{6-5}$$

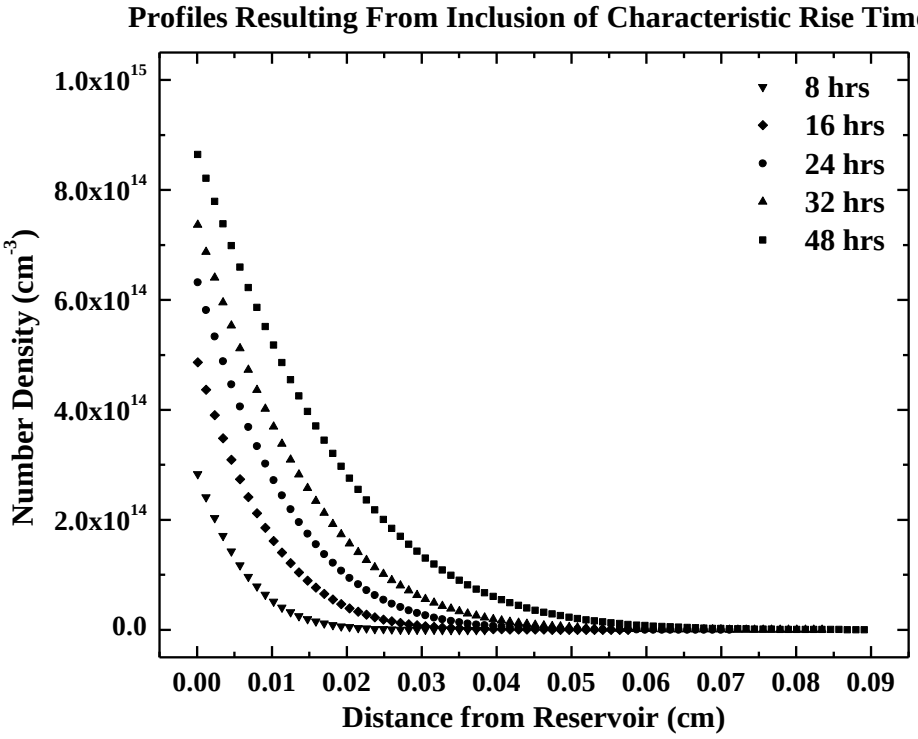

Figure 6-2. The plotted solutions of Eq. 6-2 at several times using a BC (Eq. 6-4) that simulates a characteristic rise time in the interface's concentration, and eventually equilibrates to the reservoir concentration of 1.0E15 NC cm^{-3}. The diffusion coefficient is 2.0E-9 $cm^2\ s^{-1}$ and τ_{sat} is 24 hrs.

The results shown in Figure 6-2 still show that the channel's eventual equilibrium concentration will be equivalent to the initial reservoir concentration. The resulting

profiles suggest that inclusion of a characteristic rise time as a BC could mimic the experimentally observed increase in NC concentration as a function of time. However, as it will be shown in the Results and Discussion chapter, the experimentally observed NC's saturation concentration exceeds the initial reservoir concentration due to the wall adsorption process. This suggests that the transport model needs to incorporate the adsorption concentration as a BC, the typical heterogeneous adsorption BC, to produce a more suitable fit for the experimental data, which would be expected.

As a side note, traditionally the BC for diffusion of species through membranes or microchannels from a reservoir makes use of a mass transfer resistance at the entrance. The diffusional mass transfer hindrance at the pore or channel entrance, $x = 0$, takes the form of,

$$-D_c \frac{\partial c}{\partial x} = k_c (K_p c_o - c), \tag{6-6}$$

where k_c, K_p, and c_o represent mass transfer coefficient, partition coefficient, and reservoir concentration, respectively. This BC suggests that the NC concentration in the reservoir near the nanochannel inlet becomes depleted over time, due to NCs diffusing into the nanochannels. If k_c at the channel entrance can be approximated by the ratio of the NC's diffusion constant to the thickness of this depletion layer, one can immediately deduce that k_c would vary as a function of time. However, this depletion in concentration in the reservoir near the nanochannel inlet is not easy to measure and verify experimentally within our system. This is mainly due to the reservoir's large volume of fluorescent NCs that exceed the detector's measurable intensity range; essentially our detector becomes flooded with photons in the reservoir region. Therefore, we have applied an empirical BC that accurately tracks the observed concentration near the inlet

within the nanochannels as a function of time. Essentially, this BC includes the NC's entrance process, outlined in Eq. 6-6, and adsorption concentration as a function of time.

To establish the empirical boundary condition at x = 0, we track the NC concentration near the channel inlet (x = 10.5 μm) as a function of time. While this position is not exactly x = 0, we have chosen this distance for consistency and to avoid any possible misreading of fluorescence intensity that may result from the uneven round edge of the reservoir defined in the Pyrex cover slip, which outlines the reservoir-nanochannel boundary. We can appropriately modify our BC in Eq. 6-4 by fitting the inlet concentration with a characteristic rise time (τ) and saturation concentration (c_{sat}),

$$c(t) = c_{sat}[1 - \exp^{(-t/\tau)}]. \tag{6-7}$$

Evaluation of Eq. 6-2 with the defined BC at x = 0, in Eq. 6-7, results in the profiles shown in Figure 6-3. The resulting diffusion profiles are similar to the higher AR NC's experimental profiles, suggesting that the empirical BC has merit as a general account for the influence of entrance phenomenon, diffusion, and adsorption into and within the nanochannels. However, the model still lacks a proper account for AR = 1 profile's shape. However, we also want a formal account of the adsorption process, utilizing common descriptive variables like adsorption/desorption rate constants and the equilibrium coefficient. Thus, a more representative mathematical construct needs to be investigated for our system.

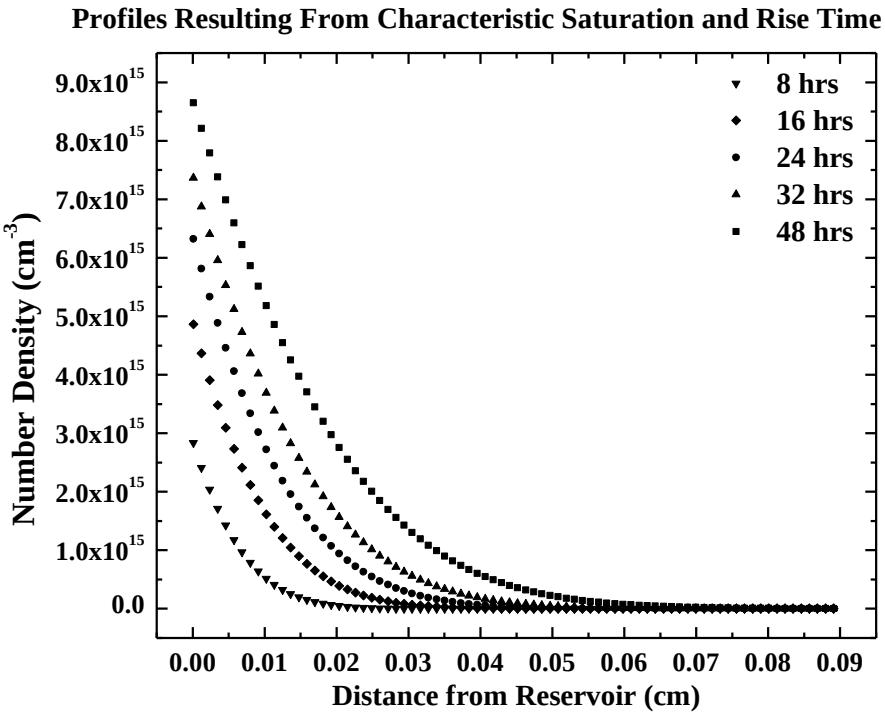

Figure 6-3. Plotted solutions of Eq. 6-2 at several times using a BC that simulates a characteristic rise in concentration as a function of time (Eq. 6-7). The modeling parameters are: c_o = 1.0E15 NC cm^{-3}, diffusion coefficient is 2.0E-9 cm^2 s^{-1}, with the modeled BC values of c_{sat} = 1.0E16 NC cm^{-3} and a τ of 24 hrs.

6.3 Single Site Adsorption Model

We have modeled the observed time-dependent NC diffusion into nanochannels using the following transport equation,

$$\frac{\partial c}{\partial t} = D_c \frac{\partial^2 c}{\partial x^2} + R_b \,, \tag{6-8}$$

where c, t, D_c, x, and R_b represent the NC concentration in the nanochannels, time, effective diffusion constant, distance from the channel inlet, and NC wall adsorption rate, respectively. The surface adsorption term, R_b, appears as a homogeneous term in Eq. (6-

8), rather than as a heterogeneous boundary condition. This approximation is allowable for the following reason. The NC transport in the nanochannels has a very small Peclet number (*Pe*), which is a unitless number that relates the convective and diffusive flow to one another. In our case, the *Pe* is equal to zero due to the complete absence of convection. Even when we consider electroosmotic flow in aqueous solutions, we typically observe a flow velocity on the order of 10 $\mu m\ s^{-1}$ or less, and the *Pe* in this case is on the order of 10^{-4} to 10^{-5}. At such a low *Pe*, the NCs' random motion can sample the nanochannels' cross-sectional plane much faster than longitudinally along the channels [56]. With the above approximation for R_b, we express the NCs adsorbed to channel walls in a bound state as *B*:

$$C + S \rightleftharpoons B \tag{6-9}$$

where *C* and *S* represent the freely diffusive NCs within the channels and surface adsorption sites, respectively. The solution concentration of NCs in the nanochannels, surface site density available for adsorption, and NC surface concentration in the bound state are denoted by *c*, *s*, and *b*. The surface site balance is given by

$$s_{max} = s + b\ , \tag{6-10}$$

where s_{max} denotes the maximum surface site density available for wall adsorption. Due to the physical differences for each AR considered in our experiments, s_{max} will have a different value for each AR. For example, spherical NCs with AR = 1 can reach a maximum surface density in a hexagonal close packed arrangement, while ARs > 1 are considered to have a head-toe and side-by-side arrangement. The adsorption rate (R_b) can be expressed by

$$-R_b = k_{des}\left(K_b\, s\, c - b\right) \quad \text{and} \tag{6-11}$$

$$\frac{\partial b}{\partial t} = -R_b \,, \tag{6-12}$$

where k_{des} (cm^{-1} sec^{-1}) and K_b (cm^3 NC^{-1}) denote the rate constant for the NCs desorbing from the walls and equilibrium constant for the process described in Eq. (6-9). The equilibrium constant is therefore a ratio of the adsorption rate constant (k_{ads}) to k_{des}, where the unit of k_{ads} is cm^3 NC^{-1} sec^{-1}. In order to solve Eq. 6-8, two BCs are needed. To be consistent with the observed increasing inlet concentration as time progresses, we have fitted the experimental rise with a characteristic c_{sat} and τ value for each AR. We believe this fitting, in a general sense, includes the entrance effects and the increasing concentration that is available due to the reversible adsorption phenomenon. The first boundary condition is

$$\text{BC 1: At } x = 0;\ \frac{\partial c}{\partial t} = c_{sat}[1 - \exp^{(-t/\tau)}] \quad , \tag{6-13}$$

where c_{sat} and τ represent the characteristic saturation concentration and time to saturation, respectively. The second boundary condition is

$$\text{BC 2: As } x \to \infty,\ c \to 0. \tag{6-14}$$

In order to show the difference between this model (Eq. 6-8 thru Eq. 6-14) and the previous models, we have simulated two cases where the equilibrium constant (K_b) is considered to favor strong adsorption, shown in Figure 6-4, and a weak adsorption, shown in Figure 6-5. Comparison of the two cases would suggest that the K_b value is an important variable in fitting the model to the NC's experimental profile. Furthermore, the simulated modeling appears to be capable of fitting all of the AR profiles, which suggests that the mathematical concepts are adequate enough to describe the experimentally observed physical features. We used Wolfram Mathematica 7.0.0 to

evaluate our transport model and extract numerical values for the diffusion coefficient, equilibrium constant, and the adsorption/desorption rate coefficients. The fitting results will be discussed in the 'Results and Discussion' section.

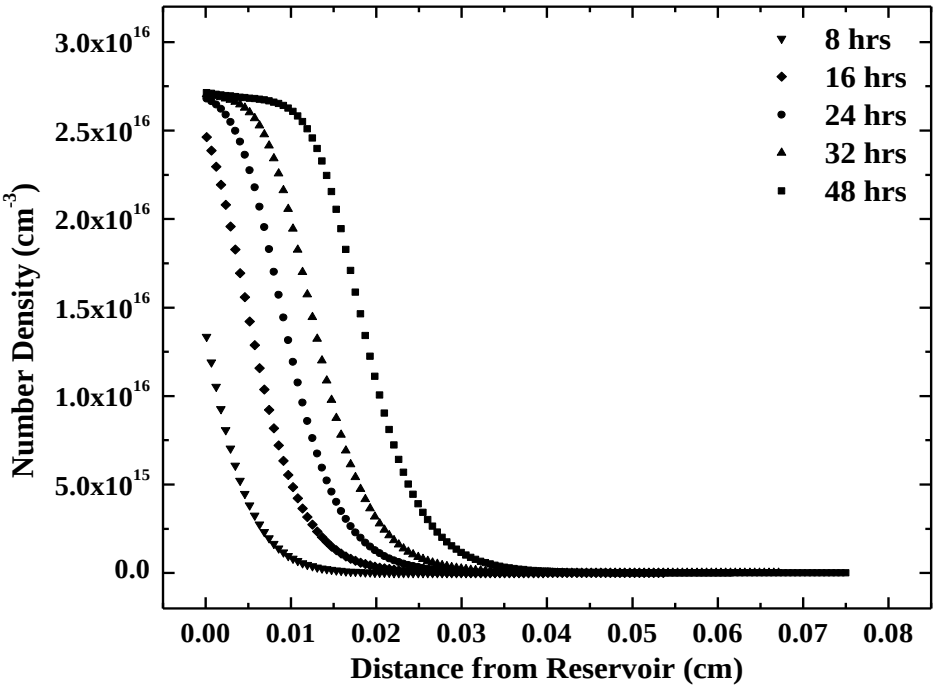

Figure 6-4. Diffusion profiles as a function of time for the case of strong wall adsorption, where K_b is 5.0 $cm^3\ s^{-1}$. The other parameters are: c_{sat} = 4.0E16 cm^{-3}, τ = 24 hrs, D_c = 2.0E-9 $cm^2\ s^{-1}$, and k_{des} = 8.0E-7 s^{-1}.

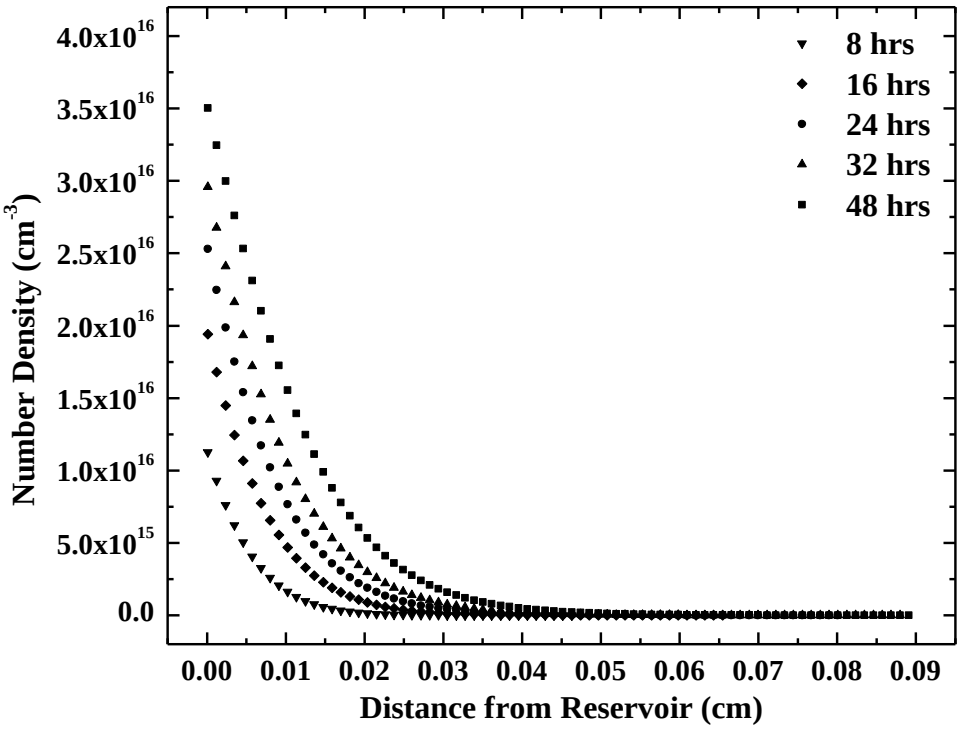

Figure 6-5. Diffusion profiles as a function of time for the case of weak wall adsorption, where K_b is 1.0 cm^3 s^{-1}. The other parameters are: c_{sat} = 4.0E16 cm^{-3}, τ = 24 hrs, D_c = 2.0E-9 cm^2 s^{-1}, and k_{des} = 8.0E-7 s^{-1}.

6.4 Two-Site Adsorption Model

We properly model the observed time-dependent NC diffusion into nanochannels, as will be discussed in Chapter 7, by using the following transport equation,

$$\frac{\partial c}{\partial t} = D_c \frac{\partial^2 c}{\partial x^2} + R_{b,str} + R_{b,wk} \quad , \tag{6-15}$$

where c, t, D_c, x, $R_{b,str}$, and $R_{b,wk}$ represent the NC number concentration in the nanochannels, time, effective diffusion constant, distance from the channel inlet,

adsorption rate of NCs strongly binding to the channel walls, and adsorption rate of NCs weakly binding to the channel walls, respectively.

The surface adsorption terms, $R_{b,\mathrm{str}}$ and $R_{b,wk}$, appear as homogeneous reaction terms in Eqn. (6-15), rather than as a boundary condition. This approximation follows the similar logic as described in the single site model, and is allowable for the following reason. The NC transport in the nanochannels has a very small Peclet number (*Pe*); *Pe* is equal to zero due to the complete absence of convection in this case. Even with an electroosmotic flow in aqueous solutions, we typically observe a flow velocity on the order of 10 μm s^{-1} or less, and the *Pe* in this case is on the order of 10^{-4} to 10^{-5}. At such a low *Pe*, the NCs' random motion can sample the nanochannels' cross-sectional plane much faster than longitudinally along the channels [56]. With the above approximation for $R_{b,\mathrm{str}}$ and $R_{b,wk}$, we express the NCs adsorbed to channel walls in a bound state as B_{str} and B_{wk}:

$$C + S \underset{k_{d,str}}{\overset{k_a}{\rightleftharpoons}} B_{str} \tag{6-16}$$

$$C + S \underset{k_{d,wk}}{\overset{k_a}{\rightleftharpoons}} B_{wk} \tag{6-17}$$

where C, S, B_{str}, and B_{wk} represent freely diffusive NCs within the channels, surface adsorption sites, NCs strongly bound to the channel walls, and NCs weakly bound to the channel walls, respectively. Therefore, k_a is the adsorption rate constant that is assumed to be identical for both strongly and weakly bound states, while $k_{d,str}$ and $k_{d,wk}$ are the desorption rate constant of strongly bound NCs and weakly bound NCs, respectively. The two adsorption states can then be described by two corresponding equilibrium constants:

$$K_{b,str} = \frac{k_a}{k_{d,str}} \quad \text{, and} \tag{6-18}$$

$$K_{b,wk} = \frac{k_a}{k_{d,wk}} \quad . \tag{6-19}$$

For the rate expressions, the solution concentration of NCs in the nanochannels, surface site density available for adsorption, and NC surface concentration in the two bound states are denoted by c, s, b_{str}, and b_{wk}. The surface site balance is then given by

$$s_{\max} = s + b_{str} + b_{wk} \ , \tag{6-20}$$

where s_{max} denotes the maximum surface site density available for wall adsorption. Due to the physical differences for each AR considered in our experiments, s_{max} will have a different value for each AR. For example, spherical NCs with AR = 1 can reach a maximum surface density in a hexagonal close packed arrangement, while ARs > 1 are considered to have a head-toe and side-by-side arrangement. We denote the maximum surface site density based on the close-packing arrangements with s_{cp}. However, for random sequential adsorption of NCs where adsorption is limited by the geometric obstruction of the previously adsorbed NCs [110], the close-packing limit must be reduced to an appropriate level:

$$s_{\max} = \varepsilon s_{cp} \quad , \tag{6-21}$$

where ε is the correction factor (< 1) accounting for the random sequential adsorption. Talbot *et al.* provided a review of analysis on random sequential adsorption of spherocylinders, using statistical mechanics and Monte Carlo simulations, and we use the reported values of ε ranging from 0.547 (AR = 1) to 0.525 (AR = 6) [110]. The adsorption rates ($R_{b,str}$ and $R_{b,wk}$) can then be expressed by

$$-R_{b,str} = k_{d,str}\left(K_{b,str}\, s\, c - b_{str}\right) \ , \tag{6-22}$$

$$-R_{b,wk} = k_{d,wk}\left(K_{b,wk}\, s\, c - b_{wk}\right) \ , \tag{6-23}$$

$$\frac{\partial b_{str}}{\partial t} = -R_{b,str} \qquad \text{, and} \tag{6-24}$$

$$\frac{\partial b_{wk}}{\partial t} = -R_{b,wk} \qquad . \tag{6-25}$$

In order to solve Eq. (6-15), two boundary conditions are needed. To be consistent with the observed increasing inlet concentration at $x = 0$ as time progresses, we have fit the experimentally measured forward diffusion concentration with an empirical model containing a saturation concentration (c_{sat}) and a characteristic rise time (τ_{sat}) for each AR. As we will discuss in a later section, c_{sat} corresponds to a combined concentration of freely diffusive NCs at equilibrium (c_e) at the channel entrance and NCs adsorbed to the channel walls at equilibrium at the channel entrance (c_{surf}). We therefore model the entrance BC by considering the characteristic rise time, where the first boundary condition for c at the entrance is given by

$$\text{At } x = 0,\ c = c_e[1 - \exp^{(-t/\tau_{sat})}]. \tag{6-26}$$

The second boundary condition is

$$\text{As } x \rightarrow \infty,\ c \rightarrow 0. \tag{6-27}$$

We use $c(x, t = 0) = 0$ as the initial condition, where the channels are empty. These BCs allow us to model the two-site transport system with Eqs. 6-15 through 6-27. The results will be discussed in the Results and Discussion section (Chapter 7).

6.5 Conclusions for the Diffusion Modeling

Throughout this section, we have developed several modeling concepts that pertain to the boundary conditions and have proposed modifications to Fick's second law to better account for the adsorption process within nanochannels. The simulations of the final model (Eq. 6-15 thru 6-27) would suggest that an adequate mathematical description of the observed forward diffusion profiles is accounted for by the model's variables. The variables that make up the final model include the diffusion coefficient, two equilibrium coefficients, and the adsorption/desorption rate constants. The empirical boundary condition at the reservoir entrance, Eq. 6-26, should allow the profiles to be adequately fit without having the knowledge of the entrance effects. We will report the boundary condition fitting values obtained from the forward diffusion experiments, the ramifications observed from the reverse diffusion experiments, and the averaged fitting values for both the single site and two-site model in the following Results and Discussion section.

CHAPTER 7 RESULTS AND DISCUSSION

7.1 Introduction

Our diffusion experiments include the use of several synthesized batches of CdSe spheres and rods, the latter of which differ primarily by their elongation and therefore provide several aspect ratios (ARs = length/width). We experimentally monitor the concentration profile of these NCs as they diffuse into 100-nm-wide, 400-nm-deep rectangular nanochannels. The NCs are suspended in toluene and the nanochannels are filled with toluene prior to the diffusion experiments. The toluene solution is considered to be an aprotic solution, since there are no electrolytes or significant amount of charged surfactants added to the toluene solution. This allows the experimental focus to be on the diffusion properties of the NCs, as a function of their AR, into the nanochannel geometry without electrostatic interactions playing a dominant role. The fluorescent intensity of the CdSe NCs is used to both quantify the NC concentration and track the NC's movement as a function of time and distance from the channel inlet.

Once the NCs have sufficiently progressed into the nanochannels, a reverse diffusion experiment is carried out. The reverse diffusion experiment allows the NCs that have previously diffused into the nanochannels to out-diffuse into a reservoir that is filled with neat toluene. Again the tracking of the concentration as a function of time and distance is captured. The results allow for an estimation of the equilibrium constants that are in turn used in the transport modeling of the system.

The following sections provide examples of the experimental data collected, and highlight the pertinent results from both the forward diffusion and reverse diffusion experiments. Based on the analysis of these experiments, the mechanisms of attachment

and desorption process are discussed in terms of the physical NC interaction. We in turn incorporate a descriptive two-state desorption process in the form of two equilibrium constants, which are used in a two-site transport model. We first evaluate a single site transport model, followed by the two-site transport model, and discuss each model's fitted diffusion coefficient, equilibrium coefficients, adsorption and desorption constants, which are collectively compared as a function of the aspect ratio. Finally, a summary of the work with the relevant conclusions, trends, and numbers of interest will be discussed with respect to the scientific significance of the work.

7.2 Forward Diffusion: Inlet Concentration Data

The fluorescent intensity of CdSe NCs is used to quantify the NC concentration within the nanochannels as a function of time and distance from the channel inlet. The general observation for all ARs is that the NC concentration within the nanochannels increases over time and eventually saturates. As a possible mechanism for the gradual increase in the inlet concentration as a function of time, one can introduce a mass transfer hindrance at the channel inlet as a boundary condition at $x = 0$:

$$-D_c \left.\frac{\partial c}{\partial x}\right|_{x=0} = k_c(K_p c_{bulk} - c), \tag{7-1}$$

where k_c, K_p, and c_{bulk} represent the mass transfer coefficient, partition coefficient, and reservoir concentration of NCs, respectively. In previous microfluidic studies, it has been shown that it is common to experimentally observe and model a concentration gradient leading up to a solid interface or pore opening. A depletion layer forms as NCs diffuse into the channels, essentially leading to a region of mass transfer resistance or more appropriately a diffusion-limited region. If k_c at the channel entrance can be

approximated by the ratio of the NC's diffusion coefficient to the thickness of this depletion layer, one can deduce that k_c would vary as a function of time. However, the concentration depletion and its time dependence in the reservoir near the nanochannel inlet are not easy to measure and verify experimentally in our setup. The experiments are limited by the ability to adequately account for the concentration in the reservoir at a specific height without interference from the above NC solution, and by the significantly different intensity observed for the reservoir and within the nanochannel. Secondly, the magnitude of the concentration increase at the inlet is much greater than that of the reservoir concentration, indicating that the gradual increase is largely due to wall adsorption, rather than a mass transfer hindrance.

Although we cannot directly observe the mass transfer hindrance in our experiments, and we believe the system has strong wall adsorption, we have developed a formal thermodynamic evaluation of the partition coefficient to account for the freely diffusive NC's within the nanochannels. The partition coefficient is developed from statistical mechanics for a confined spherocylinders at the low density limit (NC's are considered dilute) and is further evaluated at thermodynamic equilibrium, see formalism in Appendix A (Eq. A-16). The derived equation is

$$K_p = \frac{\bar{\rho}}{\rho_{bulk}} = \frac{H - \frac{L}{2} - W}{H} \quad , \tag{7-2}$$

where $\bar{\rho}$, ρ_{bulk}, H, L, W is the average number density in the channel, initial bulk number density in the reservoir, limiting dimension of the channel, length of the NC, and width of the NC, respectively. Equation 7-2 relates the partitioning of the NC's average density within the pore to the original solution density at thermodynamic equilibrium. In

evaluating the right side of Eq. 7-2, our NC's increase in AR results only in a small decrease in the partition coefficient, as shown in Figure 7-1.

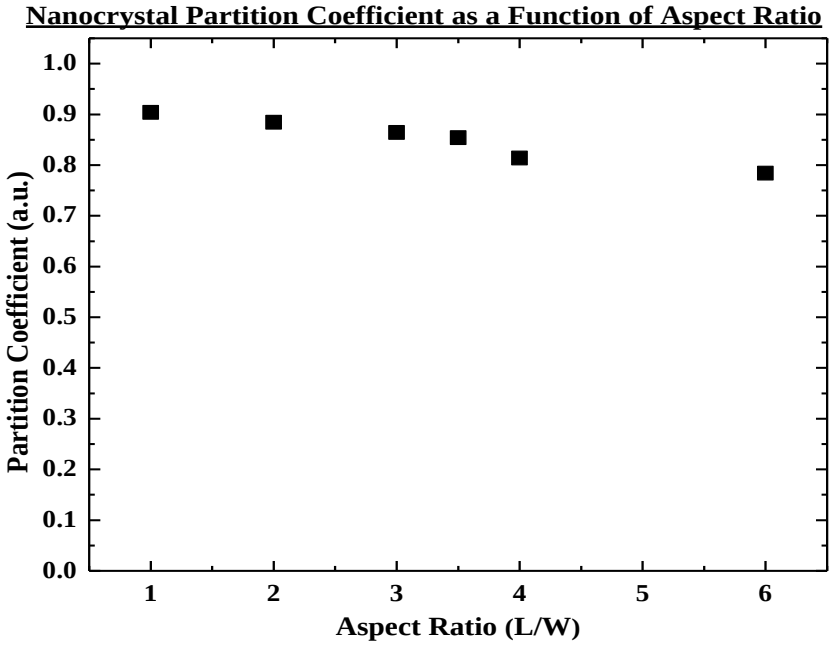

Figure 7-1. The calculated partition coefficient from Eq. 7-2 as a function of AR for the nanocrystals evaluated in this work.

Since we believe that the entrance's increasing concentration and eventual saturation within our nanochannels are mainly due to the channel walls adsorbing NCs, we should explain the mechanism that limits the wall's adsorption. The mechanism, in which the NC concentration is eventually limited, is explained by considering that the already adsorbed NCs physically block additional NCs from adsorbing onto the channel's surface; the NC-NC interaction is not attractive. However, if the NC-NC interaction is attractive, then a multilayered adsorption would be expected. We further discuss the mechanisms of adsorption and desorption in a later section. In order to model the concentration increase, we probe the inlet concentration as a function of time by

averaging the area near the entrance. Shown in Figure 7-2 is an example of the inlet concentration probe area (diameter 50 μm) used to average the nanochannel's areal intensity from the LS-CFM image. The average intensity is converted to a number density that is plotted as function of time in Figure 7-3 for several AR NCs.

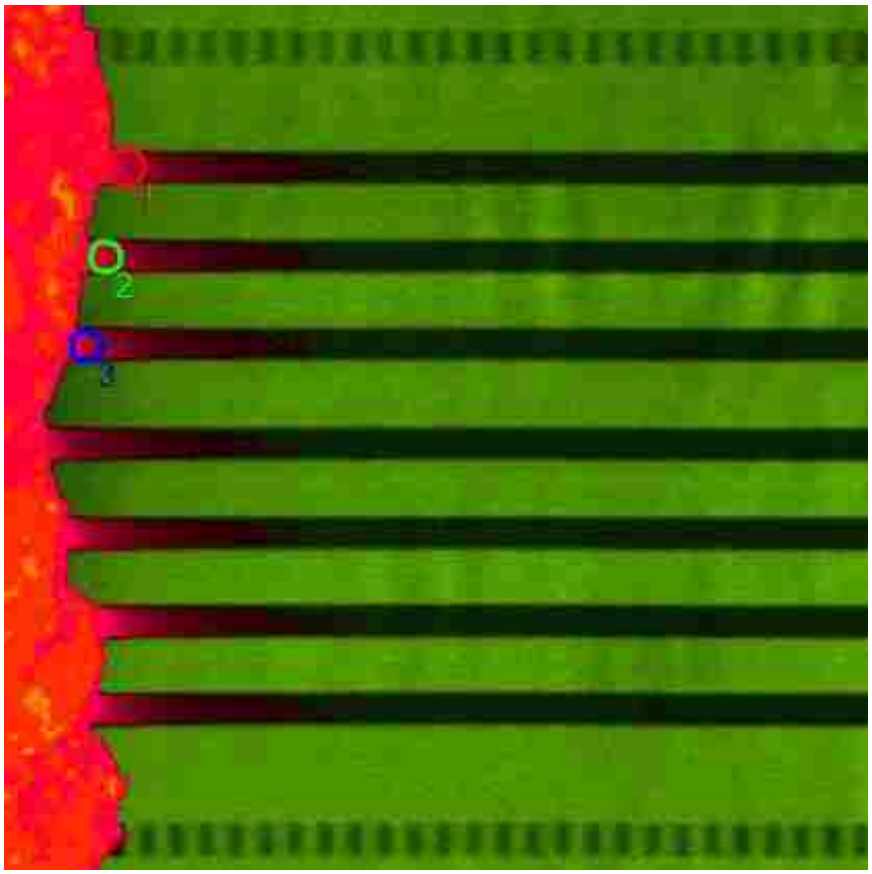

Figure 7-2. A typical LS-CFM image highlighting three example regions that would be included in the averaging of all seven channels (the other 4 probe circles are removed for clarity).

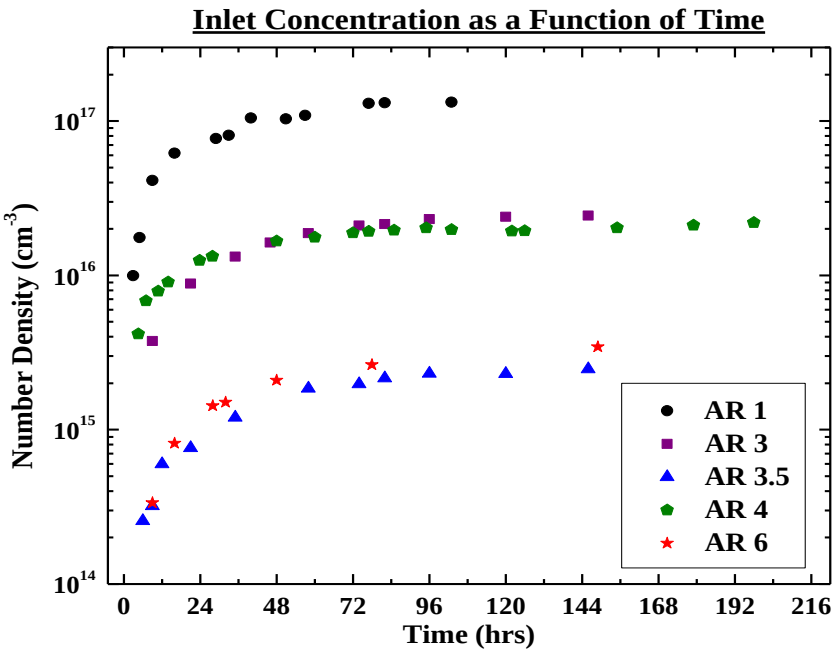

Figure 7-3. The averaged inlet concentration as a function of time for several AR NCs.

It should be noted that the NC reservoir concentration (i.e., bulk NC solution in the reservoir outside of the channels) remains virtually constant, since only a small amount of NCs diffuse into the nanochannels as compared to the bulk solution within the container. Furthermore, evaporation of the NC solution is kept minimal as the experiments are conducted by using a screw-top container that is closed at all times, except when pulling the nanochannel chip out for imaging. The nanochannel's increasing concentration (c_t) above the reservoir concentration is shown in Figure 7-4, which shows the data normalized by the individual NC's reservoir concentration (c_{bulk}).

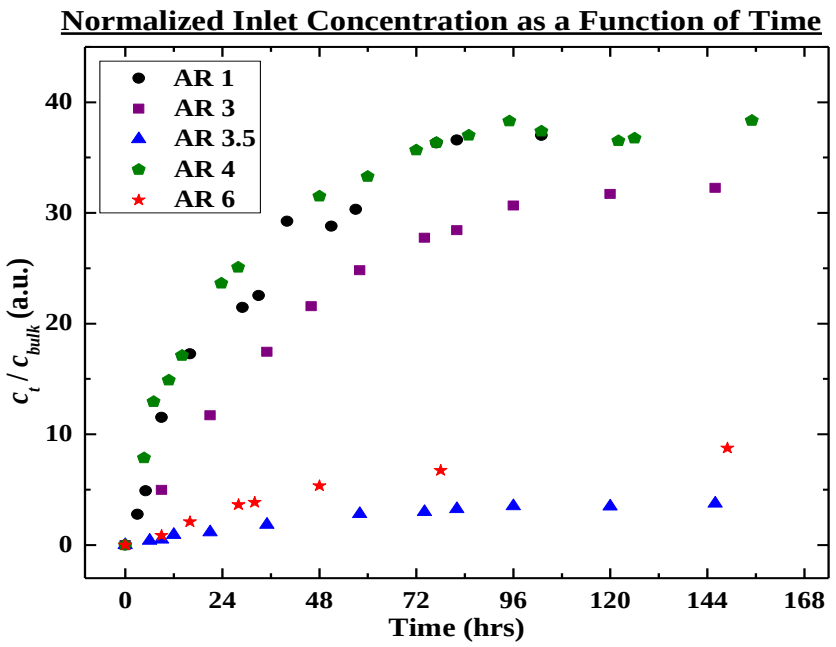

Figure 7-4. Normalized inlet concentration as a function of time, which shows the effective increase in concentration beyond the initial reservoir concentration.

Upon examination of Figure 7-4, it becomes apparent that the diffusion of dilute NCs, in all cases, is not indicative of simple diffusion, but rather it rises over time and saturates to an apparent level 4 to 40 times higher than the reservoir's bulk solution. This observation led us to conclude that a mass transfer resistance and possible partitioning at the channel's inlet, both of which under simple diffusion conditions keep the concentration below the reservoir concentration, could not reasonably account for the substantial increase in the observed concentration as time progressed. Instead, we consider that a NC-wall interaction in the form of a reversible adsorption must account for the apparent NC concentration that is several times higher than the bulk reservoir concentration.

The basic nature of this adsorption phenomenon can be examined by calculating an estimate of the adsorption energy, which will help determine the type of NC-silica interaction, i.e. weak physical adsorption like van der Waals or a strong chemical adsorption like chemical bonding. If we consider a macroscopic system that contains a uniform surface in which one dilute component adsorbs to the surface and is limited to a monolayer coverage, an equation for the free energy of adsorption can be estimated by replacing the activities with effective concentrations [111-113],

$$\Delta G = -RT\, ln \frac{c_{ads}}{c_{bulk}}, \tag{7-3}$$

where ΔG is the free energy of adsorption (J/mol), R is the gas constant (J/mol K), T is the temperature (K), c_{ads} is the concentration adsorbed on the surface, and c_{bulk} is the bulk concentration. For estimating our system, we estimate c_{ads} as the saturation concentration (c_{sat}) reduced by the freely diffusive equilibrium concentration (c_e), i.e. $c_{ads} = c_{sat} - c_e$; where $c_e = K_p \times c_{bulk}$. A more formal definition for c_{sat} will be discussed in the following paragraphs. The approximate ΔG calculated for the various ARs ranged from -5.5 to -9.6 kJ/mol. The approximate values would suggest that the adsorption process is indeed van der Waals in nature and allows us to consider the system as having reversible adsorption. This isn't unexpected as the NC's terminating chemical motif (ligand) is a hydrocarbon chain that is considered to be chemically inert, and would provide no reasonable chemical bonding with the silica surface. However, hydrogen bonding is typically on the order of 5 to 30 kJ/mol, which could also be partially responsible for a weak interaction between the particle and the surface. Recently, the interaction energy between a bulk solution containing aqueous 25 nm CdSe/ZnS core-shell quantum dots conjugated with streptavidin, and a silica surface was calculated to be -24.66 kJ/mol (25

^{o}C in a 300 mM phosphate-buffered saline solution at a pH of 7.4, ionic strength of 10^{-3}) [114]. The authors suggest that the adsorption process was primarily due to hydrophilic interactions between the QDs and silica surface. Likewise, Schmitt *et al.* calculated the free energies of adsorption for the anisotropic protein fibrinogen (6 nm x 45 nm) using a variety of complex polymer surfaces with varying charge densities. The average free energy of adsorption was calculated to be ~ -28 kJ/mol at low protein concentrations (23 ^{o}C in a 50 mM Tris buffer at a pH of 7.35) [115]. The non-specific and relatively weak bonding of the protein to the various polymer surfaces was considered a general van der Waals attraction.

Fitting of the observed inlet concentration as a function of time is reasonably well defined by the single exponential expression,

$$c(t) = c_{sat}[1 - \exp^{(-t/\tau_{sat})}], \tag{7-4}$$

where, c_{sat} represents the saturation concentration and τ_{sat} the characteristic rise time. An example of the curve fitting is shown in Figure 7-5 for an AR 3. The equation assumes that a monolayer formation of NCs can exist on the surface and that the NCs are adsorbed to the surface at a uniform rate. By averaging multiple experimental runs for each AR, the characteristic inlet concentration parameters are established and listed in Table 7-1.

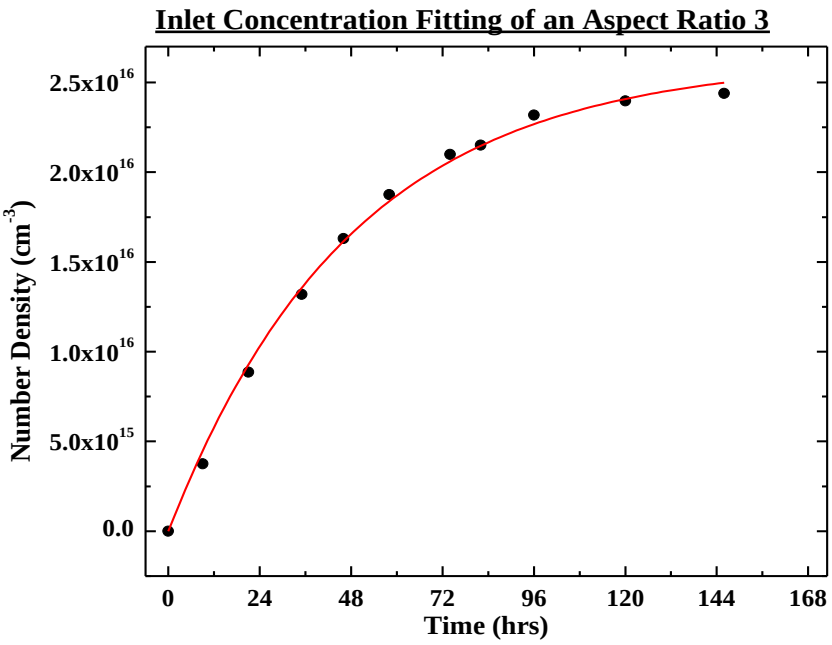

Figure 7-5. An example of the fitting curve (red line) for AR 3 data (●) by Eq. 7-4; fitting parameters are c_{sat} = 2.63 x 10^{16}, τ_{sat} = 48.17, with an adjusted R^2 = 0.997.

Table 7-1. Averaged Forward Diffusion Fitting Parameters From Eq. 7-4.

AR	c_{sat} (x10^{16} NC cm^{-3})	τ_{sat} (hr)
1	14.18±0.22	29.00±1.15
2	1.21±0.04	41.44±6.42
3	2.61±0.06	44.13±2.99
3.5	0.26±0.01	46.13±0.74
4	1.90±0.28	34.68±4.92
6	0.38±0.01	59.51±3.66

The data in Table 7-1 represents the averaged fitting parameters from multiple runs (≥4) of data for each AR. The averaged data suggests that the increase above the reservoir's bulk solution is quite substantial for AR 1, ~40 times, and even for the longest AR 6 NCs the value is ~10 times higher. This signifies that adsorption is predominant within the aprotic nanofluidic system. However, there does appear to be some inconsistency in the data as it relates to the c_{sat} values. It could be assumed that much of the inconsistency arises from interfacial differences that may alter the concentration gradient proceeding into the nanochannel openings. Also, there maybe some unaccounted for experimental error in characterizing and measurement of the initial bulk solution concentrations. These differences could impact the total amount of NCs observed at equilibrium within the nanochannels, although these issues seem to be poor excuses. In the lapse of having a macroscopic experimental study on the impact of variation of the reservoir concentration on adsorption density, thus establishing the NCs isotherm, it is hard to draw any conclusive trend from our apparent c_{sat} values. Furthermore, the impact of the AR could reasonably alter the adsorption density and equilibrium concentration within the nanochannels. Another consideration is how the passivating ligand density changes on the various NC's surfaces, although it is expected to be fairly similar but the most noticeable difference would be between a sphere and a much longer spherocylinder. Additionally, the ligands may also change the general shape of the particle, especially for low AR NCs.

Comparison of the τ_{sat} values suggests that it takes longer to reach a stable inlet concentration as the NC AR increases. For instance, τ_{sat} for AR 6 is approximately two times that of AR 1. We attribute this trend to the decrease in diffusion coefficient with

increasing AR when considering freely diffusing NCs in an unconfined large volume. In fact, the diffusion coefficient for AR 1 in an unconfined large volume, approximated from the Stokes-Einstein equation, is three times faster than that of AR 6, which is approximated from a correlation developed by Garcia de la Torre *et al*. [116]. The resulting implication is that the wall-collision rate decreases with the NC's increasing AR. Therefore, the rate at which the NCs collide with the channel walls must be approximately three times more frequent for AR 1 than for AR 6. Pappaert *et al.* have also shown a similar trend in the analysis of average characteristic time between wall collisions for dye and single-strand DNA molecules of different molecular weight within a nanochannel [21]. Assuming that the wall adsorption rate is proportional to the wall collision rate, the observed τ_{sat} ratio of 2 for comparison of AR 6 to AR 1 is consistent with their diffusion coefficients in an unconfined large volume.

In addition to the collision rate with the channel walls, the number of NCs per unit area (i.e., areal number density) that would constitute a complete monolayer would be expected to decrease as a function of increasing AR, due to the increased occupation area for a NC laying on it's side. We approximate the observed inlet saturation concentration (c_{sat}) as a sum of adsorbed NC concentration (c_{surf}) and freely diffusing NC concentration at equilibrium (c_e); therefore, $c_{surf} = c_{sat} - c_e$. The adsorbed NC concentration (c_{surf}) is a volume-equivalent concentration if the adsorbed NCs were to be released into the free-volume within the nanochannels. The equilibrium concentration (c_e) is approximated by the partitioned concentration of NCs in the nanochannels according to our previous description; $c_e = K_p \times c_{bulk}$. We use a volumetric equivalent because we experimentally measure the total amount of NCs in the nanochannel's volume, and therefore must relate

the adsorbed species to those that are freely diffusing. For comparison, we also consider the concentration for a fully adsorbed monolayer (c_{mono}), which is a volume concentration equivalent to the maximum surface adsorption site density derived from a close packing arrangement. However, as will be discussed in the proceeding paragraphs, for random sequential adsorption (RSA) of NCs where adsorption is limited by the geometric obstruction of the previously adsorbed NCs [110], the close-packing limit must be reduced to an appropriate level. We further supply the RSA packing limit (s_{max}) that we use in our modeling of the NCs in the form of a volumetric equivalent plotted as c_{max}. Note that the NCs are modeled with surfactants that have a surface density of 1 nm^{-2} and for spheres extend 0.5 nm, while spherocylinders extend 1.2 nm off of the NC's surface. Additionally, if we adjust our definition of AR to include the surfactant length, AR 3, 4, and 6 would effectively have an AR of ~2.3, ~3, and ~4.3, respectively. However for consistency, we will keep our definition of AR to remain exclusive to the physical description of the NC's crystalline core. Therefore, Figure 7-6 compares the experimental c_{surf} against c_{mono} and c_{max}, which all show an expected monotonic decrease as AR increases.

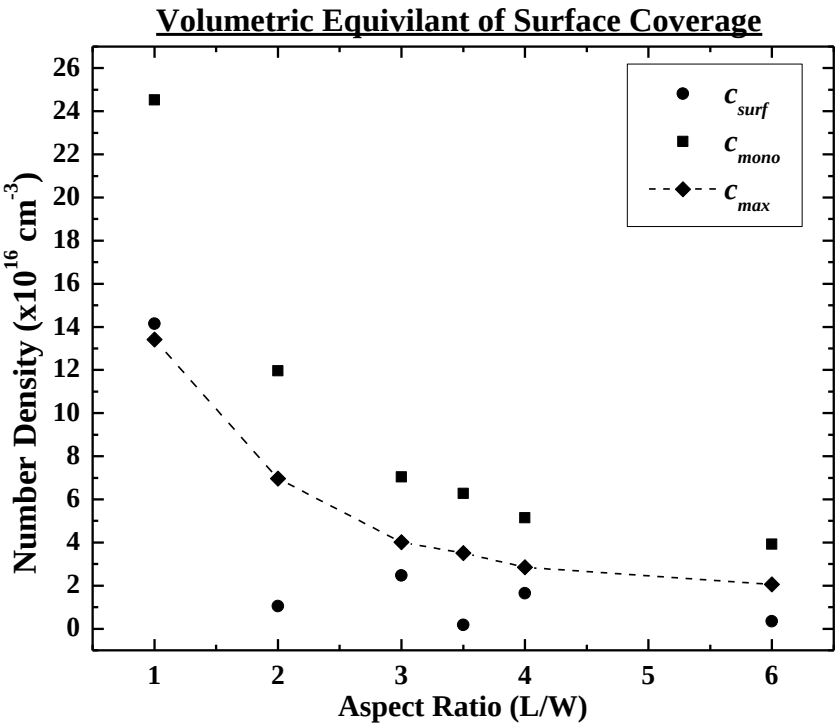

Figure 7-6. Several calculations of the equivalent volumetric surface coverage as a function of AR.

Calculating the average fraction of surface coverage (c_{surf} / c_{mono}) at time >100 hrs results in values of 57%, 33%, 36%, and 9% for ARs 1, 3, 4, and 6 respectively. However, it is important to note that c_{surf} never reaches c_{mono}, as one would expect from the RSA of NCs onto a surface, see c_{max} values in Figure 7-6. Collectively, it should be further noted that c_{surf} is below the predicted RSA values used in our modeling of the surface.

The sequential irreversible adsorption of NC's without overlap onto a surface can be computationally modeled by the RSA process via Monte Carlo simulations. The RSA process limits the surface coverage to less then a monolayer because the geometric obstruction of previously adsorbed NCs leads to surface voids forming in-between the

NCs that cannot be accessed by additional NCs [110]. The typical surface coverage from two-dimensional RSA modeling of spheres is ~55%, while spherocylinders vary depending on their AR [110], see Figure 7-7. It is important to note that our experimental surface coverage for spheres appears to agree with the RSA model. However, our results for higher AR NCs appear to fall much lower (~20-25%) then the RSA modeling of spherocylinders predicts. Interestingly, Schaaf, *et al.* have experimentally calculated the maximum surface coverage for fibrinogen to be ~40% [117], although RSA for the same AR spherocylinder predicts ~51% [110]. This is a considerable difference between a macroscopic experiment and a computational value. Furthermore, RSA has been noted to over-predict sphere-like globular proteins as well [118-120]. In general, it appears that RSA over predicts the surface coverage for spherocylinders as well, and it is suspected that the hydrodynamic interactions between particles diffusing to the surface and the surface adsorbed particles play a more substantial role in the system. Examples of the latter case would include van der Waal's forces, or electrostatic and short range repulsions. It has been commented on by several authors that these neglected interactions by the RSA model would modify the kinetics and the overall structure of the adsorbed layer [110, 121-123]. For the particular case of a 100 nm wide nanochannel, the effect of a NC standing on end off of the surface could substantially change the angle in which additional NCs can adsorb to the surface. This would be especially true for the case of AR 6, where the NC reduces the cross-sectional area of the channel substantially. Specifically, the NC has a length up to 30 nm and would be impeding by 60 nm (30 nm from each side) of the total 100 nm available.

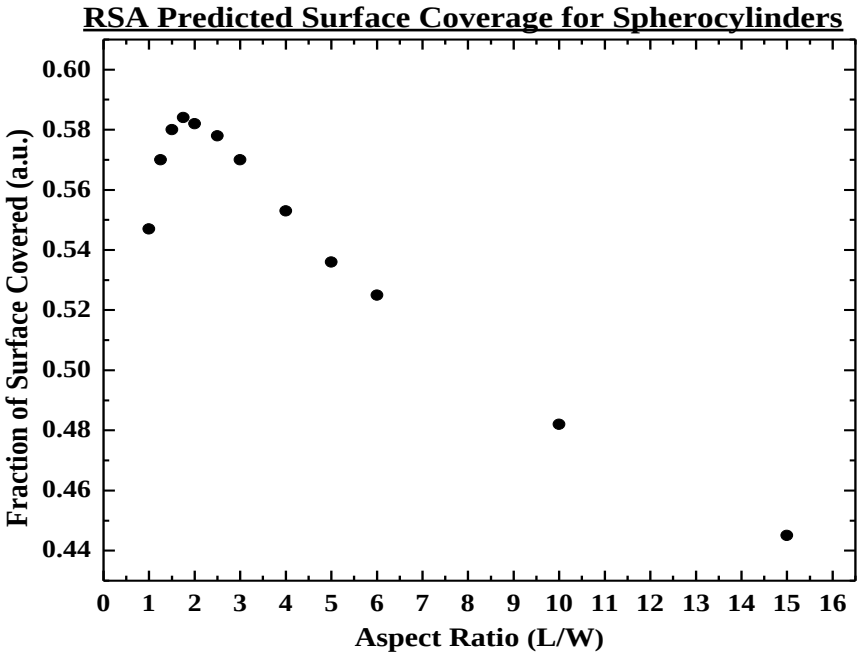

Figure 7-7. The summarized RSA modeling results as a function of AR for a spherocylinder. These results are adapted from Figure 5 in Talbot, *et al.*[110].

7.3 Forward Diffusion: Profile Data

The forward diffusion profiles for each AR are collected using nanofluidic chips described in the experimental section. For each time step, we average the fluorescence intensity from the seven 50-μm-wide strips as a function of distance from the channel entrance to produce the concentration profile, see Figures 7-8 thru 7-13. For AR 1, we find that all of our collected profiles show a characteristic bell-shaped curve. This shape is different from the common complementary error function (*erfc*) that often describes purely diffusive transport with an infinite source and a fixed concentration at the diffusion source's boundary. Similar bell-shaped diffusion profiles are often observed in affinity chromatography, where the molecules being separated strongly interact with the static medium that fills the column [124]. Karnik *et al.* also suggested a similar

concentration profile, when molecules diffusing in a nanochannel irreversibly bind to the functional groups immobilized on the channel wall [70]. The observed bell shape thus suggests that NCs may strongly interact with the channel walls and adsorb to them within the nanochannels. In contrast, the concentration profiles approach the shape of *erfc* with increasing AR. This general observation suggests that higher AR NCs interact with the channel walls less strongly than spherically shaped NCs.

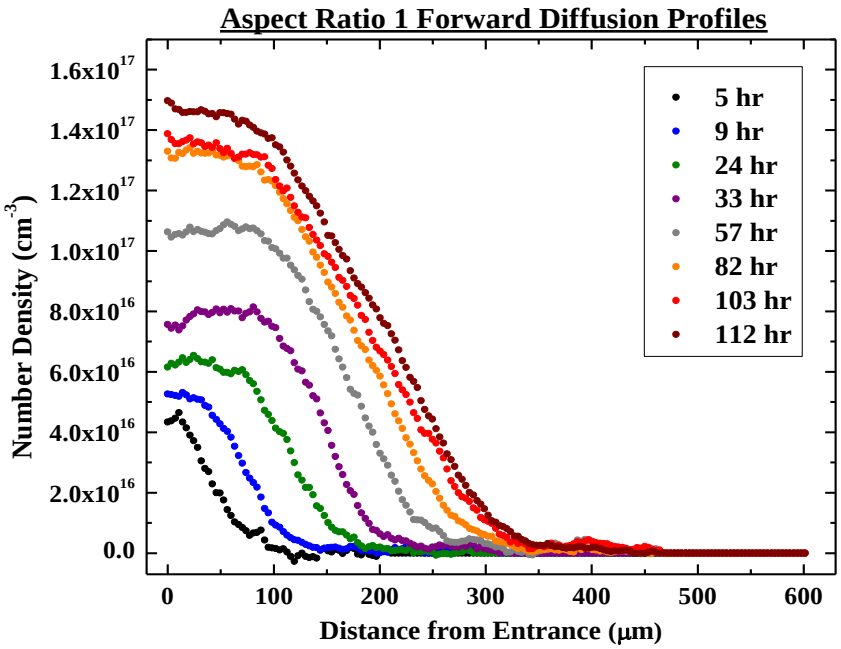

Figure 7-8. An example of forward diffusion profiles for AR 1.

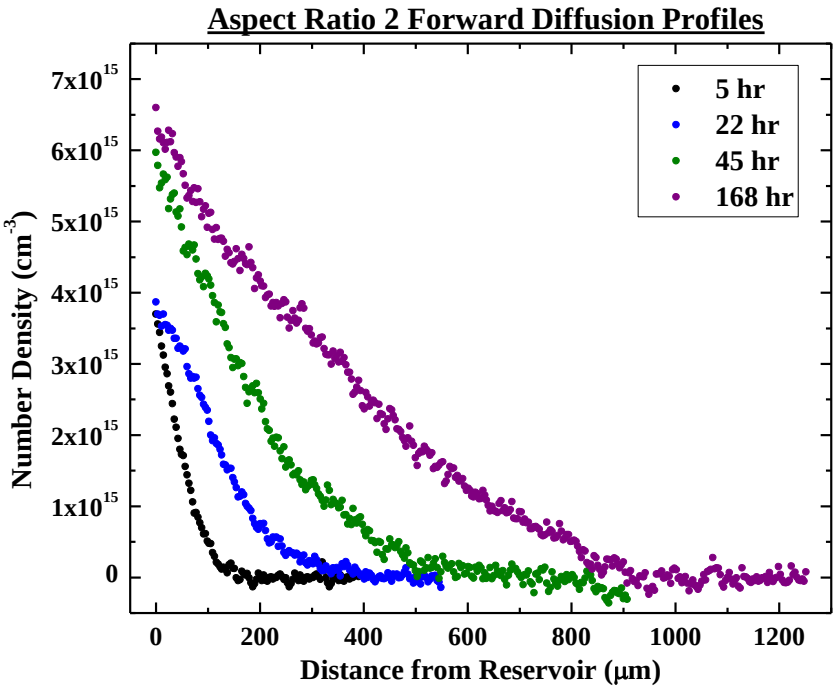

Figure 7-9. An example of forward diffusion profiles for AR 2.

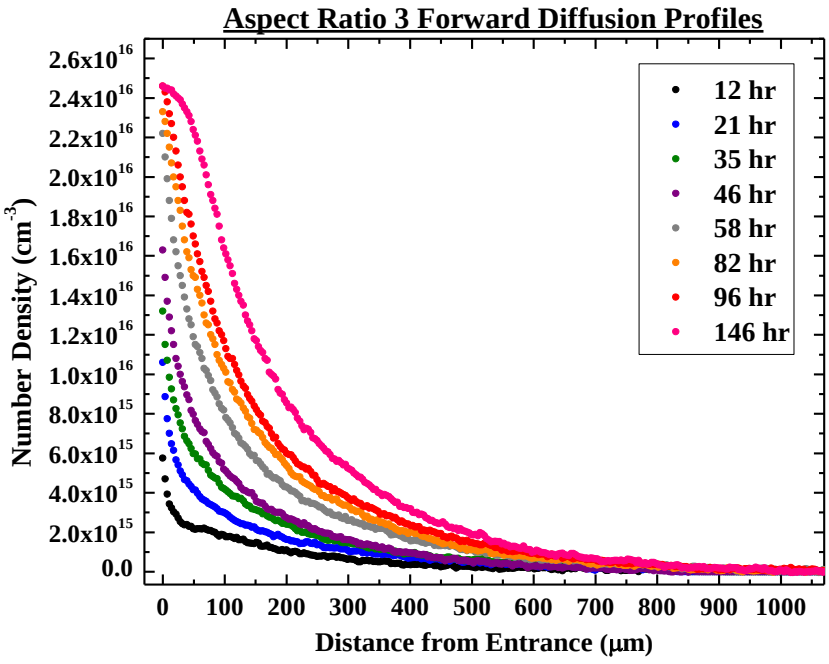

Figure 7-10. An example of forward diffusion profiles for AR 3.

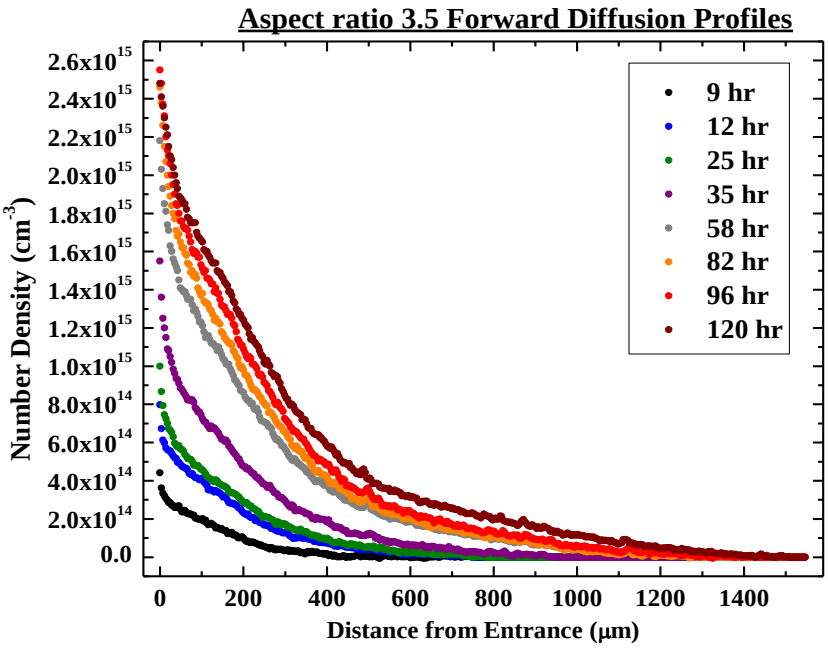

Figure 7-11. An example of forward diffusion profiles for AR 3.5.

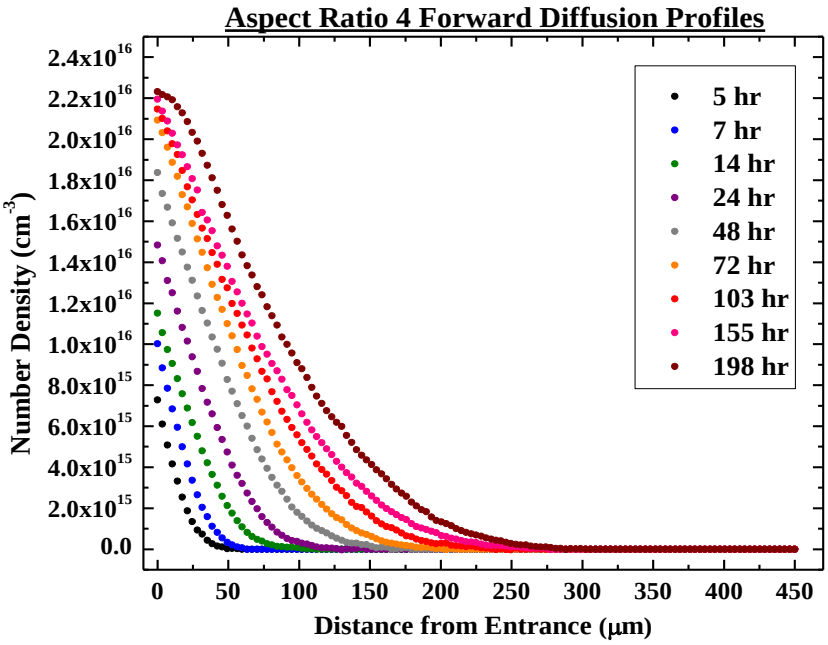

Figure 7-12. An example of forward diffusion profiles for AR 4.

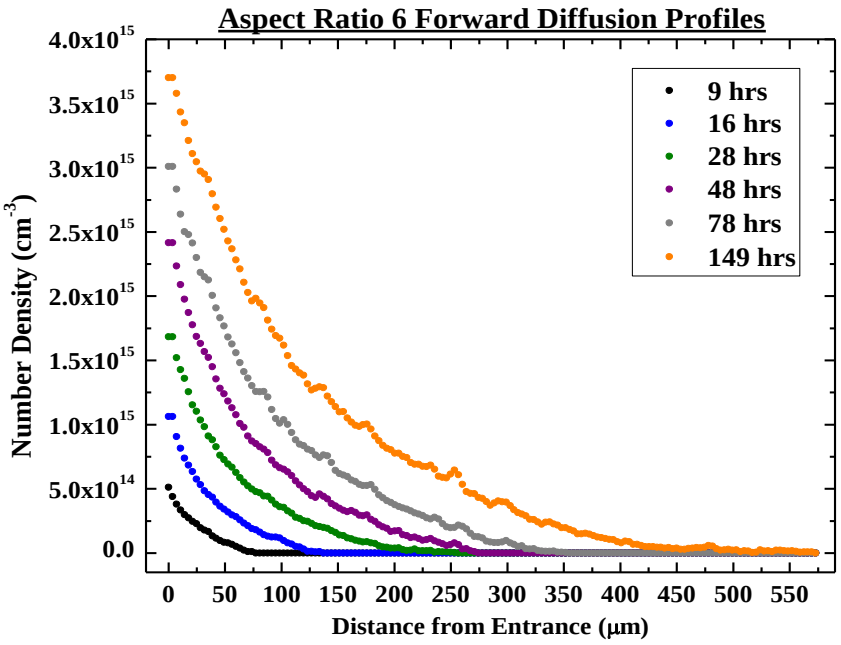

Figure 7-13. An example of forward diffusion profiles for AR 6.

7.4 Reverse Diffusion Data

The reverse diffusion experiments are conducted immediately following the forward diffusion in order to delineate the channel entrance effect and wall adsorption from free channel diffusion. The NC concentration near the exit (i.e., the entrance for forward diffusion) within the nanochannels is recorded as a function of time; see Figures 7-14 through 7-19. The observed concentration as a function of time during reverse diffusion shows two distinct time constants, and suggests that two groups of NCs exist within the nanochannels: (i) the 1st group that readily diffuses out from the channels on the order of hours and (ii) a 2nd group that slowly diffuses out from the channels on the order of days. By fitting the concentration with a double exponential, we approximate the characteristic concentrations and time constants associated with the two processes:

$$c_{surf} = c_{sat} - c_e = c_{ads,wk} \exp^{(-t/\tau_{wk})} + c_{ads,str} \exp^{(-t/\tau_{str})}, \quad (7\text{-}5)$$

where $c_{ads,wk}$, τ_{wk}, $c_{ads,str}$, and τ_{str} denote the concentration of NCs that readily diffuse out, the time constant associated with the fast out-diffusion, the concentration of NCs that slowly diffuse out, and the time constant associated with the slow out-diffusion, respectively. The values of $c_{ads,wk}$, τ_{wk}, $c_{ads,str}$, and τ_{str} averaged over 4 to 5 runs for each AR are listed Table 7-2.

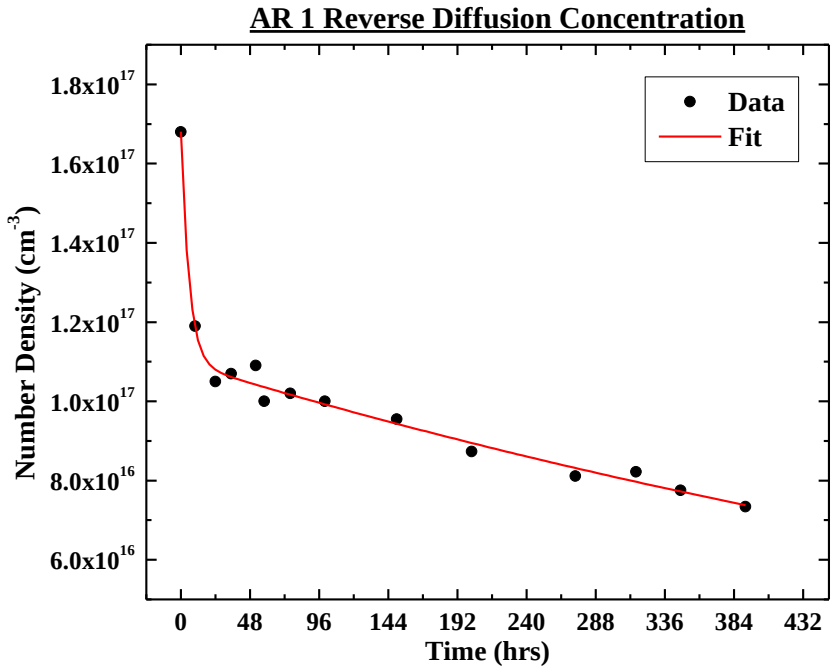

Figure 7-14. An example of the reverse diffusion concentration as a function of time for AR 1.

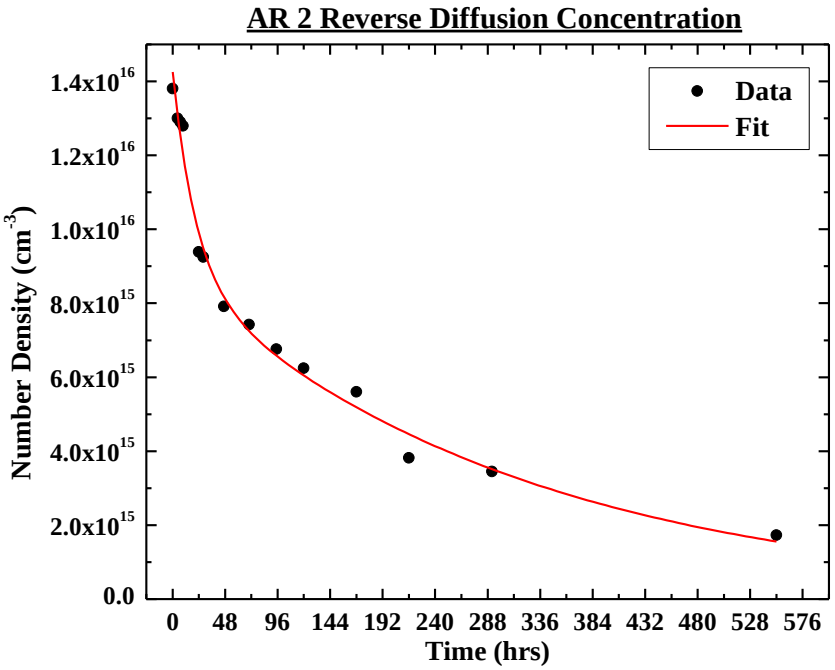

Figure 7-15. An example of the reverse diffusion concentration as a function of time for AR 2.

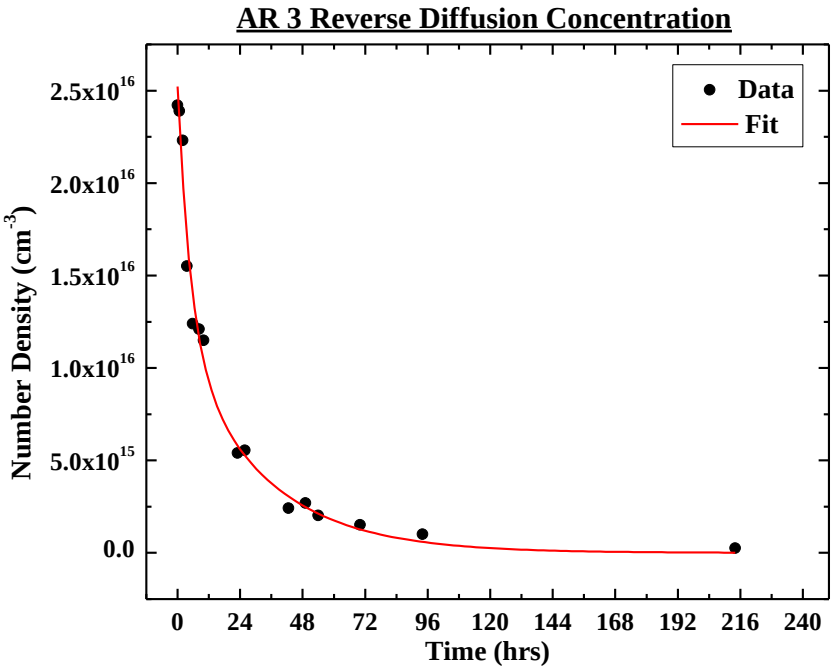

Figure 7-16. An example of the reverse diffusion concentration as a function of time for AR 3.

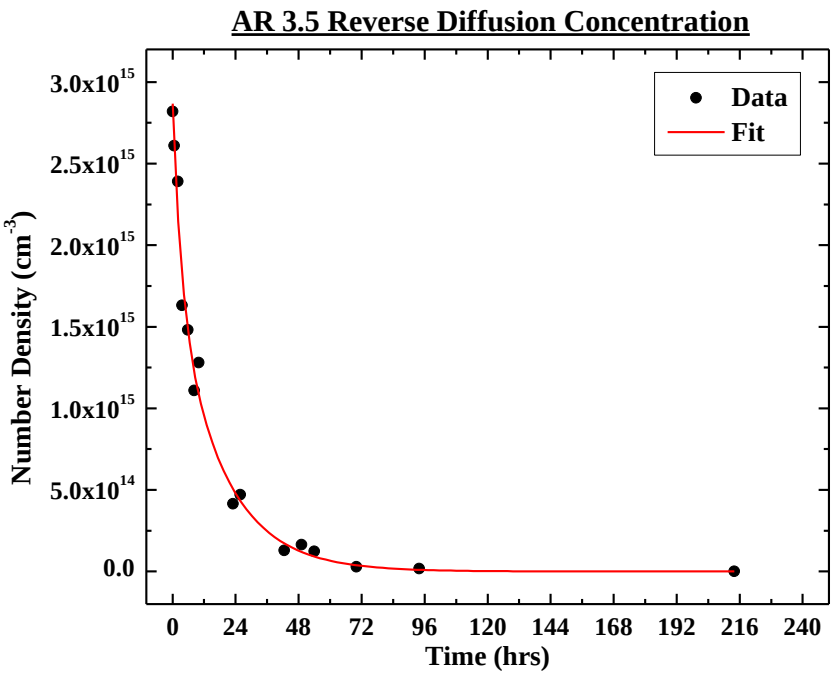

Figure 7-17. An example of the reverse diffusion concentration as a function of time for AR 3.5.

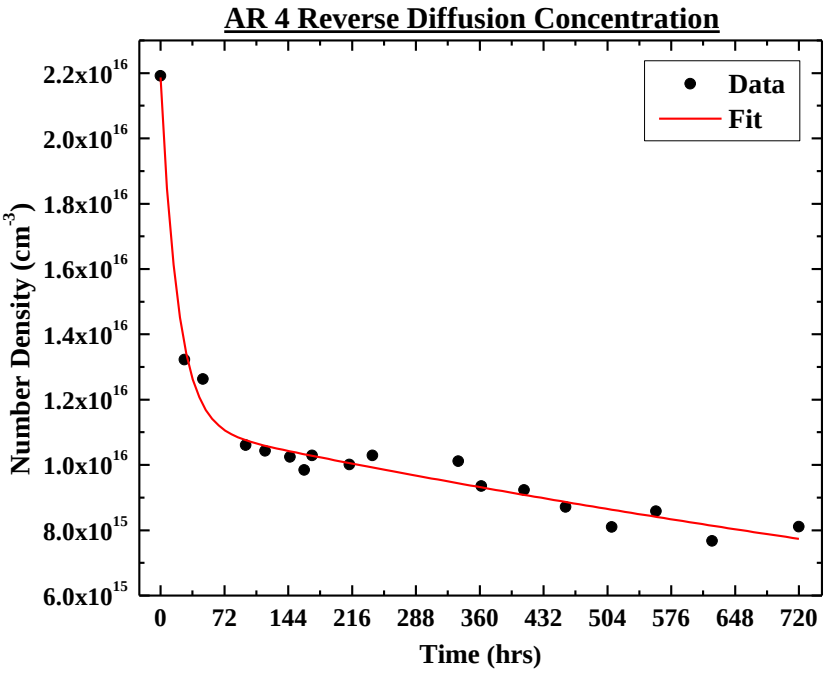

Figure 7-18. An example of the reverse diffusion concentration as a function of time for AR 4.

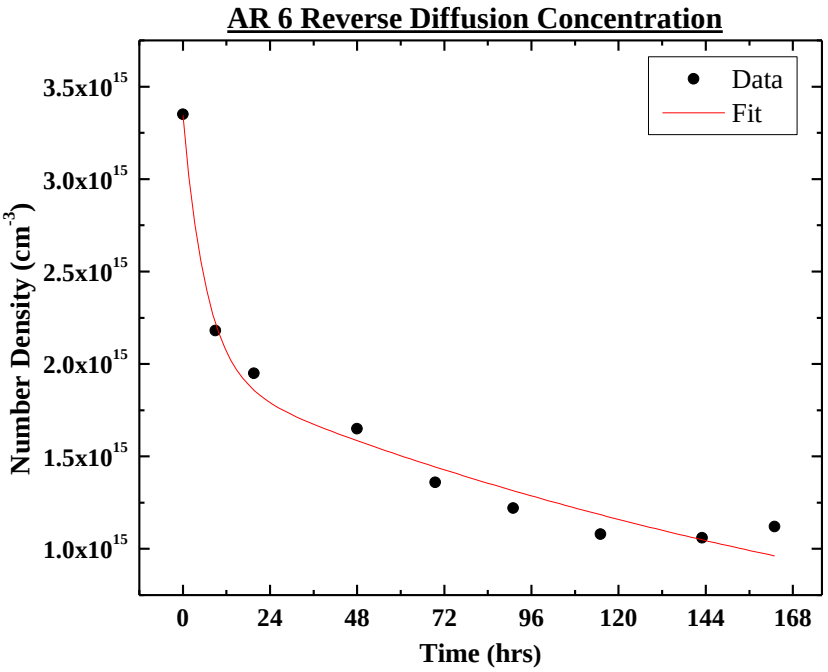

Figure 7-19. An example of the reverse diffusion concentration as a function of time for AR 6.

Table 7-2. Averaged Reverse Diffusion Fitting Parameters From Eq. 7-5.

AR	$C_{ads,wk}$ (x10^{15} NC cm^{-3})	τ_{wk} (hr)	$c_{ads,str}$ (x10^{15} NC cm^{-3})	τ_{str} (hr)
1	35.16±3.17	3.2±1.4	106.46±11.53	949±123
2	3.48±1.29	6.5±2.8	8.63±1.56	262±45
3	20.45±2.96	8.4±1.8	9.30±0.70	417±128
3.5	1.83±0.10	10.3±2.2	0.86±0.01	698±229
4	6.83±1.40	16.5±3.9	11.40±0.35	814±165
6	1.61±0.37	20.4±4.4	2.13±0.47	259±45

Additionally, we can also look at the time dependent profiles during the desorption process. Figures 7-20 to 7-25 show representative reverse diffusion concentration profiles as a function of time, where time 0 refers to the final forward diffusion profile. A general observation for all AR profiles is that the concentration decreases over the entire diffusion profile, however the profile does not appear to retract out of the nanochannel as it had originally progressed into the nanochannel during forward diffusion. Another interesting feature is that the NCs would still be expected to diffuse further into the nanochannels, but this feature appears to be absent from all of the ARs profiles. It remains hard to remark on the absence of the expected diffusion within the channels without a detailed study and modeling of the reverse diffusion profiles. In observing the time evolution of the concentration profiles, it should be noted that there still remains a portion of NCs adsorbed on the surface at times >100 hrs, except for AR 3 and 3.5. Specifically, ARs 1, 2, 4, and 6 still retain 56, 32, 61, and 28 % of the original NCs within the nanochannels, respectively, while ARs 3 and 3.5 retain <1%; all AR values are measured at ~200 hrs and 100 μm away from the nanochannel's exit/entrance. This observation of the profiles and quantities left on the surface would suggest that AR 3 and 3.5 behave much differently when adsorbing and desorbing from the surface. This leads us to carefully review the mechanism in which these NCs adsorb to the surface and subsequently how they desorb.

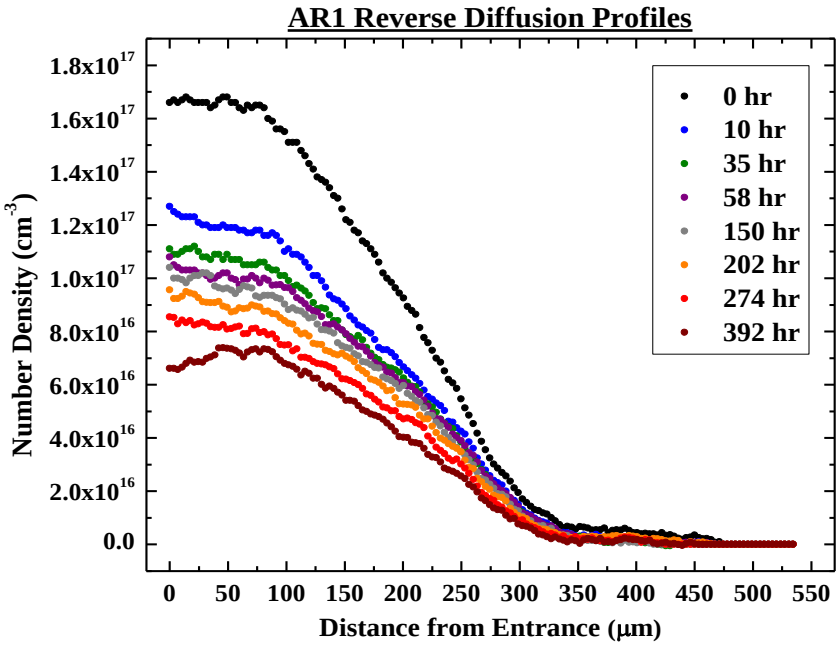

Figure 7-20. An example of the reverse diffusion concentration profile as a function of time for AR 1.

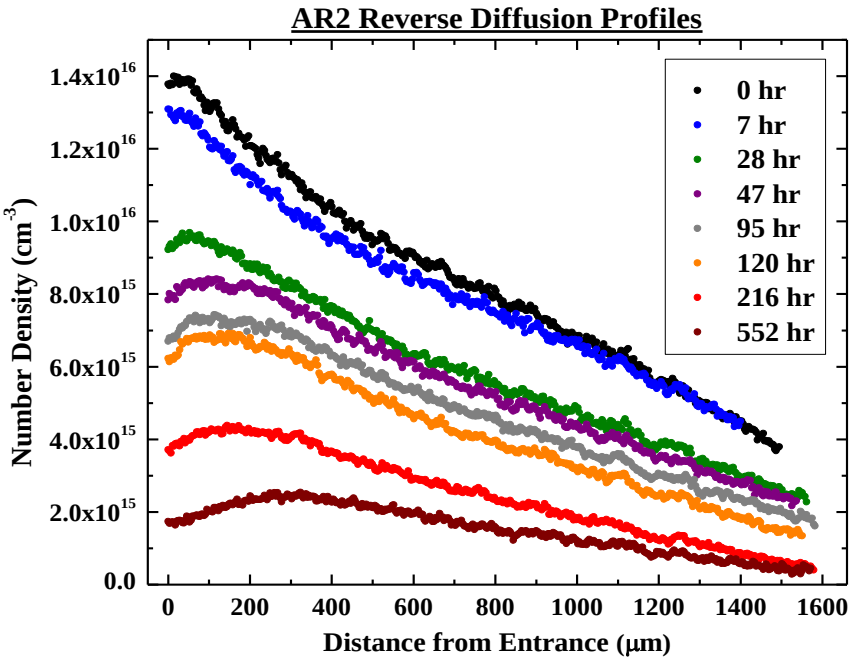

Figure 7-21. An example of the reverse diffusion concentration profile as a function of time for AR 2. Note that the NCs have diffused past the frame of reference and therefore appears to be cut-off.

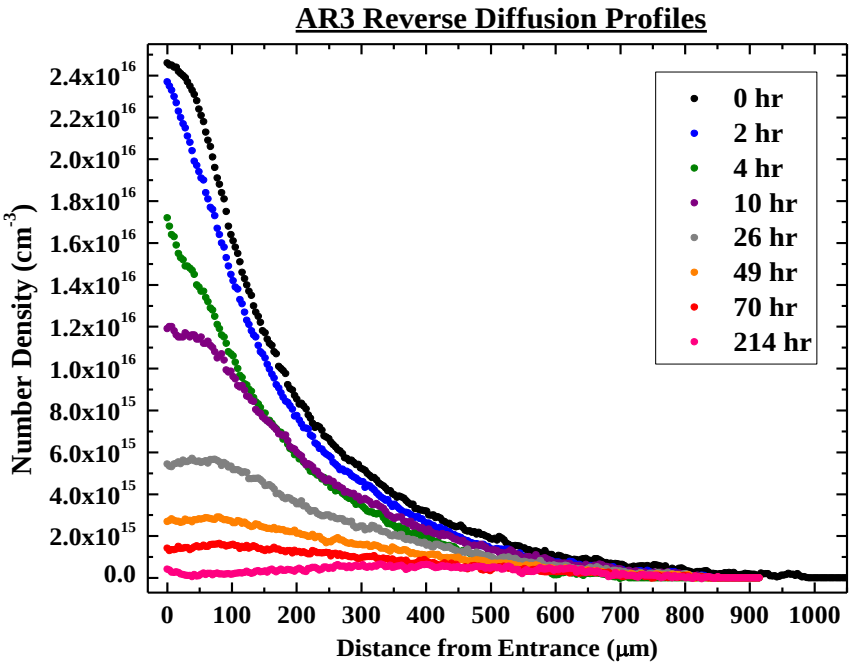

Figure 7-22. An example of the reverse diffusion concentration profile as a function of time for AR 3.

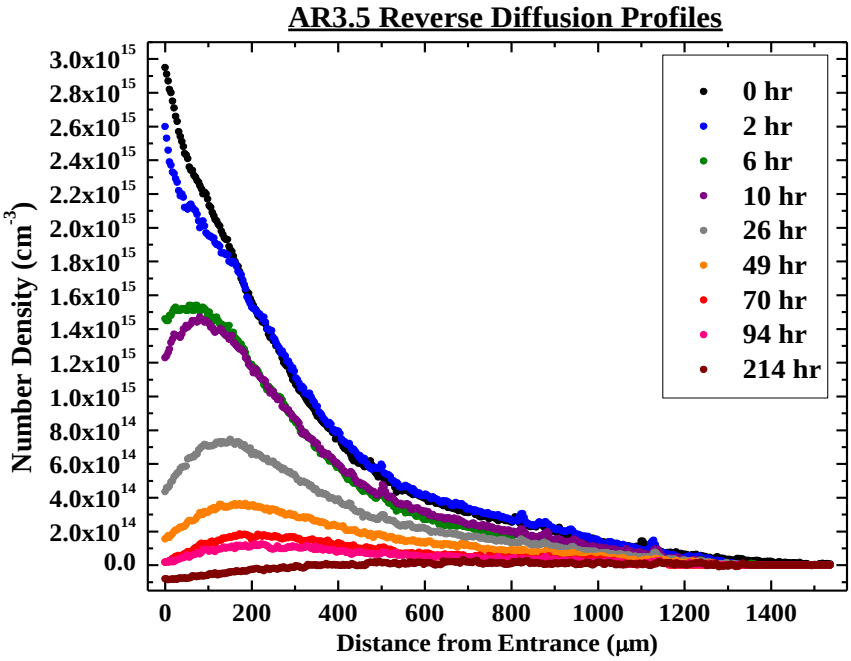

Figure 7-23. An example of the reverse diffusion concentration profile as a function of time for AR 3.5.

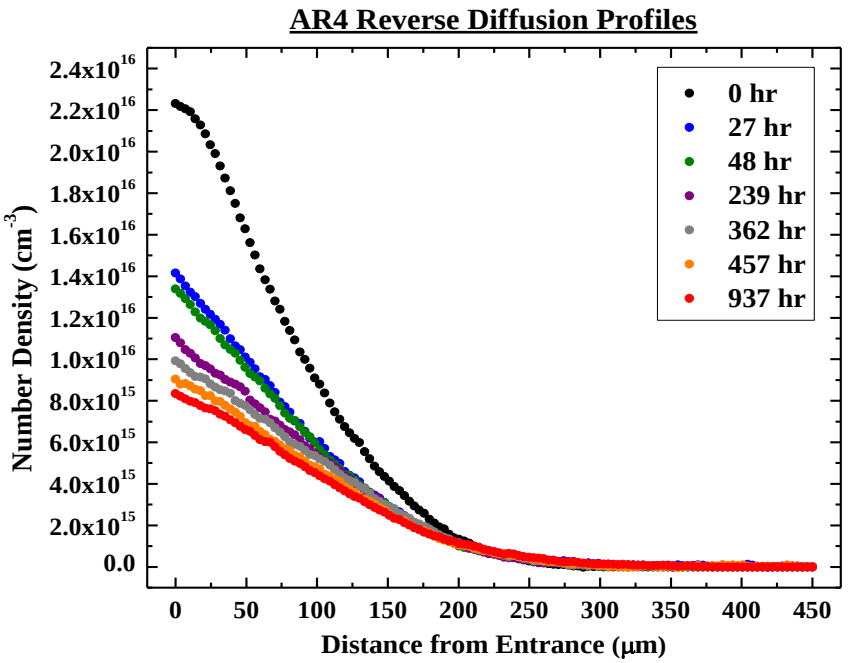

Figure 7-24. An example of the reverse diffusion concentration profile as a function of time for AR 4.

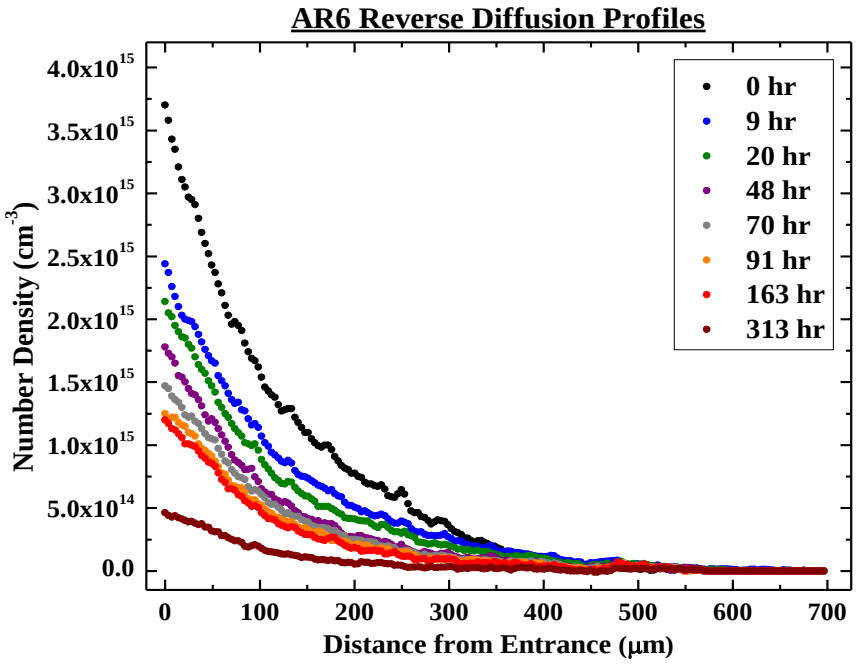

Figure 7-25. An example of the reverse diffusion concentration profile as a function of time for AR 6.

7.5 Mechanism of Adsorption and Desorption

From tracking the forward diffusion concentration as a function of time, it is hard to detail what the mechanism of adsorption is for anisotropic objects. More precisely, one expects that the orientation of an anisotropic object as it approaches the surface would play a pivotal role in how the object adsorbs to the surface, *e.g.* a rod can adsorb directly onto its side or initially by its tip. Currently, there are no publications that delineate the affects of the AR and size on the stability of tip-on and parallel adsorption for anisotropic molecules and particles. Simply comparing AR 2 to AR 6, one would think that there may be a vastly different equilibrium concentration of tip-on vs. parallel adsorbed species, mainly due to the difference in van der Waals forces (dispersive and attractive forces) acting upon the objects. In the particular case of an AR 2 NC, it is

expected that there is very little energetic difference between the two states of adsorption, as the attraction should be a function of surface area. This would clearly not be the case for an AR 6 NC.

Moreover, the governing physical parameters for anisotropic objects taking either a parallel or perpendicular orientation on a surface have yet to be adequately detailed in the current literature. Both computational simulations and experimental results agree, to some extent, that the bulk concentration and object's AR are the main governing parameters [110, 125-129], although there are very few experimental results to rely upon for nano-scaled objects. Interestingly, simulations and experiments still vastly differ in the magnitude of the bulk concentration required for different adsorption orientations to take place (by as much as 3-orders). Newer models based on more recent experimental insights have proven to close this gap considerably [125, 129].

Although the NC's forward diffusion behavior would suggest a single state of adsorption, the reverse diffusion data would suggest otherwise. We note that the absolute magnitude of $c_{ads,wk}$ and $c_{ads,str}$ is much greater than that of the reservoir concentration (c_{bulk}), which suggests that these concentrations correspond to NCs adsorbed to the channel walls. The first desorption mode, characterized by $c_{ads,wk}$ and τ_{wk}, is on the same time scale as pure diffusion (hrs), but has a concentration several times that of the predicted c_e. The second desorption mode, characterized by $c_{ads,str}$ and τ_{str}, is on the order of days. A few possible scenarios for the adsorption/desorption mechanism should be considered. It is expected that the NCs are homogeneously covered with a hydrocarbon surfactant that prevents any chemical binding (covalent binding) to the surface. So, if we consider multilayer adsorption of the NCs onto the SiO_2 surface, where a strongly bound

first layer is followed by subsequently weaker bound layer(s), an explanation for the two distinct τ constants would be plausible during the desorption process. However, since c_{sat} gradually levels off over time during the forward diffusion, and the saturation concentration is less than the volume equivalent maximum surface coverage of a monolayer (i.e. $c_{sat} < c_{mono}$, Figure 7-6), our quantitative results are inadequately explained by a multilayer adsorption process.

Another possibility is that the amorphous SiO_2 potential surface is rather heterogeneous. The distribution of chemical moieties, such as SiOH and SiH, or a physical corrugation of the surface may lead to two distinct adsorption sites. However, the differences in chemical and physical nature of a thermally grown SiO_2 surface are likely to exist over dimensions on the order of a few Angstroms, whereas the NC dimensions are on the order of nanometers. This explanation is therefore an unlikely candidate.

Another prospect is a "crowding effect", wherein the repulsive NC-NC interaction at higher surface coverage places the adsorbed NCs at a higher energy state, leading to a population of NCs that readily desorb. At low surface coverage, the NC-NC interaction is less pronounced due to the lack of neighboring NCs, and thus the NCs are strongly bound to the surface. Therefore, the crowding effect at high surface coverage provides a feasible physical interaction that can adequately explain the two distinct time constants associated with desorption. As an illustrative example of the crowding effect for spheres, Figure 7-26 (a-c) shows the RSA results for a surface coverage of 10, 30, and 50% [110]. After the irreversible adsorption of NCs to the surface one could further include the NC's hypothetical field of influence, represented by the cross hatched area, to

better understand the higher energy state that emerges with increasing surface coverage. Figure 7-26(d) shows a typical RSA illustration of a 45% surface coverage for an AR 15 [110]. Since we do not observe any agglomeration of NCs in the solution phase, we can rule out that the NC-NC interaction is attractive; if the NC-NC interaction were attractive a multilayer formation on the surface would also be possible, but again this is not evidenced by our data.

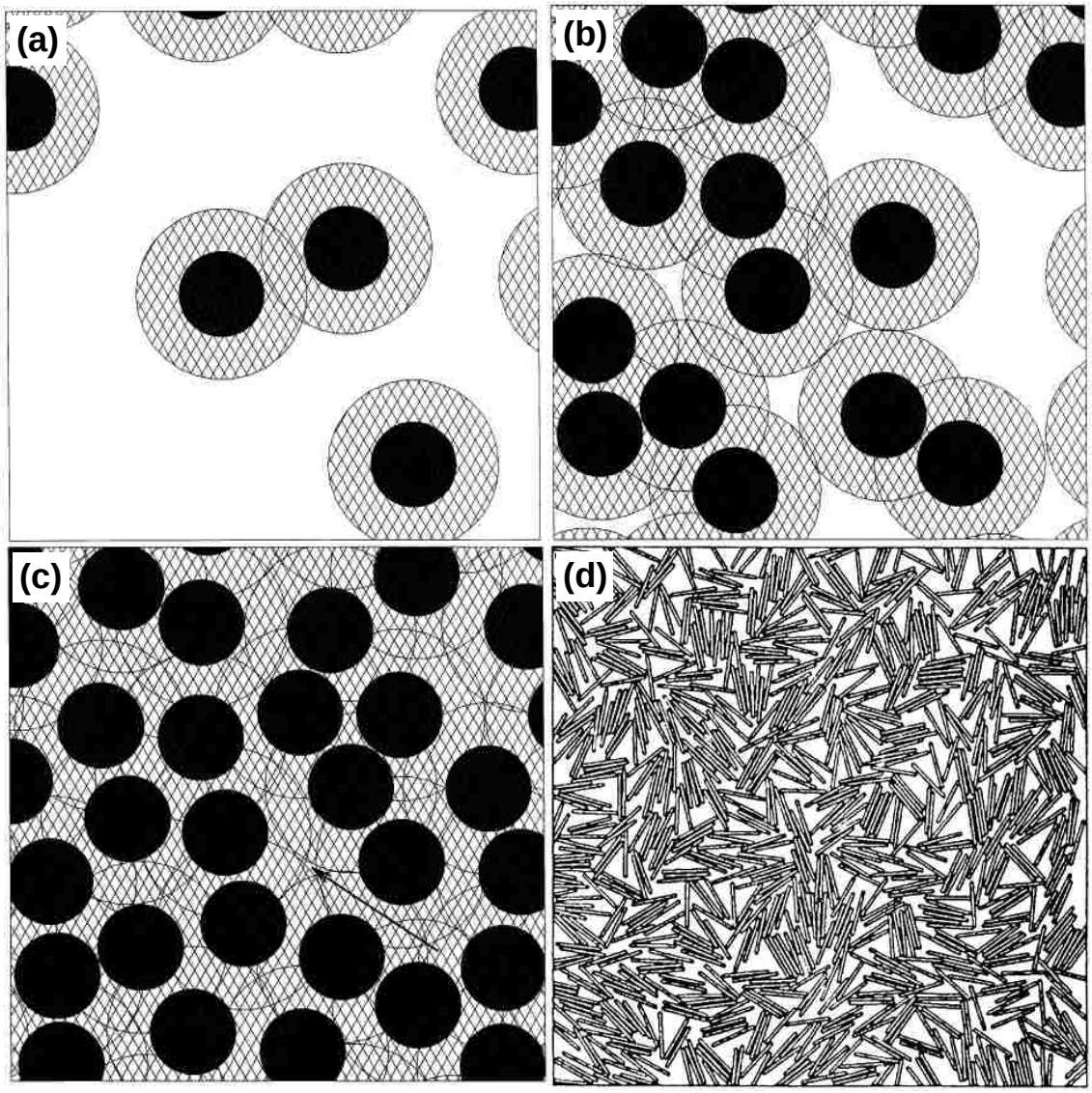

Figure 7-26. Talbot *et al.* illustration of typical RSA results for different surface coverage: (a) spheres at 10%, (b) spheres at 30%, (c) spheres at 50% with an arrow pointing to where room is available for another sphere, and (d) spherocylinders of AR 15 at 45%.

There is yet another possibility that was mentioned earlier, the mechanism in which NCs adsorb to the surface. For spherical particles, there is no orientation dependence on the NC's adsorption to the surface, essentially the spherical NC can have any orientation and still adsorb to the surface. However for spherocylinders, it is far more likely that the tip or end of the rod will hit the surface first, due to the rotational spin of the NC as it comes into contact with the surface. Potentially, a 2-step mechanism of adsorption may exist, where the initial contact by the tip leads to a perpendicular orientation or "tethering" of the NC to the surface. The tethered spherocylinder can then rapidly convert to a lower energy state by laying along its entire length on the surface (side-on), assuming there is no hindrance by neighboring NCs. It would be expected that the side-on state would be the majority of the adsorbed NCs at low surface coverage, while at higher surface coverage the NCs could tether to the voids left between the side-on NCs. The two states of adsorption would naturally have different desorption time constants and respective concentrations, and potentially vary with the NC's AR.

Schaaf *et al*. were one of the first groups to use ellipsometry experiments to characterize the adsorption of the anisotropic fibrinogen protein to a silica surface [117]. In their report, they observed a change in the adsorption layer thickness as a function of the bulk concentration. At a low bulk concentration (10^{-2} mg cm^{-3}), the fibrinogen lays parallel with the surface and forms a monolayer. As the bulk concentration increases they observed that the thickness of the adsorbed layer increased to the length of the fibrinogen. The data lead Schaaf *et al.* to suggest that a complex surface evolves as a function of the bulk concentration, wherein at high bulk concentrations (>0.5 mg cm^{-3}) the fibrinogen is suspected to be angled off of the surface and tethered by one end, rather

than laying parallel on the surface when at low bulk concentrations. Other techniques have reported a similar dependence on fibrinogen's bulk concentration influencing the concentration of the adsorbed layer, usually at a concentration ≥0.5 mg cm^{-3} [115, 126-128, 130]. These reports assume that either a multi-layer adsorption process is occurring or that an additional tethering of the fibrinogen to the surface voids is taking place. Our reverse diffusion results suggest that both a crowding effect, that is based on the surface's NC population, and/or an additional tethering of the anisotropic NCs to the available voids are reasonable explanations of the empirical results.

7.6 Single Site Modeling Results

Since we have entertained several possible desorption mechanisms to explain our reverse diffusion results, and have narrowed the possibilities to either a crowding or a tethering effect, we need to incorporate these physical details into an adequate model for the system. Before we get into detailing these effects, let's first develop some basic perspective on reversible adsorption systems. Much of the various transport models are described in Chapter 6, so we will start with the formalism of the equilibrium constant. We can describe our reverse diffusion results by the resulting equilibrium coefficient, typically the ratio of the adsorption constant (k_{ads}) and desorption constant (k_{des}). In the case of macroscopic single-site reversible adsorption, the equilibrium constant (K_{eq}) is classically defined as

$$K_{eq} = \frac{k_{ads}}{k_{des}} = \frac{c_{ads}}{c_{bulk}\, s_{opn}} \quad , \tag{7-6}$$

where c_{ads}, c_{bulk}, and s_{opn} is the total adsorbed concentration, the bulk reservoir concentration, and the open site density, respectively.

Evaluating our nanofluidic system at the entrance, after the long forward diffusion time and the observed saturation in concentration at the entrance, we consider the entrance to be at equilibrium with the reservoir. Similarly, the adsorption and desorption of NCs within this region must also be at equilibrium with one another. By considering a single-site mechanism of adsorption, we can fit the experimental data by reducing the inherent complexity of the two-site adsorption, to a more manageable number of variables. The single site model allows us to calculate some approximate values, but more importantly allows us to understand how the variables affect the overall fitting of the data. See Appendix B for the Mathematica code used in the single site modeling of the data.

However, for the single site model we would like to incorporate some aspect of the reverse diffusion modeling results produced by Eq. 7-5. In particular, Eq. 7-5 describes two states of adsorption where the weakly bound concentration ($c_{ads,wk}$) was experimentally indistinguishable from the freely diffusive NCs (c_e). We can impose, for the sake of argument, that the local freely mobile phase within the nanochannels is actually the sum of c_e and $c_{ads,wk}$; although we know this to be a physical misrepresentation of the system, the overall dynamics will be better represented in the single site model. If we consider our system to be described as a reversible single-site adsorption system, then there is only one K_{eq} value needed to describe the system's ratio of adsorption to desorption constants. For clarification of our simple model, $c_e + c_{ads,wk}$ must represent the local quantity of NCs that easily diffuse out of the nanochannels, rather than just c_{bulk} or c_e, and therefore $c_{ads,str}$ represents the amount of NCs adsorbed on

the surface. Using these definitions, the single site equilibrium coefficient can be expressed as

$$K_b = \frac{c_{ads,str}}{(c_e + c_{ads,wk})\, s_{opn}} \quad . \tag{7-7}$$

The K_b provides the ratio between the adsorption rate (k_{ads}) and desorption rate constants (k_{des}), thus allowing the system to be solved for the relevant variables. The fitting results of AR 1 and AR 4 are shown in Figure 7-27 and 7-28, respectively. We further report the average equilibrium coefficient (K_b), desorption rate constant (k_{des}), adsorption rate constant (k_{ads}), and diffusion coefficient (D_c) in Table 7-3.

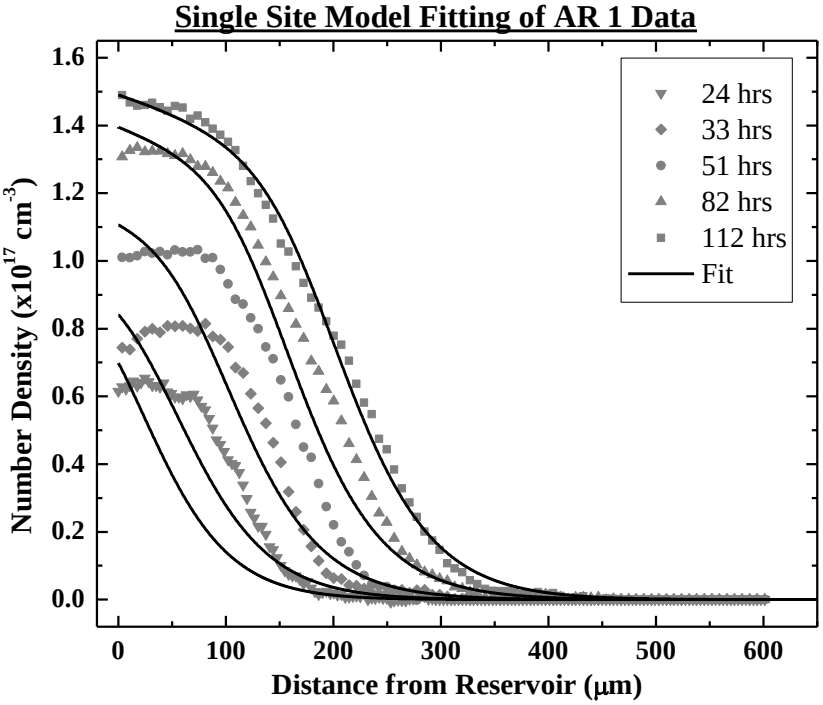

Figure 7-27. A comparison of the average single site model fitting parameters against the forward diffusion profiles of AR 1.

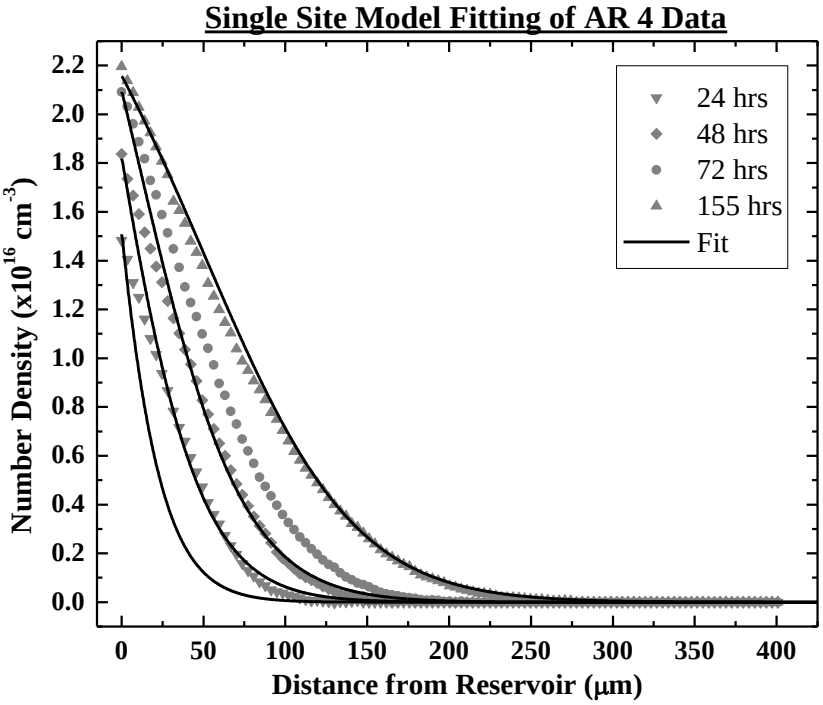

Figure 7-28. A comparison of the average single site model fitting parameters against the forward diffusion profiles of AR 4.

Table 7-3. Fitting Results for a Single Site Adsorption Model.

AR	K_b ($x10^{-11}$ cm^2 NC^{-1})	k_{des} ($x10^{-6}$ s^{-1})	k_{ads} ($x10^{-17}$ cm^2 NC^{-1} s^{-1})	D_c ($x10^{-9}$ cm^2 s^{-1})	D_{bulk} ($x10^{-6}$ cm^2 s^{-1})
1	1.75±0.14	5.34±2.62	9.36±0.75	1.14±0.15	2.03
2	0.61±0.20	5.93±1.21	3.59±1.16	2.04±0.69	0.83
3	0.18±0.03	3.08±0.50	0.55±0.08	3.76±0.35	0.71
3.5	0.19±0.03	12.58±1.31	2.39±0.38	5.51±0.36	0.60
4	1.05±0.21	15.70±6.42	16.41±3.26	0.18±0.04	0.54
6	0.97±0.26	16.22±7.72	15.65±4.26	0.39±0.03	0.47

Although the single site model is capable of fitting all of the various AR profiles, the model doesn't accurately account for the two types of desorption observed in the reverse diffusion results. Therefore, the data will be cautiously reviewed and discussed. First, it needs to be emphasized that the data fits shown in Figures 7-27 and 7-28 show the average fitted parameters for times >100 hrs of forward diffusion projected onto earlier data sets. It can be clearly seen that the model can not effectively fit times <100 hrs and would suggest that at surface coverage less than the equilibrium value, the dynamics of the adsorption process are substantially different than at equilibrium. Again, this evidence substantiates the aforementioned mechanisms of adsorption that would appear to deviate from a classical Langmuir isotherm definition of the equilibrium coefficient. More precisely, the adsorption behavior at low surface coverage is much different than at higher surface coverage, most likely due to the increased NC-NC interactions on the surface.

For the equilibrium coefficients, Figures 7-29 and 7-30 reveal that there is a substantial decrease in the fitted K_b as the AR $\rightarrow$ 3, with a small recovery for AR 3.5, and larger values for 4 and 6. The trend would tentatively suggest that there is indeed a fundamental difference in the adsorption/desorption dynamics for low AR NCs ($1 < AR \leq 3.5$) as compared to the NCs with an AR ≥ 4. Since the adsorption process is primarily due to an attractive van der Waal's force and the binding strength is proportional to the NC's surface area, the observed K_b trend in general appears to be counter-intuitive, especially for ARs from 2 to 3.5. We would expect that the higher surface area of the spherocylinders to have an increasing K_b trend as a function of AR, instead of the apparent decrease. The K_b values may suggest that a change in shape is the root cause for

the observed decreasing values. Although, it should be pointed out that comparing the k_{ads} values of AR 1 to ARs 4 and 6, would seem to substantiate that the longest ARs do adsorb stronger than AR 1.

These modeled K_b results do bring us back to the topic of the potentially different physical adsorption for low AR NCs as compared to higher AR NCs. In particular, the energetic difference between side-on and tethering adsorption states for low AR NCs may not be significantly different, and therefore the resulting equilibrium concentration for the tethered state maybe much higher than larger AR NCs (≥ 4). Reiterating, for low AR NCs there is a higher percentage of tethered NCs than there would be at higher ARs. This would also suggest that higher AR NCs do in fact experience a larger dispersion force (a repulsive van der Waal force based on the NC's mass) that must reduce the amount of tethered NCs on the surface. Comparison of K_b and D_c for ARs ≥ 4 illustrates the substantially decreased diffusivity of the NCs as the van der Waal's force becomes dominant (K_b increases as compared to low AR NCs), again suggesting that a side-on adsorption maybe preferred with little to no stability for the tethered state.

As a consequence of the apparent K_b, the observed D_c for mildly elongated NCs ($1 < AR \leq 3.5$) actually increases when compared to the spherical NCs (AR 1), as shown in Figure 7-31. Although the provided single site transport model accounts for the adsorption of NCs within the nanochannels, the reported diffusion coefficients (D_c) are still 3-orders of magnitude lower than the calculated diffusion coefficients for diffusion in an unconfined large volume. However, it bears repeating that these single site modeling values do not capture the true desorption process within the system, and therefore maybe misleading.

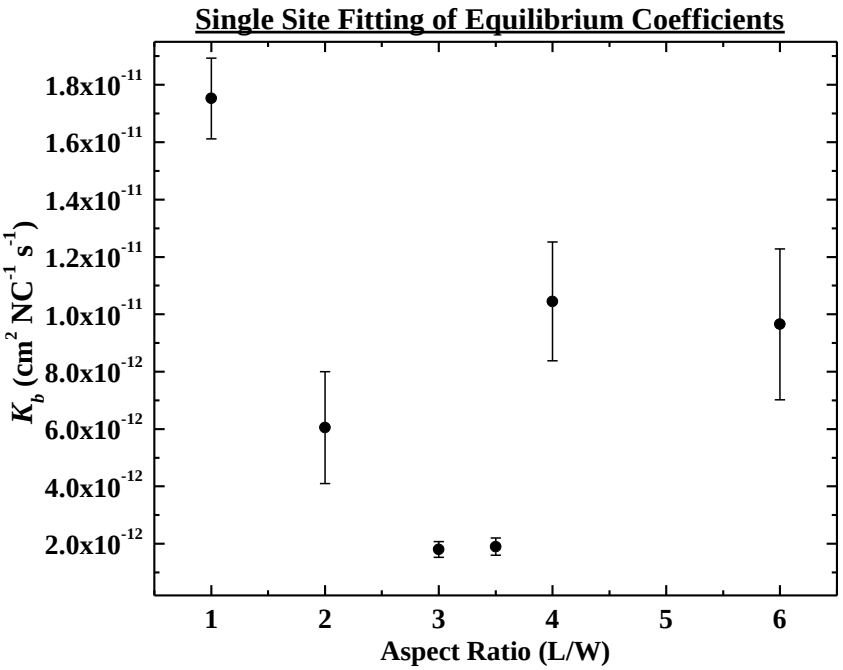

Figure 7-29. A linear plot of the single site fitting values for the equilibrium coefficient as a function of AR, established by Eq. 7-7.

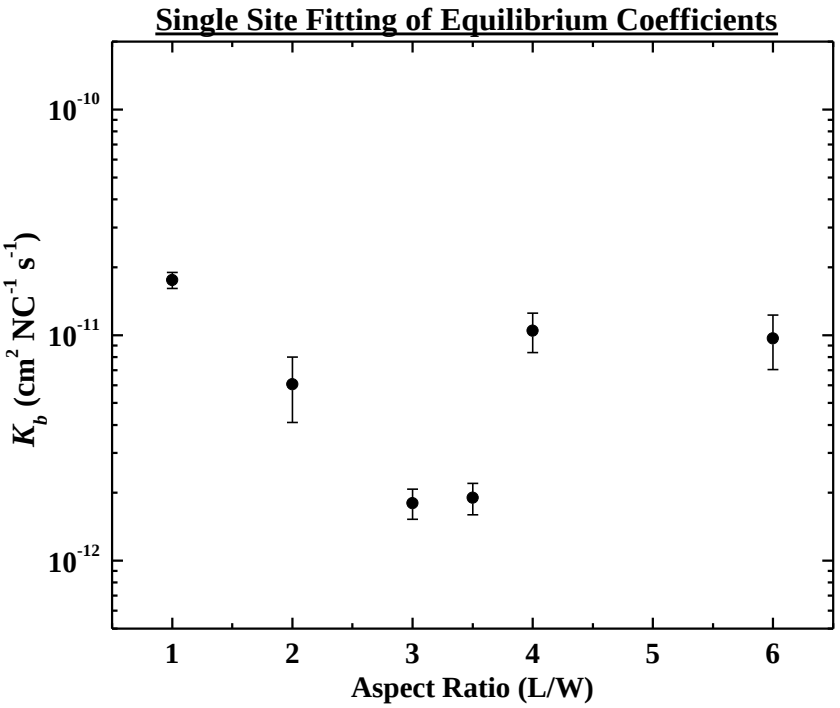

Figure 7-30. A log-scale plot of the single site fitting values for the equilibrium coefficient as a function of AR, established by Eq. 7-7.

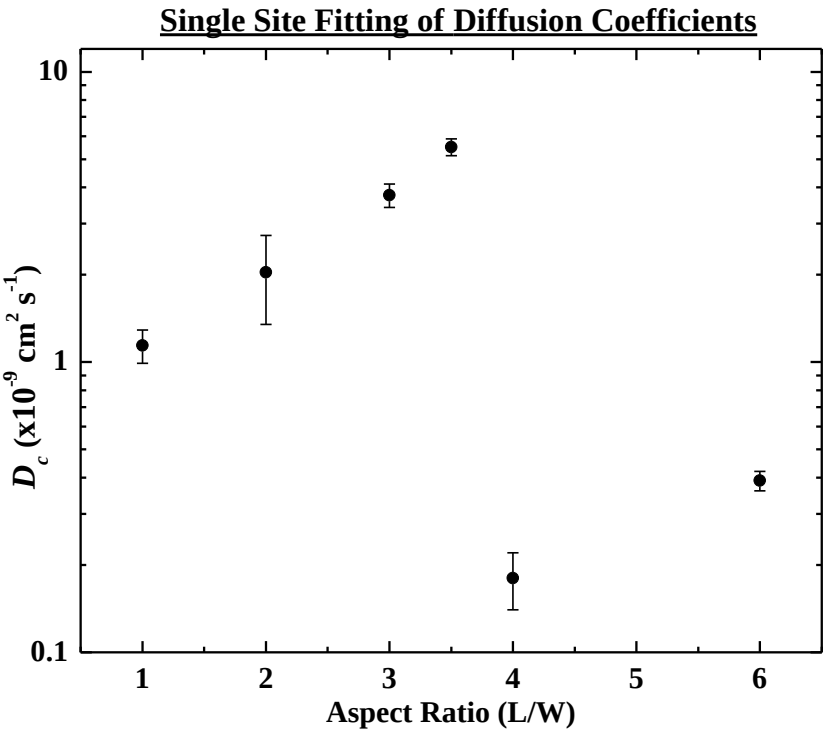

Figure 7-31. A plot of the single site fitting values for the diffusion coefficient as a function of AR.

7.7 Two-Site Modeling Results

Since the single site model has been analyzed and the profiles fitted, we move on to the complication of adding a secondary desorption event to the transport model. We expect that the initial adsorption event, or adsorption constant, is considered equal between the two-states. We believe this to be reasonable because the *Pe* number is small and therefore the NCs sample the wall's surface at a high rate. By fitting the reverse diffusion data with Eq. 7-5, the two apparent desorption processes can be quantified and compared. Examination of the $c_{ads,wk}$ term reveals that for all ARs the amount of NCs in the initial out-diffusion process is several times higher then the expected equilibrium concentration (c_e). To look further into these results and to provide a sensible physical

model for the desorption process, we examined the fractional concentrations for the weakly (F_{wk}) and strongly (F_{str}) bound NCs that are described by

$$F_{wk} = \frac{c_{ads,wk}}{c_{ads,wk} + c_{ads,str}} \quad \text{, and} \tag{7-8}$$

$$F_{str} = \frac{c_{ads,str}}{c_{ads,wk} + c_{ads,str}} \quad . \tag{7-9}$$

Plotting the fractional desorption amounts for F_{wk} and F_{str} as a function of AR, we can further gain insight into the magnitude of each desorption process, shown in Figure 7-32.

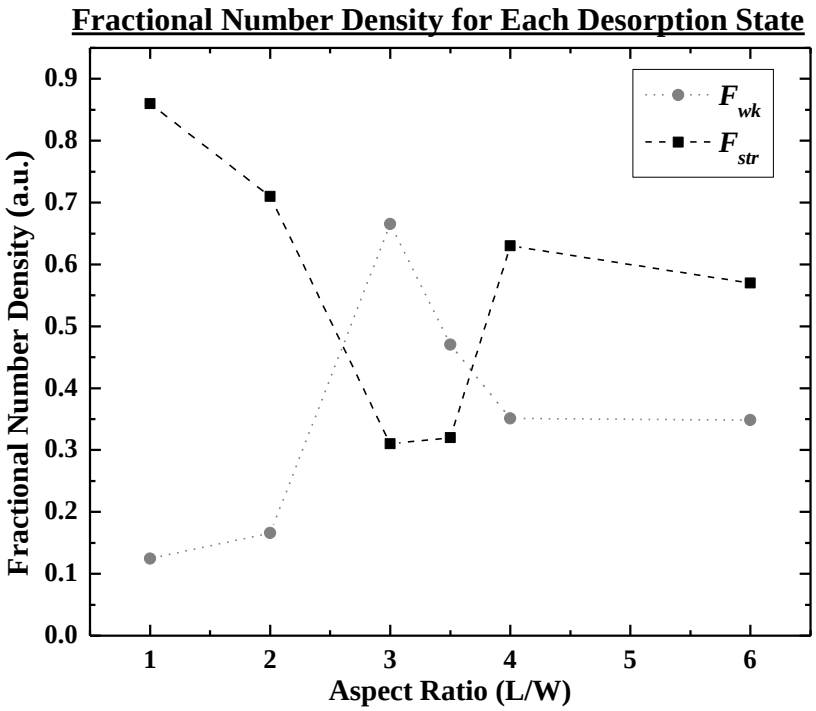

Figure 7-32. A plot of the fractional number densities for the weakly and strongly bound NCs as a function of AR, as described by Eq. 7-8 and 7-9.

Reviewing the results of F_{wk} and F_{str}, it appears that an additional complexity may exist around an AR 3. For F_{str}, a general monotonic decrease as a function of increasing AR is observed. Similarly, an increase for F_{wk} is observed as the AR increases. However, AR 3 and 3.5 appear to behave much different than the general trends would suggest. These results appear to disagree with only an increase in the attractive van der Waal's force as the AR increases, and would indicate that a secondary dispersive force maybe responsible for the discrepancy centered at AR 3. Nevertheless, a two-site model will be able to produce a more accurate description of the two desorption processes and their resulting dynamics. See Appendix C for the Mathematica code used to model the data.

Before the results of the two-site model are discussed, there needs to be some clarification as to how the weak ($K_{b,wk}$) and strong ($K_{b,str}$) equilibrium coefficients are fitted in the model. Initially, the weak and strong equilibrium coefficients are estimated from the reverse diffusion fitting (Eq. 7-5) by

$$K_{b,wk} = \frac{c_{ads,wk}}{c_e \; s_{opn}} \quad \text{, and} \tag{7-10}$$

$$K_{b,str} = \frac{c_{ads,str}}{c_e \; s_{opn}} \quad . \tag{7-11}$$

In the case of the two-site model, each equilibrium coefficient is further fitted by relating each states' contributing concentration to the corresponding reverse diffusion concentration, whereby each is individually modeled and plotted in the Mathematica code and verified by the $c_{ads,wk}$ and $c_{ads,str}$ values (see Figures 7-33 and 7-34). This is similar to taking Eq. 7-10 and dividing by Eq. 7-11 to produce an estimate of the ratio between the equilibrium coefficients, which would be expected to be similar to the relative concentration ratio in the model; but this is only used as a basic guideline for the

modeling and is further iterated upon to produce the best fit. Furthermore, it is quite apparent that the proper fitting of the experimental data as a function of time can only be obtained near equilibrium conditions, or in other words near c_{sat}. The reasoning follows that the c_e value used in Eqs. 7-10 and 7-11 actually has a time dependency due to the system being transport limited. It was briefly mentioned earlier that we do not know how the complexity of adsorption process depends on the c_e value within the nanochannels. As Schaaf *et al*. had previously discussed in their fibrinogen study, the equilibrium concentration greatly affects the resulting adsorption state of the molecules, and naturally their desorption from the surface [117]. Therefore fitting the profile data at non-equilibrium times would be difficult and the results questionable. Again, we do not know how the surface coverage changes with c_e or for that matter the partitioning between the adsorbed surface states at non-equilibrium conditions (low surface coverage). Lacking this critical data, we instead fit the data near or after the saturation concentration has been reached at times >100 hrs of forward diffusion or what we consider to be equilibrium.

Although the fitting values are reported at times >100 hrs of forward diffusion and we have clearly stated that the two-site model should not be applied to fitting results collected at low surface coverage, examples are shown for the average fitting parameters projected as a function of time on corresponding data sets of AR 1 and AR 4 in Figures 7-35(a) and 7-36(a) respectively. It should be noted that in order to obtain better fits for the lower surface coverage at shorter times (see Figures 7-35(b) and 7-36(b)), the K_b values were kept constant with time and the k_a value was allowed to be refit accordingly. Comparison of the k_a values at low and high surface coverage was found to increase by at least 1 to 2 orders of magnitude at low surface coverage. This clearly illustrates the fact

that the mechanism of adsorption is dependent on the surface coverage. However, solving the two-site model described in Chapter 6 (Eqs. 6-15 to 6-27) at or above equilibrium allows us to report the average equilibrium coefficients ($K_{b,wk}$ and $K_{b,str}$, shown in Figure 7-37), desorption rate constants ($k_{d,wk}$ and $k_{d,str}$), adsorption rate constant (k_a), and diffusion coefficient (D_c) shown in Figure 7-38, and are all summarized in Table 7-4.

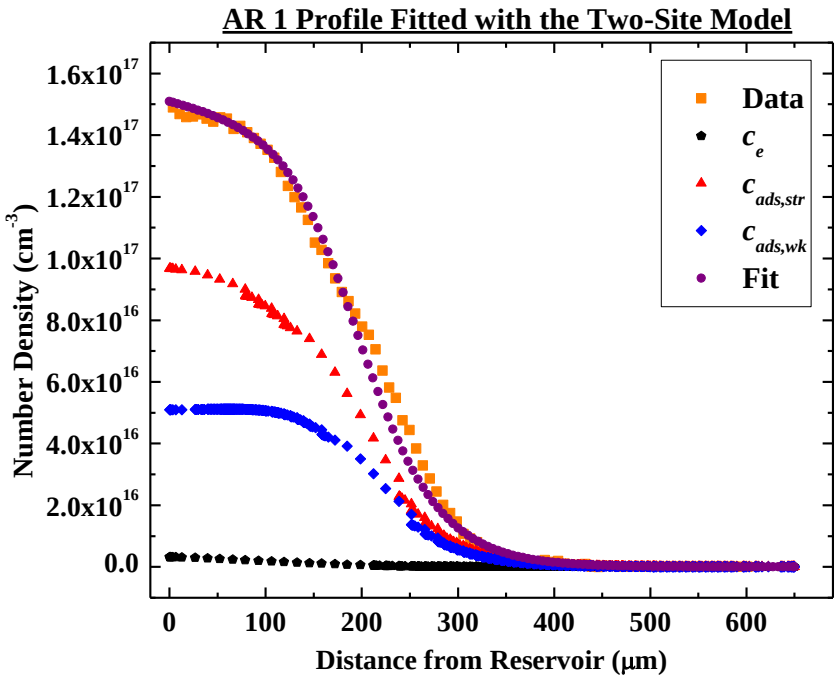

Figure 7-33. An example of an AR 1 forward diffusion profile (orange) fitted with the respective two-site model components. The data fit (purple) includes the sum of the individual contributions of c_e (black), c_{str} (red), and c_{wk} (blue).

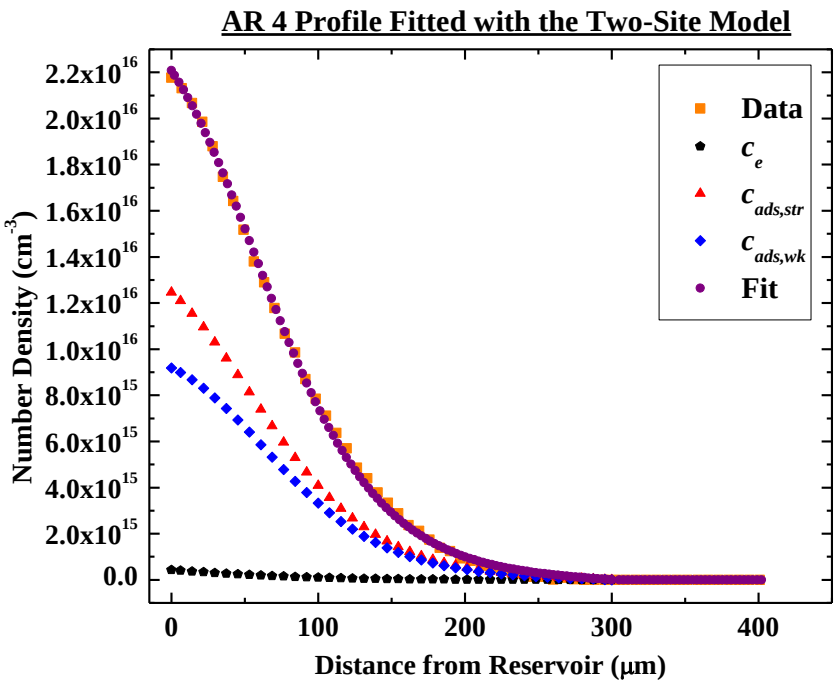

Figure 7-34. An example of an AR 4 forward diffusion profile fitted with the respective two-site model. The data fit (red) includes the contributions of c_e (green), c_{str} (blue), and c_{wk} (purple).

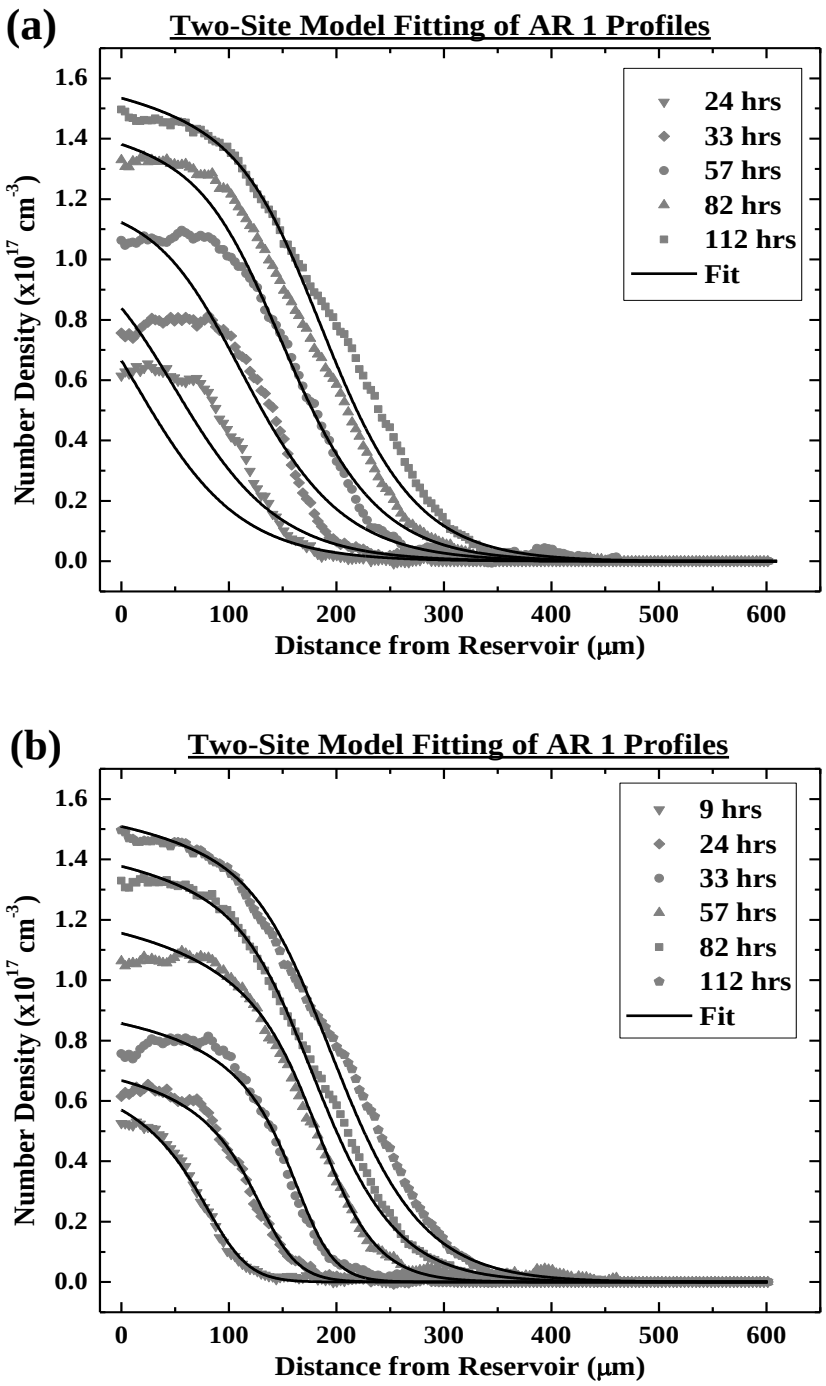

Figure 7-35. (a) A comparison of the average two-site model fitting parameters against the forward diffusion profiles of AR 1. (b) An example of the two-site model fitting of the forward diffusion profiles for AR 1 while allowing the refitting of the k_a value at each time step.

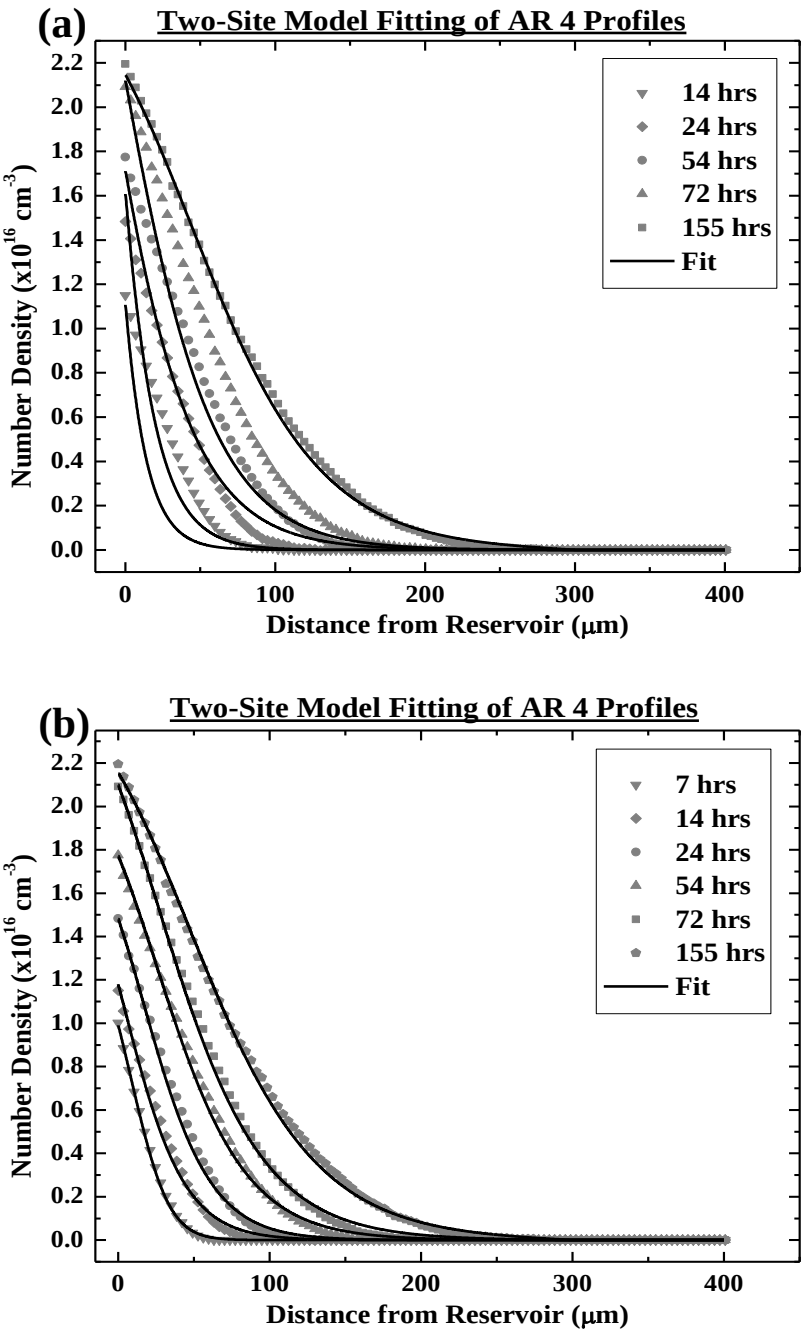

Figure 7-36. (a) A comparison of the average two-site model fitting parameters against the forward diffusion profiles of AR 4. (b) An example of the two-site model fitting of the forward diffusion profiles for AR 4 while allowing the refitting of the k_a value at each time step.

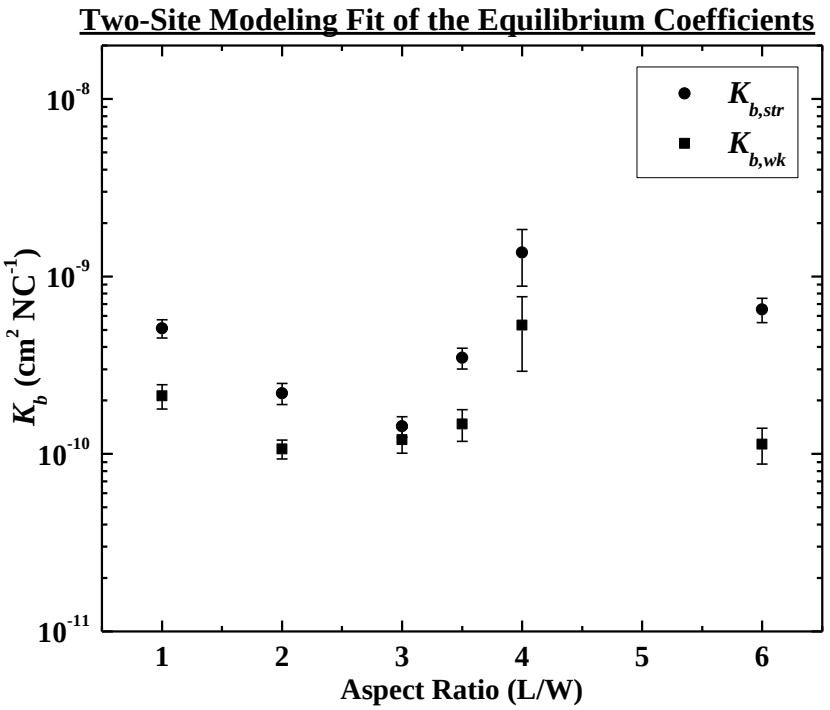

Figure 7-37. A plot of the two-site fit for the weak and strong equilibrium coefficients as a function of AR.

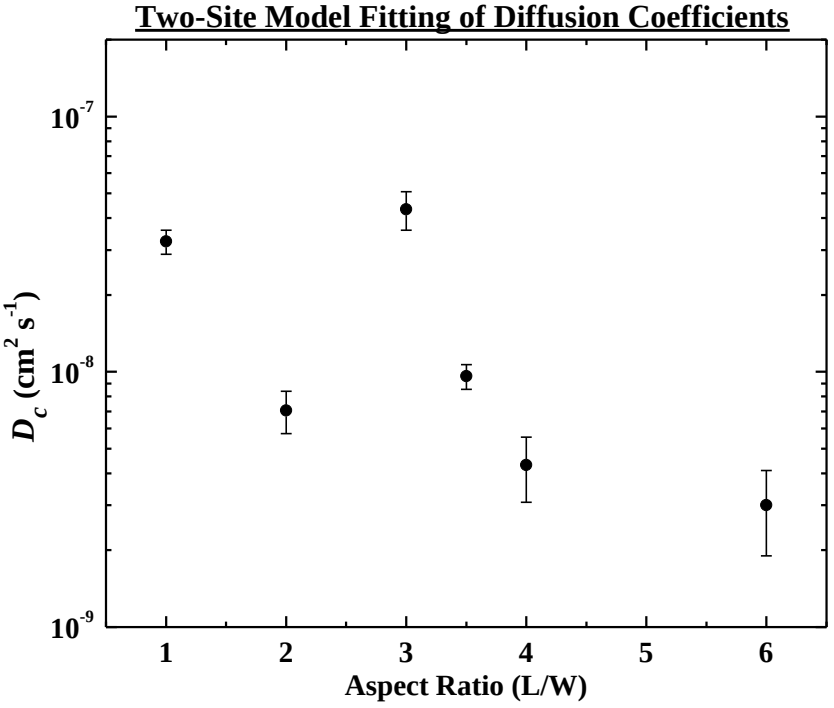

Figure 7-38. A plot of the two-site fit for the diffusion coefficient as a function of AR.

Table 7-4. Fitting Results for a Two-Site Adsorption Model.

AR	$K_{b,str}$ ($\times 10^{-10}$ cm^2 NC^{-1})	$K_{b,wk}$ ($\times 10^{-10}$ cm^2 NC^{-1})	k_a ($\times 10^{-15}$ cm^2 NC^{-1} s^{-1})	$k_{d,str}$ ($\times 10^{-6}$ s^{-1})	$k_{d,wk}$ ($\times 10^{-6}$ s^{-1})	D_c ($\times 10^{-8}$ cm^2 s^{-1})
1	5.10±0.60	2.12±0.33	1.60±0.48	3.13±1.04	7.53±2.06	3.24±0.35
2	2.12±0.30	1.07±0.13	1.07±0.12	4.86±0.87	10.02±1.65	0.71±0.13
3	1.43±0.19	1.20±0.19	0.82±0.12	5.69±0.87	6.79±0.74	4.33±0.74
3.5	3.48±0.27	1.48±0.30	1.11±0.11	3.19±0.32	7.54±1.08	0.96±0.11
4	13.62±4.79	5.31±2.39	1.45±0.11	1.06±0.40	2.73±1.17	0.43±0.12
6	6.50±1.01	1.14±0.26	0.36±0.08	0.55±0.08	3.13±0.65	0.30±0.11

Discussing the model's fitted equilibrium coefficients first; Figure 7-37 reveals a decrease in K_b as AR 1 is slightly elongated to an AR 2. This would suggest that the change in shape from a sphere to a spherocylinder could have substantial ramifications in the particle's interaction with the surface [110, 131, 132]. Furthermore, the K_b as a function of AR form a valley in-between AR 1 and AR 4, after which the $K_{b,str}$ appears to be comparable to AR 1. It should be mentioned that the rather large error in AR 4's K_b comes from the apparent diversity in data, and not the fitting itself. Additionally, $K_{b,str}$ and $K_{b,wk}$ appear to converge to a similar value as the AR approaches 3, and then diverges from one another as the AR further increases. The convergence and divergence could suggest that the van der Waals dispersion and attractive forces are changing as a function of AR [132]. For AR 3 NCs the two equilibrium states, a tethered vs. a side-on position, are partitioned similar and could further signify that the two states are energetically close to one another at this AR. Alternatively, an assessment of the surface density by RSA suggests that the maximum surface density is reached at an AR ≈ 2 [110]. If we recall, the inclusion of the surfactant length for an AR 3 NC modifies the physical AR ≈ 2.3. It would seem plausible that a higher density of spherocylinders would result in a higher

surface energy, leading the $K_{b,\,wk}$ partitioning comparable to $K_{b,str}$. However, it is hard to quantify the ramifications of a seemingly small predicted change in surface occupation, 6% by RSA for ARs 2 to 6, in terms of the observed kinetics. Therefore, the crowding effect can not be completely dismissed and suggests further study by RSA simulations is needed. Luckily, there appears to be paths already forged to do just such simulations [110, 125, 133].

In the interest of further clarifying the convergence and divergence of K_b, we plot the ratio of the two K_b ($K_{b,str}$ / $K_{b,wk}$) in Figure 7-39. Here again we observe two features, a decrease in the K_b ratio centered at an AR ≈ 3, and thereafter a noticeable rise to a maximum value at AR 6 that is roughly ×2 that of AR 1. Furthering our previous discussion in the Single Site Model, the observed phenomenon maybe explained by the balance between the dispersion force and the attractive van der Waals force acting upon the NCs as a function of AR. Dispersion forces are typically a function of the particle's weight, thus growing as a function of volume, where as the attractive van der Waals force is a function of the NC's surface area. Specifically, as a NC's mass increases or in our case as the AR increases, the dispersion force exerted on a tethered NC would eventually overcome the attractive van der Waals force acting on the tip's surface, thus decreasing the NC's propensity for the weakly bound state. Conversely, as the AR increases the van der Waals force exerted on a fully adsorbed NC with a side-on orientation on the surface will also increase, and the adsorbed surface concentration will predominantly contain strongly bound species ($K_{b,str}$). The apparent K_b ratio shown in Figure 7-39 as a function of increasing AR, qualitatively tracks well for NCs that experience an increasing

attractive van der Waals force (increasing $K_{b,str}$) and an increasing dispersion force (observed as the K_b ratio increases after AR 3).

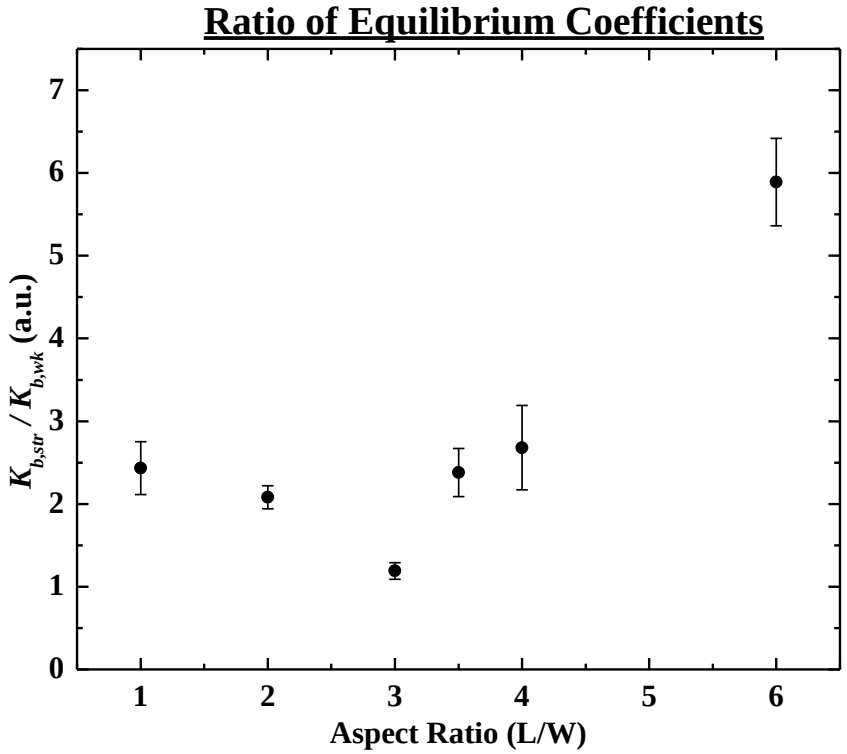

Figure 7-39. The ratio of the equilibrium coefficients as a function of AR.

As a consequence of the K_b dynamics, the effective diffusion coefficient (D_c) for the mildly elongated AR 3 is slightly faster than AR 1, as shown in Figure 7-38. However, in general the NC's D_c appears to decrease as the AR increases, and is especially apparent when looking at ARs > 3. The D_c would appear to track well with the K_b ratio although AR 2 does appear to have a lower then expected D_c. Comparison of the calculated diffusion coefficients for NCs freely diffusing in an unconfined large volume to the modeled D_c, the reported values are still found to be 1 to 2 orders of magnitude lower then their bulk counter parts. This could suggest that a more general steric exclusion at the nanochannel opening may still need to be incorporated into the model,

similar to Anderson and Quinn's analysis of the pore permeability [55]. In fact our results suggest that the NC permeability (ξ) is on the order of 10^{-2} to 10^{-3}, where $\xi = \frac{D_c}{D_{bulk}}$; typical values for micro-porous membranes range between 0.7 and 1. This would lead us to re-evaluate the classic definitions for the steric exclusion and hindered diffusion of particles into nanofluidic channels, and is left to be done at a later time.

7.8 Future Work

This body of work has clearly outlined several prospective paths of research that need to be addressed. First, it is highly recommended that a macroscopic experiment be devised that can substantiate the tethering process for NCs as a function of the surface concentration. It has been suggested that the use of a flat waveguide or surface be used to probe the orientation dependence of the NCs at different solution concentrations, e.g. a Si waveguide or surface with a thin oxide layer that could be probed by second harmonic spectroscopy [134] or thermoreflectance spectroscopy [135]. Secondly, computational methods such as Monte Carlo simulations need to be performed to elucidate the bonding energy differences between the two proposed mechanisms (orientation dependence and crowding effect) that will provide additional insight into the two-state adsorption observed within this work. These simulations should shed significant light on the behavior of NCs at different surface coverage and elucidate the physical blocking of NCs on a surface due to different NC orientations. These computational results will most likely provide key features that can be used to develop future experiments.

CHAPTER 8 CONCLUSIONS

The adsorption and desorption behavior of various anisotropic CdSe nanocrystals diffusing within nanofluidic channels has been studied as a function of the nanocrystal's aspect ratio (AR). The adsorption kinetics within the nanochannel system is transport limited and we have provided an appropriate two-site transport model that accounts for a first-order reversible adsorption process. To date, we believe this to be the first quantification of the equilibrium constants for a reversible adsorption process within nanochannels. We use an aprotic solution (toluene) to decouple the impact of the geometric factors on the NC's diffusion from that of electrostatic interactions. In our study we observe the NCs diffusing into toluene filled nanochannels, and after several days allow the NCs to out-diffuse into neat toluene. Our forward diffusion analysis indicates that a saturation concentration was achieved within a 100 hours of diffusion. The equilibrium concentration was between 4 to 40 times higher then the initial reservoir concentration, indicating NC wall adsorption within the nanochannels. The saturation concentration measured for ARs > 1 remained below the equivalent maximum surface adsorption coverage calculated for a close-packing arrangement and modified by a geometric obstruction term based on the random sequential adsorption (RSA) process for spherocylinders. These values should be of interest to the RSA modeling community, as very few systems for anisotropic NCs have been reported; the only comparable study is the protein fibrinogen. It was found, that AR 1 was in good agreement with the equivalent maximum surface adsorption coverage provided for spheres by previous RSA studies. This further validates the RSA process and our study presents experimental results to further challenge the progression of these simulations.

We also provide results from a reverse diffusion study in which we allowed the already diffused NCs, from the forward diffusion study, to then out-diffuse into neat toluene. By using a double-exponential curve to fit the reverse diffusion data, we were able to distinguish two desorption processes. In retrospect, our reverse diffusion methodology inherently allows us to collect critical data pertaining to the adsorption processes within nanochannels, previously unknown to the nanofluidic community. We believe that for the adsorption of AR 1 NCs, a crowding effect is likely happening on the surface, where the repulsive NC-NC interaction at high surface coverage places the adsorbed NCs at a higher energy state, leading NCs to quickly desorb. At low surface coverage, the NC-NC interaction is low, and the NCs are strongly adsorbed. For ARs > 1, an additional tethering process must also be considered. At high surface coverage the void space between NCs may only allow the tips of subsequently adsorbing NCs to tether to the surface, thus allowing for a weaker interaction with the surface. The reverse diffusion study further allows the two equilibrium constants ($K_{b,wk}$ and $K_{b,str}$) associated with the two desorption processes to be estimated. The two-site adsorption rates are implicitly included in the transport model and we further consider the adsorption constant to be similar between the two-states. This allowed us to fit the experimental forward diffusion profiles and solve for the average equilibrium coefficients, adsorption constant, desorption constants, and diffusion coefficient.

Our model's fitting of the experimental forward diffusion concentration profiles reveal some interesting phenomenon. First, the modeled $K_{b,wk}$ and $K_{b,str}$ appear to be a function of the AR, and would suggest that the shape of the NC also impacts the adsorption and desorption properties, especially in the case of a sphere (AR 1) and short

spherocylinders (AR ≤ 3). Secondly, the ratio of the equilibrium coefficients as the AR increases beyond 3 substantiates the lower population of tethered NCs on the surface. We believe that at ARs > 3 the dispersion force overtakes the attractive van der Waals force for the tethering of NCs, although higher AR NCs are needed to provide a more conclusive study of this phenomenon. In general as the NC's AR increases the diffusion coefficient decreases, and appears to correspond well with the equilibrium coefficient ratio. Although the provided transport model accounts for the adsorption of NCs within the nanochannels, the reported diffusion coefficients (D_c) are still 2-orders of magnitude lower then calculated diffusion coefficients for diffusion in an unconfined large volume. We suspect that at the entrance of the nanochannel an additional steric hindrance is responsible for the hindered diffusion coefficients and observed concentration partitioning.

We believe this study provides valuable insight and quantitative analysis on the adsorption and desorption kinetics for a general NC-silica interface. Our study further provides a fresh look at the governing transport properties of particles or molecules within a nanochannel. Although our nanochannel system is not specifically unique, the analysis and methodology provided within this report are clearly a step (or two) beyond the most current literature on the subject. Furthermore, we breach the long discussed subject of particle or molecule adsorption within nanochannels with substantial details provided by a rigorous transport model. Lastly, the knowledge regarding AR dependent diffusion of NCs in nanochannels has been significantly enhanced by the methodology and transport modeling results presented in this manuscript.

APPENDIX A STATISTICAL MODELING OF RODS IN A SLIT PORE

Originally Authored by Frank van Swol

Edited by Louis J. Tribby

A.1 Introduction

In this short report we consider the adsorption of rods inside a narrow slit pore. Experiments indicate that beyond a certain rod length (l) the adsorption, or average density ($\bar{\rho}$), of the rods is negligible. Here we will use statistical mechanics to address the problem and determine the dependence of the adsorption on the rod length. We find that for sufficiently narrow pores $\bar{\rho} \sim l^{-1}$ and the partitioning factor inside of a slit pore can be calculated.

A.2 Model of Hard Rods Confined to a Slit Pore

To represent the rods we will use the hard spherocylinder, a straight circular cylinder of diameter σ and length l capped at each end by a hemisphere of diameter σ. The physical, end-to-end, length of the spherocylinder is therefore $l + \sigma$. The rods are considered to be confined in a slit pore by two parallel hard walls, perpendicular to the z-axis, and separated by a distance H. For convenience, these walls will be placed at $z = 0$ and $z = H$, respectively, and the coordinate system is shown in Figure A-1.

The interaction between a rod and the walls is governed by a hard wall potential, $V_{ext}(z, \phi, \theta)$, which acts as a one-body external field. This external field is infinite when any part of the spherocylinder intersects the wall and zero otherwise. In other words, the

distance of closest approach for the spherical caps is the radius of the sphere, i.e. $\sigma/2$ and similarly, placing the rod's axis parallel to the wall, the closest approach is also $\sigma/2$.

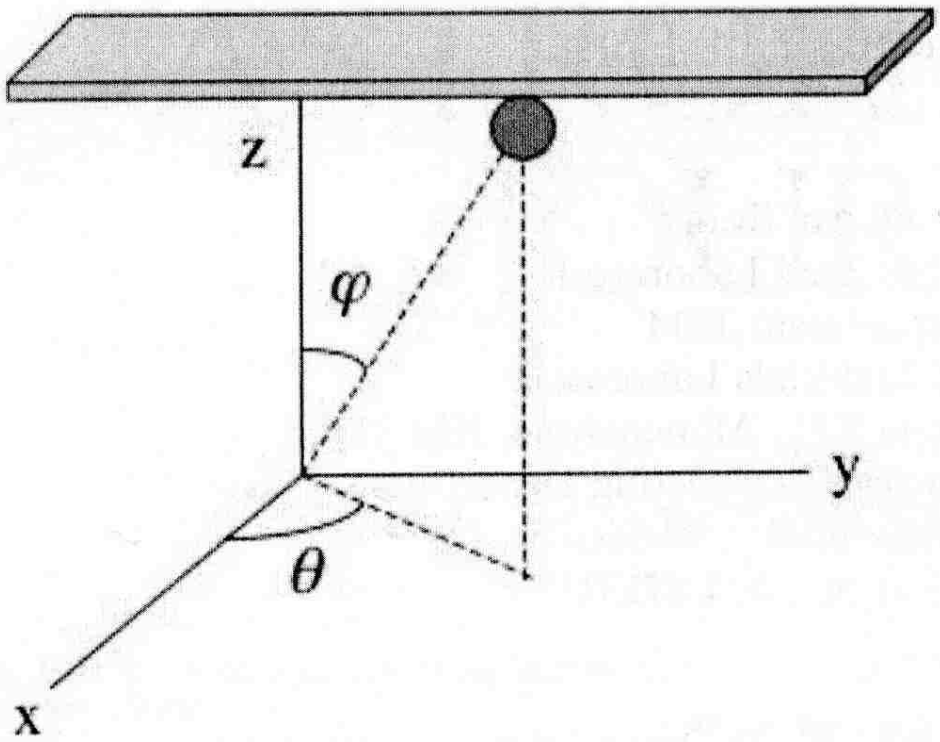

Figure A-1. The coordinate system used throughout this paper. The *z*-axis is taken as perpendicular to the plane's wall, while the *x*- and *y*-plane is parallel to the wall. The coordinates used to describe the orientation of the rod (denoted by a dashed line and a capping sphere, note that the spherocylinder's body is removed) are the zenith angle ϕ and the azimuth angle θ.

A.3 Expressing Densities as Volume Fractions

When reporting the density (ρ) of a fluid of hard particles (e.g. spheres, rods, or mixtures thereof) it is customary and convenient to represent this as the volume fraction (η). The volume fraction can be defined by the total volume V occupied by N number of hard particles. For example, for hard spheres of diameter σ, a single particle's volume is expressed as $V_p = \pi\sigma^3/6$, with the total volume of N spheres being $N\pi\sigma^3/6$. The resulting volume fraction can then be described by,

$$\eta = \frac{NV_p}{V} = \frac{N\pi\sigma^3/6}{V} = \frac{\pi}{6}\rho\sigma^3 \quad . \tag{A-1}$$

Similarly, for a spherocylinder of length l and diameter σ, i.e. aspect ratio $p \equiv l/\sigma$, the resulting volume fraction is,

$$V_p = \frac{\pi}{6}\sigma^3\left(1+\frac{3}{2}p\right) \quad . \tag{A-2}$$

The volume fraction is analogous to the volume's packing fraction, and is of sufficient means to judge the low versus high density behavior for spheres, although for non-spherical systems this may not be the case. An example of the latter case, is a fluid of hard infinitely thin lines of finite extent. Here, clearly $V_p = 0$ and hence η always vanishes. Yet, hard lines do become entangled as their density goes up and even though they manifestly take up no volume, they still exhibit non-ideal behavior such as hindered rotation. Therefore, in the case of rods it makes no sense to consider the volume fraction of the hypothetical object, rather, it is important to describe the out-scribed sphere or so-called "sphere of influence" (the volume over which one rod may influence another).

For spherocylinders, the out-scribed sphere has a diameter equal to $\sigma+l$ and hence the volume of this hypothetical particle is $V_p = \pi(\sigma+l)^3/6 = \pi\sigma^3(1+p)^3/6$. Thus, the packing fraction using the definition of the "sphere of influence" for spherocylinders can be expressed as,

$$\eta^* = \frac{\pi}{6}\rho\sigma^3(1+p)^3 = \eta\frac{(1+p)^3}{1+\frac{3}{2}p} \quad . \tag{A-3}$$

Equation A-3 indicates that for large p we expect $\eta^*/\eta \sim (2/3)p^2$, which can be considerably larger than unity. For example, for p = 10 and 20 we find $\eta^*/\eta \approx 80$ and 300, respectively. Roughly speaking, we need $\eta^* \leq 0.1$ for the assumption of ideal gas behavior to be valid. In the context of our NCs, we find our initial c_{bulk} to yield, by Eq. A-3, η^* values on the order of 10^{-3} to 10^{-4} when using the crystalline core dimensions. If we further consider the c_{sat} values as a freely floating concentration, then the η^* values are on the order of low 10^{-2} to 10^{-4}, and would suggest the NC system to be dilute enough to use ideal gas behavior within the model.

A.4 The Adsorption of Rods Inside a Slit Pore

We seek to determine the adsorption or, more appropriately, the average density ($\bar{\rho}$) of the rod-shaped particles inside the pore. Since we are interested in the situation where rods beyond a certain length appear to be absent from the pore, it is reasonable to use the ideal gas approximation to eliminate the rod-rod interactions. That is, inside the pore we can focus on an isolated rod, ignoring the possible interactions between rods. Notice, that the rod-wall interaction is still non-ideal, as it consists of the excluded volume wall-rod interaction defined above.

To solve the problem of finding the adsorption or the average density we must first find the density profile, $\rho(z)$, of the center of the rod as a function of z, the position along the direction normal to the wall. From this we can define the average density (using symmetry around $z = H/2$) simply as

$$\bar{\rho} = \frac{2}{H}\int_0^{H/2} dz\,\rho(z) \quad . \tag{A-4}$$

The most straight forward way to determine $\rho(z)$ is to use the Potential Distribution Theorem (PDT) due to the Widom, which for planar geometry reads as

$$\beta\mu = \beta\mu(z) = \ln \rho(z) - \ln < e^{-\beta U_t(z)} > \quad , \tag{A-5}$$

where $\beta = 1/\kappa T$ in which κ is the Boltzmann's constant and T is the absolute temperature, μ represents the chemical potential, and $U_t(z)$ is the energy of a test particle inserted with a random orientation and its center at position z. The angled brackets in Eq. A-5 denote an ensemble average. The PDT, which is generally valid at equilibrium, expresses the chemical potential as a constant, and also provides a generally applicable method for calculating that chemical potential that is often used in molecular simulations. In general, the energy U_t is the sum of interactions for the inserted rod with the walls, and the interactions with other rods present in the slit pore. In the present case, which focuses on the low density regime where we can use the ideal gas approximation, only the external field contributes, *i.e.*, $U_t(z) = V_{ext}(z)$.

The chemical potential (μ) that describes the equilibrium condition between the rods contained in the slit pore and the rods in the bulk reservoir (ρ_{bulk}) is generally related

through a bulk equation of state. Under the assumption of an ideal gas, which we believe to be true ($\eta^* << 0.1$), we simply have

$$\beta\mu = \ln \rho_{bulk} \quad . \tag{A-6}$$

We can further rewrite Eq. A-5 as an explicit expression for $\rho(z)$, as

$$\begin{aligned} \rho(z) &= e^{\beta\mu} < e^{-\beta U_t(z)} > \\ &= \rho_{bulk} < e^{-\beta U_t(z)} > \end{aligned} \quad . \tag{A-7}$$

However, our task is to determine the ensemble average of the Boltzmann factor of the insertion energy of a rod inserted at z, with a random orientation (θ, ϕ). For the slit pore at hand, the ensemble average amounts to an average taken over all possible orientations.

Before we proceed with the actual calculation of the quantity $< e^{-\beta U_t(z)} >$, or $\rho(z)/\rho_{bulk}$, it is worthwhile to sketch its basic behavior as function of z. Far from the wall, $U_t = V_{ext}$ will be zero for all orientations, and hence the average of the Boltzmann factor will be unity. For hard rods this will occur whenever $z > (\sigma + l)/2$. At the other extreme, $z < \sigma/2$, is inaccessible since the external field is infinite when the rod overlaps with the wall. For the intermediate region $\sigma/2 < z < (l + \sigma)/2$, the value of $< e^{-\beta U_t(z)} >$ will monotonically vary between 0 and 1, completing the three regions.

It is worthwhile to separately consider the two- and three-dimensional versions, as we shall do in the sections that follow. We will find that the exact 3D profile is, in fact, simpler than its 2D analog. For the 3D case the middle section, $\sigma/2 < z < (l + \sigma)/2$, is linear in the distance, z. In contrast, the middle section of the 2D profile is expressed in terms of the inverse sine function. Although perhaps at first sight somewhat surprising,

we note that it is not uncommon in statistical mechanics for 2D problems to be more challenging than 3D problems [A1].

A.5 Assumption of Isolated Rods

The approach to the density profile, and specifically in the form outlined above, assumes that we can treat the rods inside the pores as an ideal gas in an external field. Of course, neglecting rod-rod interactions is justified only when the average distance between rods is large compared to the diameter of the "sphere of influence" for the rods. For rods confined to a narrow slit pore it makes sense to examine the areal density, *i.e.* the number of rods per unit area (N/A). This quantity, a two-dimensional density which we denote as ρ_{2D}, is obtained directly from the integral of the profile $\rho(z)$, described by

$$\rho_{2D} = \frac{N}{A} \approx \int_0^H dz \rho(z) = H\bar{\rho} \quad . \tag{A-8}$$

We stress that this measure is only meaningful when the slit is sufficiently narrow, *i.e.*, when $H < l + \sigma$.

Finally, pursuing a line of argument similar to that given in regard to treating the 3D bulk solution as an ideal gas, the areal volume (or packing fraction) of the "disks of influence" is given by

$$\eta_{2D}^{*} = \frac{\pi}{4}\rho_{2D}\sigma^2(1+p)^2 \approx \frac{\pi}{4}H\bar{\rho}(1+p)^2 \quad . \tag{A-9}$$

It is this quantity that we need to be small (roughly ≤ 0.1) in order to be justified in neglecting rod-rod interactions.

A.6 2-Dimensional Slit Pores

In 2D, the problem simplifies as follows:

$$\begin{aligned} < e^{-\beta U_t(z)} > &= \int_0^{\pi/2} d\phi \; e^{-\beta V_{ext}(z,\phi)} \Big/ \int_0^{\pi/2} d\phi \\ &= \frac{2}{\pi} \int_0^{\pi/2} d\phi \; e^{-\beta V_{ext}(z,\phi)} \\ &= \frac{2}{\pi} \int_0^{\pi/2} d\phi \\ &= 1 - \frac{2}{\pi} \phi_m(z) \end{aligned} \tag{A-10}$$

Here, the zenith angle ϕ measures the angle between the spherocylinder's long body axis and the *z*-direction, which is taken to be perpendicular to the walls, see Figure A-1. Thus, $\phi = 0$ indicates an orientation perpendicular to the walls. The rod's symmetry, both ends being identical, implies that the maximum orientation we have to consider is $\phi = \pi/2$, or parallel to the wall. On the second line we explicitly make use of the fact that for hard body interactions, as we have here, the Boltzmann factor of the external field (V_{ext}) is either 1 (no wall overlap) or 0 (wall overlap). In other words, the integration over the orientation angle ϕ only extends from a minimum angle ϕ_m, which corresponds to a spherical cap touching the wall to $\pi/2$.

Thus, the entire calculation of the ensemble average term has been reduced to a straightforward geometrical problem, a determination of the minimum angle of rotation that still avoids overlap with the wall. Note that the minimum angle is a function of *z*, or more appropriately, $0 \le \phi_m(z) \le \pi/2$. Clearly, when $\phi_m(z) = \pi/2$ and $z = \sigma/2$, a spherocylinder is lying flat against the wall. Similarly, for sufficiently wide pores, or more specifically when $H > l + \sigma$, we obtain $\phi_m(z) = 0$ whenever $z \ge (l + \sigma)/2$. That is to

say that when a rod is sufficiently far away from the wall, the rod can have any orientation.

It is straightforward to show that the minimum angle can be expressed in terms of z, and the rod's physical dimensions (l and σ), by

$$\phi_m(z) = \begin{cases} \pi/2 & ;z \le \sigma/2 \\ \cos^{-1}\left(\dfrac{2z-\sigma}{l}\right) & ;\sigma/2 < z < (l+\sigma)/2 \\ 0 & ;z \ge (l+\sigma)/2 \end{cases} \quad . \qquad \text{(A-11)}$$

We have now obtained an explicit expression for the density profile. By using Eqs. A-7 and A-10, we have a continuous piece-wise profile, given by

$$\frac{\rho(z)}{\rho_{bulk}} = \begin{cases} 0 & ;z \le \sigma/2 \\ \dfrac{2}{\pi}\sin^{-1}\left(\dfrac{2z-\sigma}{l}\right) & ;\sigma/2 < z < (l+\sigma)/2 \\ 1 & ;z \ge (l+\sigma)/2 \end{cases} \quad , \qquad \text{(A-12)}$$

where it is understood that the maximum value of interest for a slit pore corresponds to the midpoint, $z = H/2$. Hence, if $H < l + \sigma$ we will not observe large z parts of the profile, such as $\rho(z) = \rho_{bulk}$, since the profile is "truncated" at $z = H/2 < (l + \sigma)/2$.

Equation A-12 can be integrated to produce the average density ($\bar{\rho}$) inside the pore (see Eq. A-4):

$$\frac{\bar{\rho}}{\rho_{bulk}} = \begin{cases} 0 & ;H \le \sigma \\ H^{-1}\left\{H - \sigma - \dfrac{2l}{\pi}\left[a\cos^{-1}(a) - \sqrt{1-a^2} + 1\right]\right\} & ;\sigma < H < l+\sigma \\ H^{-1}\left\{H - \sigma - \dfrac{2l}{\pi}\right\} & ;H > l+\sigma \end{cases} \qquad \text{(A-13)}$$

Where we used the shorthand notation $a = (H - \sigma)/l$.

A.7 3-Dimensional Slit Pores

In 3D, we need to consider an additional rotation around the z-axis, which is described by the azimuth angle θ. Using spherical coordinates, we express the ensemble difference as

$$\begin{aligned} < e^{-\beta U_i(z)} > &= \int_0^{\pi/2} d\phi \, sin\phi \int_0^{2\pi} d\theta e^{-\beta V_{ext}(z,\phi,\theta)} \;\; / \;\; \int_0^{\pi/2} d\phi \, sin\phi \int_0^{2\pi} d\theta \\ &= \frac{1}{2\pi} \int_0^{\pi/2} d\phi \, sin\phi \, e^{-\beta V_{ext}(z,\phi)} \int_0^{2\pi} d\theta \\ &= \frac{1}{2\pi} \int_{\phi_m(z)}^{\pi/2} d\phi \, sin\phi \int_0^{2\pi} d\theta \\ &= \int_{\phi_m(z)}^{\pi/2} d\phi \, sin\phi \\ &= \cos\phi_m(z) \end{aligned} \quad , \qquad \text{(A-14)}$$

where on the second line we explicitly make use of the cylindrical symmetry around the z-axis, *i.e.*, $V_{ext}(z, \phi, \theta) = V_{ext}(z, \phi)$. Furthermore, on the third line we use the fact that for hard interactions, as we have here, the Boltzmann factor of the external field is either 1 (no wall overlap) or 0 (wall overlap). As in the 2D case, the overlap condition depends solely on ϕ, and therefore the lower limit of the integration over ϕ is the minimum angle ϕ_m, which corresponds to the spherical cap touching the wall.

Finally, using Eq. A-11 to express $\phi_m(z)$ in terms of z, l, and σ, we obtain an exact expression for the piecewise profile,

$$\frac{\rho(z)}{\rho_{bulk}} = \begin{cases} 0 & ;z \le \sigma/2 \\ \left(\dfrac{2z-\sigma}{l} \right) & ;\sigma/2 < z < (l+\sigma)/2 \\ 1 & ;z \ge (l+\sigma)/2 \end{cases} \quad . \qquad \text{(A-15)}$$

To obtain the average density ($\bar{\rho}$, see Eq. A-4) we integrate the profile. Three different regimes exist: first $H \le \sigma$, followed by $\sigma < H \le l + \sigma$, and lastly $H > l + \sigma$. Performing the integration with respect to the $\bar{\rho}$, we find

$$\frac{\bar{\rho}}{\rho_{bulk}} = \begin{cases} 0 & ;H \le \sigma \\ \dfrac{(H-\sigma)^2}{2lH} & ;\sigma < H \le l+\sigma \\ \dfrac{(H-l/2-\sigma)}{H} & ;H > l+\sigma \end{cases} \quad . \qquad \text{(A-16)}$$

As expected, in the case of $H \to \infty$, we find that the $\bar{\rho} \to \rho_{bulk}$. From the above expression we conclude that for narrow pores, but wide enough to accommodate a rod, of fixed width the average density inside the pore varies as $\bar{\rho} \sim l^{-1}$. Our definition of the equilibrium partitioning coefficient between our NCs and the nanochannel dimensions falls in the third region ($H > l + \sigma$). Using the third region, we establish the equilibrium concentration (c_e) values that are plotted in the Results and Discussion chapter.

A.8 Continuous Potentials

For model rods that are not described by a discontinuous potential but by a continuous function V_{ext} (z, ϕ, θ), the ensemble average of Eq. A-7, and its more explicit forms Eqs. A-10 and A-14, has to be determined numerically. This can be done through quadrature methods such as Simpson's rule or, better still, Gaussian quadrature. Alternately, one can use a Monte Carlo method, *i.e.* sampling randomly over possible orientations ϕ, θ, at each position z, *via*,

$$\frac{\rho(z)}{\rho_{bulk}} \approx N_o^{-1} \sum_{\phi_k,\theta_k}^{N_o} e^{-\beta V_{ext}(z,\phi_k,\theta_k)} \quad , \qquad \text{(A-17)}$$

where the pair ϕ_k and θ_k denote the random orientation on the relevant interval, *i.e.*, $0 \le \phi_k \le \pi/2$ and $0 \le \theta_k \le \pi/2$, while N_o denotes the number of orientations sampled.

A.9 Molecular Scale Rods: The Lennard-Jones 9-3 Potential

To proceed we have to define an interaction between a rod and a planar wall. There exists a large variety of interaction potentials each of which is relevant to a different physical situation. For molecular scale rods that interact through dispersion (*i.e.*, van der Waals) forces, and in the absence of electrostatic charges, a pair wise Lennard-Jones (LJ) interaction potential is the function of choice. For an atom interacting with a wall that fills a half-space (*i.e.*, $z < 0$) the spatial integration of the standard LJ potential over all the wall atoms results in

$$\Phi_{9-3}(z) = \varepsilon_{wf}\sqrt{2/5}\left[\frac{1}{5}\left(\frac{\sigma_{wf}}{z}\right)^9 - \frac{3}{2}\left(\frac{\sigma_{wf}}{z}\right)^3\right] \quad . \tag{A-18}$$

Here, ε_{wf} denotes the strength of the interaction between a wall (*w*) atom and a fluid (*f*) atom, and σ_{wf} is the associated diameter.

We can use this potential in two ways. First, we can represent the rod by a collection of M interaction sites located at some position z_j along the axis of the rod. Hence, a rod with center-of-mass position z experiences an interaction with the wall that is given by a sum of sphere-wall interactions:

$$V_{ext}(z) = \sum_{j}^{M} \Phi_{9-3}(z_j) \quad . \tag{A-19}$$

Alternately, we can use the so-called Kihara potential which expresses the rod's interaction with the wall in terms of the shortest distance, z_s, between the rod's axis and the wall:

$$V_{ext}(z) = \Phi_{9-3}(z_s) \quad . \tag{A-20}$$

A.10 Nanoscale Rods: Hamaker's Approach

For a suspension of nanoscale rods, the relevant physical situation is a little more complicated than the problem of molecular rods interacting with a wall. That is, for a solution or suspension of nanoscale rods we must also account for the solvent. In a brute-force approach one would simply represent the solvent medium explicitly, *i.e.*, by explicit molecules/atoms. More traditionally, however, in modeling colloidal phenomena one seeks to avoid such a large number of solvent molecules and opt instead for an approach that is predicated on the idea that the solvent can be considered a 'spectator' species. The solvent's presence may be represented by a dielectric constant, and hence the nanorod-wall interaction is considered to be an effective interaction. For the case of van der Waals interactions, Hamaker proposed to integrate over all the atoms of the wall (similar to the discussion proceeding Eq. A-18) as well as the atoms of the object (*i.e.*, nano-sphere or rod), assuming an even distribution in both.

A.11 Orientation Distribution

Besides the density profile of the center of mass, one is often also interested in the orientation of the rods as a function of position, *z*. There exist various ways of expressing the orientation. A familiar one is the order parameter, *S*, used to characterize alignment along a so-called director. Depending on the dimensionality, *d*, the order parameter is

$$S = \begin{cases} \dfrac{<2\cos^2(\phi)-1>}{2} & ;d=2 \\ \dfrac{<3\cos^2(\phi)-1>}{2} & ;d=3 \end{cases} \quad . \tag{A-21}$$

For alignment along the *z*-axis, like all order parameters, it has been constructed to take the value of 1 for a complete alignment, and a value of 0 for a sample that exhibits no preferred direction, *i.e.*, one with random orientation. To characterize the orientation we often require the ensemble averages of the kind $< \cos^2(\phi) >$ as a function of *z*. For example, for hard rods in 3D we have (for $z > \sigma/2$),

$$\begin{aligned} <\cos^2(\phi)>(z) &= \int_0^{\pi/2} d\phi \int_0^{2\pi} d\theta \sin\phi \cos^2(\phi)\, e^{-\beta V_{ext}(z,\phi)} \Big/ \int_0^{\pi/2} d\phi \int_0^{2\pi} d\theta \sin\phi\, e^{-\beta V_{ext}(z,\phi)} \\ &= \int_0^{\pi/2} d\phi \sin\phi \cos^2(\phi) \Big/ \int_{\phi_m(z)}^{\pi/2} d\phi \sin\phi \\ &= \frac{1}{3}\cos^2(\phi_m(z)) \end{aligned} \tag{A-22}$$

Where we made use of the standard integral of $\int dx \sin x \cos^m x = -(m+1)^{-1}\cos^{m+1} x$.

Upon using Eq. A-11 to express $\phi_m(z)$ in terms of *z*, *l*, and σ, we obtain an exact expression for the orientation profile, *via*,

$$<\cos^2(\phi)>(z) = \begin{cases} \left(\dfrac{2z-\sigma}{l}\right)^2 \Big/ 3 & ;\sigma/2 < z < (l+\sigma)/2 \\ \dfrac{1}{3} & ;z \geq (l+\sigma)/2 \end{cases} \quad . \tag{A-23}$$

A.12 Monte Carlo Simulation

In general, the evaluation of the average $< e^{-U_i/kT} >$ requires either approximations or a numerical approach, *i.e.*, numerical integration. The latter can be quite easily accomplished with the Monte Carlo (MC) method. To start the MC simulation method for the problem at hand, one picks a position for the center of mass of the rod that lies between two parallel walls, and selects an orientation. The MC simulation then proceeds by making random displacements of the rod's center of mass and random changes in its orientation. Each time, the total energy is calculated for the new position and the change in energy $\Delta U = U_{new} - U_{old}$ is used to decide whether to accept the new position. For the Metropolis algorithm the acceptance is decided as follows. A random number from a uniform distribution, $\xi \in [0, 1]$, is compared to the Boltzmann factor of the energy change. The decision to accept/reject is then simply:

$$\begin{aligned} \xi &< e^{(-\Delta U/kT)};\ accept \\ \xi &\geq e^{(-\Delta U/kT)};\ reject \end{aligned} \quad . \tag{A-24}$$

Note that for a hard rod between two hard walls, this implies that a new position and/or orientation is rejected if and only if the rod in its new position/orientation overlaps with the wall. That follows easily since such a configuration leads to $\Delta U = \infty$ and hence $exp(-\Delta U/kT) = 0$, and any random number from the interval [0, 1] will be larger than zero. In general, the Metropolis scheme guarantees that the probability of observing any configuration is proportional to the Boltzmann factor of that configuration's energy.

The finite, but typically long list of configurations generated in a MC simulation (referred to as a Markov Chain) represents a 'trajectory' through phase space that is representative of phase space. That is, since there are far too many different

configurations or points in phase space to consider, we only include a subset of them. Thus, in an MC simulation we construct a sample that is representative of all of phase space, by visiting a large but finite number of configurations (or state points). We do this in such a way that any average taken over the finite set of visited configurations is representative of the ensemble average (the average that results from considering every state point). In other words, the more state points we visit, the closer the MC average is to the ensemble average. Structural and thermodynamic quantities are collected during a run by averaging over the density profile $\rho(z)$ that is constructed during the MC simulation and by collecting a histogram of the rods center of mass position along the z-axis.

A.13 Appendix A References

[A1] For instance, for the hard sphere fluid the Ornstein-Zernike integral equation with the Percus-Yevick closure has an exact solution in both 1D and 3D, but not in 2D.

[2] Lubachevsky, B.D., *How to Simulate Billards and Similar Systems*, J. Comp. Phys. **94**, 255, (1991).

APPENDIX B MATHEMATICA CODE: SINGLE SITE TRANSPORT MODEL

```
(* MODEL + Fitting of AR 1 developed for Single Site Adsorption,
Authored by Louis Tribby *)

data = Import[
   "C:\\Users\\LT\\Desktop\\MODELING\\Code update 9_20_2011\\AR1\\AR1 2_24_10 QD chipM
     Right side ALL DATA\\AR1 2_24_10 QD chipM Right ALL DATA.txt", "Table"];
(* Loads data to be examined *)

(* Importing data, converting to cm for distance,
and assigning each data set a unique name: 'DataXX' *)

data03 = {}; Table[If[data[[i, 2]] == "n", ,
  AppendTo[data03, {data[[i, 1]] * 10^(-4), data[[i, 2]]}]], {i, 2, Length[data]}];
data05 = {}; Table[If[data[[i, 2]] == "n", ,
  AppendTo[data05, {data[[i, 1]] * 10^(-4), data[[i, 3]]}]], {i, 2, Length[data]}];
data09 = {}; Table[If[data[[i, 2]] == "n", ,
  AppendTo[data09, {data[[i, 1]] * 10^(-4), data[[i, 4]]}]], {i, 2, Length[data]}];
data016 = {}; Table[If[data[[i, 2]] == "n", ,
  AppendTo[data016, {data[[i, 1]] * 10^(-4), data[[i, 5]]}]], {i, 2, Length[data]}];
data024 = {}; Table[If[data[[i, 2]] == "n", ,
  AppendTo[data024, {data[[i, 1]] * 10^(-4), data[[i, 6]]}]], {i, 2, Length[data]}];
data029 = {}; Table[If[data[[i, 2]] == "n", ,
  AppendTo[data029, {data[[i, 1]] * 10^(-4), data[[i, 7]]}]], {i, 2, Length[data]}];
data033 = {}; Table[If[data[[i, 2]] == "n", ,
  AppendTo[data033, {data[[i, 1]] * 10^(-4), data[[i, 8]]}]], {i, 2, Length[data]}];
data040 = {}; Table[If[data[[i, 2]] == "n", ,
  AppendTo[data040, {data[[i, 1]] * 10^(-4), data[[i, 9]]}]], {i, 2, Length[data]}];
data051 = {}; Table[If[data[[i, 2]] == "n", ,
  AppendTo[data051, {data[[i, 1]] * 10^(-4), data[[i, 10]]}]], {i, 2, Length[data]}];
data057 = {}; Table[If[data[[i, 2]] == "n", ,
  AppendTo[data057, {data[[i, 1]] * 10^(-4), data[[i, 11]]}]], {i, 2, Length[data]}];
data077 = {}; Table[If[data[[i, 2]] == "n", ,
  AppendTo[data077, {data[[i, 1]] * 10^(-4), data[[i, 12]]}]], {i, 2, Length[data]}];
data062 = {}; Table[If[data[[i, 2]] == "n", ,
  AppendTo[data062, {data[[i, 1]] * 10^(-4), data[[i, 13]]}]], {i, 2, Length[data]}];
data085 = {}; Table[If[data[[i, 2]] == "n", ,
  AppendTo[data085, {data[[i, 1]] * 10^(-4), data[[i, 14]]}]], {i, 2, Length[data]}];
data0100 = {}; Table[If[data[[i, 2]] == "n", ,
  AppendTo[data0100, {data[[i, 1]] * 10^(-4), data[[i, 15]]}]], {i, 2, Length[data]}];
data0103 = {}; Table[If[data[[i, 2]] == "n", ,
  AppendTo[data0103, {data[[i, 1]] * 10^(-4), data[[i, 16]]}]], {i, 2, Length[data]}];
data0108 = {}; Table[If[data[[i, 2]] == "n", ,
  AppendTo[data0108, {data[[i, 1]] * 10^(-4), data[[i, 17]]}]], {i, 2, Length[data]}];
data0112 = {}; Table[If[data[[i, 2]] == "n", ,
  AppendTo[data0112, {data[[i, 1]] * 10^(-4), data[[i, 18]]}]], {i, 2, Length[data]}];
data0120 = {}; Table[If[data[[i, 2]] == "n", ,
  AppendTo[data0120, {data[[i, 1]] * 10^(-4), data[[i, 19]]}]], {i, 2, Length[data]}];


Data = ListPlot[{data0112}, PlotStyle -> {Blue}, PlotStyle → PointSize[Large]];
(* 'Data' is used to plot the selected experimental data set *)
```

```
(* Parameter list *)
dc = N[1.1 * 10^(-9), 20] (* Diffusion Coefficient: cm^2/sec *);
ll = N[650 * 10^(-4), 20](* domain length, 2000um is our max viewing length: cm *);
(*  Origin fitting function: Cinlet = Csat*(1-Exp[-t/tau])  *)
Csat = 40.52; (* AVERAGE Saturation Concentration fitted to data: mg/cm^3*)
tau = 27.73 * 3600; (* AVERAGE Characteristic Time: sec*)
A1 = .904; (* Frank's Partioning Value: mg/cm^3 *)
A2 = Csat - A1; (* Concentration adsorbed to wall: mg/cm^3 *)
JL = .59; (* Talbot's fractional value for maximum surface coverage: a.u. *)
Sm = 73;
(*  Maximum site density of a monolayer calculated for QDs + Ligand Passivation *)
s9b[t, x] = Sm * JL - b9b[t, x]; (* Equivalent site concentration balance: mg/cm^3 *)
keq = 5.30; (* Equilibrium Coefficient: cm^3/mg*)
kdes = 1.6 * 10^-7; (* Desorption Constant: 1/sec*)


(* Simulation using the above parameters *)

sol9c[t_, x_] = c9b[t, x] /. Flatten[
    NDSolve[{∂t c9b[t, x] == dc * ∂x,x c9b[t, x] - kdes * (keq * c9b[t, x] * s9b[t, x] - b9b[t, x]),
      ∂t b9b[t, x] == kdes * (keq * c9b[t, x] * s9b[t, x] - b9b[t, x]), c9b[0, x] == 0,
      b9b[0, x] == 0, c9b[t, 0] == A1 * (1 - Exp[(-t / tau)]), c9b[t, ll] == 0},
     {c9b[t, x], b9b[t, x]}, {x, 0, ll}, {t, 112 * 3600, 112 * 3600},
     Method → "BDF", MaxStepFraction → 1 / 1000]];
sol9b[t_, x_] = b9b[t, x] /. Flatten[NDSolve[
     {∂t c9b[t, x] == dc * ∂x,x c9b[t, x] - kdes * (keq * c9b[t, x] * s9b[t, x] - b9b[t, x]),
      ∂t b9b[t, x] == kdes * (keq * c9b[t, x] * s9b[t, x] - b9b[t, x]), c9b[0, x] == 0,
      b9b[0, x] == 0, c9b[t, 0] == A2 * (1 - Exp[(-t / tau)]), c9b[t, ll] == 0},
     {c9b[t, x], b9b[t, x]}, {x, 0, ll}, {t, 112 * 3600, 112 * 3600},
     Method → "BDF", MaxStepFraction → 1 / 1000]];
sol9s[t_, x_] = s9b[t, x] /. Flatten[NDSolve[
     {∂t c9b[t, x] == dc * ∂x,x c9b[t, x] - kdes * (keq * c9b[t, x] * s9b[t, x] - b9b[t, x]),
      ∂t b9b[t, x] == kdes * (keq * c9b[t, x] * s9b[t, x] - b9b[t, x]), c9b[0, x] == 0,
      b9b[0, x] == 0, c9b[t, 0] == A2 * (1 - Exp[(-t / tau)]), c9b[t, ll] == 0},
     {c9b[t, x], b9b[t, x]}, {x, 0, ll}, {t, 112 * 3600, 112 * 3600},
     Method → "BDF", MaxStepFraction → 1 / 1000]];


(* SIMULATION RESULTS, Here we plot the individual componente and the total model *)
```

```
Sim015 = Plot[sol9c[112 * 3600, x], {x, 0, 11},
  PlotRange → All, PlotStyle → {Black, Dashed, Thick}]; Sim016 =
 Plot[sol9b[112 * 3600, x], {x, 0, 11}, PlotRange → All, PlotStyle → {Red, Dashed, Thick}];
Sim019 = Plot[sol9c[112 * 3600, x] + sol9b[112 * 3600, x], {x, 0, 11},
   PlotRange → All, PlotPoints → 2000, PlotStyle → {Purple, Dashed, Thick}];
Show[{Data, Sim015, Sim016, Sim019}, PlotRange → {{0, 11}, {0, 50}}]
```

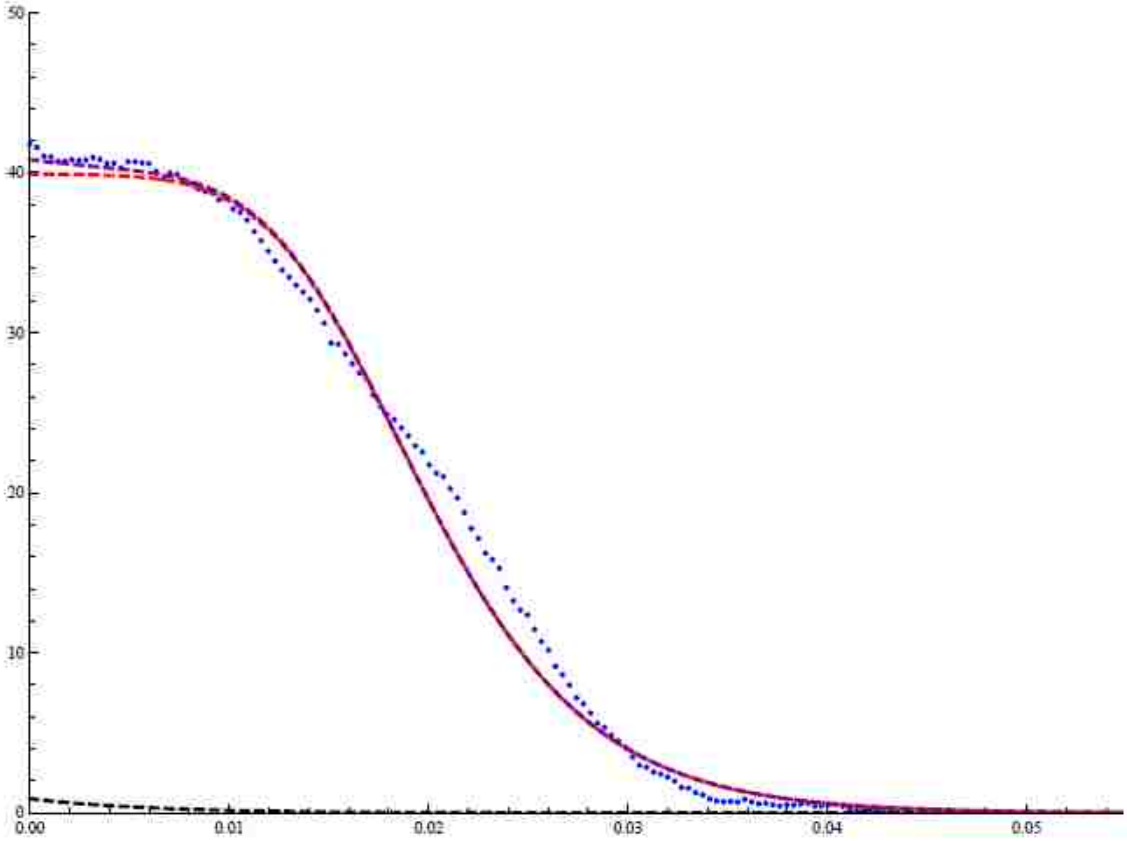


```
(* Above figure: solution to ∂t c9b[t,x]==dc*∂x,x c9b[t,x]+Rb[t,x];
Blue is the experimental data;
Black is the solved equilibrium concentration (ce);
Purple is the total concentration curve; *)
```

APPENDIX C MATHEMATICA CODE: TWO SITE TRANSPORT MODEL

```
(* MODEL + Fitting of AR 1 developed with 2-types of adsorption sitee,
Authored by Louis Tribby *)

data = Import[
    "C:\\Users\\LT\\Desktop\\MODELING\\Code update 9_20_2011\\AR1\\AR1 2_24_10 QD chipM
      Right side ALL DATA\\Kstr and Kwk\\AR1 2_24_10
      QD chipM Right ALL DATA.txt", "Table"];
(* loads data to be examined *)

(* Importing data, converting to cm for distance,
and assigning each data set a unique name: 'DataXX' *)

data03 = {}; Table[If[data[[i, 2]] = "n", ,
  AppendTo[data03, {data[[i, 1]] * 10^(-4), data[[i, 2]]}]], {i, 2, Length[data]}];
data05 = {}; Table[If[data[[i, 2]] = "n", ,
  AppendTo[data05, {data[[i, 1]] * 10^(-4), data[[i, 3]]}]], {i, 2, Length[data]}];
data09 = {}; Table[If[data[[i, 2]] = "n", ,
  AppendTo[data09, {data[[i, 1]] * 10^(-4), data[[i, 4]]}]], {i, 2, Length[data]}];
data016 = {}; Table[If[data[[i, 2]] = "n", ,
  AppendTo[data016, {data[[i, 1]] * 10^(-4), data[[i, 5]]}]], {i, 2, Length[data]}];
data024 = {}; Table[If[data[[i, 2]] = "n", ,
  AppendTo[data024, {data[[i, 1]] * 10^(-4), data[[i, 6]]}]], {i, 2, Length[data]}];
data029 = {}; Table[If[data[[i, 2]] = "n", ,
  AppendTo[data029, {data[[i, 1]] * 10^(-4), data[[i, 7]]}]], {i, 2, Length[data]}];
data033 = {}; Table[If[data[[i, 2]] = "n", ,
  AppendTo[data033, {data[[i, 1]] * 10^(-4), data[[i, 8]]}]], {i, 2, Length[data]}];
data040 = {}; Table[If[data[[i, 2]] = "n", ,
  AppendTo[data040, {data[[i, 1]] * 10^(-4), data[[i, 9]]}]], {i, 2, Length[data]}];
data051 = {}; Table[If[data[[i, 2]] = "n", ,
  AppendTo[data051, {data[[i, 1]] * 10^(-4), data[[i, 10]]}]], {i, 2, Length[data]}];
data057 = {}; Table[If[data[[i, 2]] = "n", ,
  AppendTo[data057, {data[[i, 1]] * 10^(-4), data[[i, 11]]}]], {i, 2, Length[data]}];
data077 = {}; Table[If[data[[i, 2]] = "n", ,
  AppendTo[data077, {data[[i, 1]] * 10^(-4), data[[i, 12]]}]], {i, 2, Length[data]}];
data082 = {}; Table[If[data[[i, 2]] = "n", ,
  AppendTo[data082, {data[[i, 1]] * 10^(-4), data[[i, 13]]}]], {i, 2, Length[data]}];
data085 = {}; Table[If[data[[i, 2]] = "n", ,
  AppendTo[data085, {data[[i, 1]] * 10^(-4), data[[i, 14]]}]], {i, 2, Length[data]}];
data0100 = {}; Table[If[data[[i, 2]] = "n", ,
  AppendTo[data0100, {data[[i, 1]] * 10^(-4), data[[i, 15]]}]], {i, 2, Length[data]}];
data0103 = {}; Table[If[data[[i, 2]] = "n", ,
  AppendTo[data0103, {data[[i, 1]] * 10^(-4), data[[i, 16]]}]], {i, 2, Length[data]}];
data0108 = {}; Table[If[data[[i, 2]] = "n", ,
  AppendTo[data0108, {data[[i, 1]] * 10^(-4), data[[i, 17]]}]], {i, 2, Length[data]}];
data0112 = {}; Table[If[data[[i, 2]] = "n", ,
  AppendTo[data0112, {data[[i, 1]] * 10^(-4), data[[i, 18]]}]], {i, 2, Length[data]}];
data0120 = {}; Table[If[data[[i, 2]] = "n", ,
  AppendTo[data0120, {data[[i, 1]] * 10^(-4), data[[i, 19]]}]], {i, 2, Length[data]}];


Data = ListPlot[{data0112}, PlotStyle -> {Orange}, PlotStyle → PointSize[Large]];
(*'Data' is used to plot the selected experimental data set *)
```

```
(* Parameter list *)
dc = N[3.4 * 10^(-8), 20] (* Diffusion Coefficient: cm^2/sec *);
ll = N[650 * 10^(-4), 20](* domain length, 2000 um is our max viewing length: cm *);
tau = 27.73 * 3600;
(* AVERAGE Characteristic Time Fit for Foward Diffusion Concentration: sec *)
Al = .904; (* Equilibrium Concentration = Frank's Partioning Value * Cbulk: mg/cm^3 *)
Sm = 73;
(* Maximum site density of a monolayer calculated for QDs + Ligand Passivation *)
JL = .62; (* Talbot's fractional value for maximum surface coverage: a.u. *)
sopn[t, x] = Sm * JL - b2str[t, x] - b2wk[t, x];
(* Equivalent site concentration balance: mg/cm^3 *)
keqstr = 8.3; (* Strong Site Equilibrium Coefficient: cm^3/mg *)
keqwk = 3.7; (* Weak Site Equilibrium Coefficient: cm^3/mg *)
ka = 2.6 * 10^-5; (* Adsorption constant,mg sec/cm^3 *)
(* We convert Keq and ka values into areal values by
 taking the nanochannel's corrosponding Volume/Area for a pixel *)


(* Simulation using the above parameters *)


solc[t_, x_] = c9b[t, x] /. Flatten[NDSolve[
     {∂t c9b[t, x] == dc * ∂x,x c9b[t, x] - ka * (c9b[t, x] * sopn[t, x] - (1 / keqstr) * b2str[t, x]) -
        ka * (c9b[t, x] * sopn[t, x] - (1 / keqwk) * b2wk[t, x]),
      ∂t b2str[t, x] == ka * (c9b[t, x] * sopn[t, x] - (1 / keqstr) * b2str[t, x]),
      ∂t b2wk[t, x] == ka * (c9b[t, x] * sopn[t, x] - (1 / keqwk) * b2wk[t, x]), c9b[0, x] == 0,
      b2str[0, x] == 0, b2wk[0, x] == 0, c9b[t, 0] == Al * (1 - Exp[(-t / tau)]), c9b[t, ll] == 0},
     {c9b[t, x], b2str[t, x], b2wk[t, x]}, {x, 0, ll}, {t, 112 * 3600, 112 * 3600},
     Method → "BDF", MaxStepFraction → 1 / 1000]];
solb2str[t_, x_] = b2str[t, x] /. Flatten[NDSolve[
     {∂t c9b[t, x] == dc * ∂x,x c9b[t, x] - ka * (c9b[t, x] * sopn[t, x] - (1 / keqstr) * b2str[t, x]) -
        ka * (c9b[t, x] * sopn[t, x] - (1 / keqwk) * b2wk[t, x]),
      ∂t b2str[t, x] == ka * (c9b[t, x] * sopn[t, x] - (1 / keqstr) * b2str[t, x]),
      ∂t b2wk[t, x] == ka * (c9b[t, x] * sopn[t, x] - (1 / keqwk) * b2wk[t, x]), c9b[0, x] == 0,
      b2str[0, x] == 0, b2wk[0, x] == 0, c9b[t, 0] == Al * (1 - Exp[(-t / tau)]), c9b[t, ll] == 0},
     {c9b[t, x], b2str[t, x], b2wk[t, x]}, {x, 0, ll}, {t, 112 * 3600, 112 * 3600},
     Method → "BDF", MaxStepFraction → 1 / 1000]];
solb2wk[t_, x_] = b2wk[t, x] /. Flatten[NDSolve[
     {∂t c9b[t, x] == dc * ∂x,x c9b[t, x] - ka * (c9b[t, x] * sopn[t, x] - (1 / keqstr) * b2str[t, x]) -
        ka * (c9b[t, x] * sopn[t, x] - (1 / keqwk) * b2wk[t, x]),
      ∂t b2str[t, x] == ka * (c9b[t, x] * sopn[t, x] - (1 / keqstr) * b2str[t, x]),
      ∂t b2wk[t, x] == ka * (c9b[t, x] * sopn[t, x] - (1 / keqwk) * b2wk[t, x]), c9b[0, x] == 0,
      b2str[0, x] == 0, b2wk[0, x] == 0, c9b[t, 0] == Al * (1 - Exp[(-t / tau)]), c9b[t, ll] == 0},
     {c9b[t, x], b2str[t, x], b2wk[t, x]}, {x, 0, ll}, {t, 112 * 3600, 112 * 3600},
     Method → "BDF", MaxStepFraction → 1 / 1000]];
solsopn[t_, x_] = sopn[t, x] /. Flatten[NDSolve[
     {∂t c9b[t, x] == dc * ∂x,x c9b[t, x] - ka * (c9b[t, x] * sopn[t, x] - (1 / keqstr) * b2str[t, x]) -
        ka * (c9b[t, x] * sopn[t, x] - (1 / keqwk) * b2wk[t, x]),
      ∂t b2str[t, x] == ka * (c9b[t, x] * sopn[t, x] - (1 / keqstr) * b2str[t, x]),
      ∂t b2wk[t, x] == ka * (c9b[t, x] * sopn[t, x] - (1 / keqwk) * b2wk[t, x]), c9b[0, x] == 0,
      b2str[0, x] == 0, b2wk[0, x] == 0, c9b[t, 0] == Al * (1 - Exp[(-t / tau)]), c9b[t, ll] == 0},
     {c9b[t, x], b2str[t, x], b2wk[t, x]}, {x, 0, ll}, {t, 112 * 3600, 112 * 3600},
     Method → "BDF", MaxStepFraction → 1 / 1000]];


(* SIMULATION RESULTS, Here we plot the individual components and the total model *)
```

```
Sim015 = Plot[solc[112 * 3600, x], {x, 0, 11},
   PlotRange → All, PlotStyle → {Black, Dashed, Thick}]; Sim016 =
 Plot[solb2str[112 * 3600, x], {x, 0, 11}, PlotRange → All, PlotStyle → {Red, Dashed, Thick}];
Sim017 = Plot[solb2wk[112 * 3600, x], {x, 0, 11},
    PlotRange → All, PlotStyle → {Blue, Dashed, Thick}];
Sim019 = Plot[solb2wk[112 * 3600, x] + solb2str[112 * 3600, x] + solc[112 * 3600, x],
    {x, 0, 11}, PlotRange → All, PlotPoints → 2000, PlotStyle → {Purple, Dashed, Thick}];
Show[{Data, Sim015, Sim016, Sim017, Sim019}, PlotRange → {{0, 11}, {0, 45}}]
```

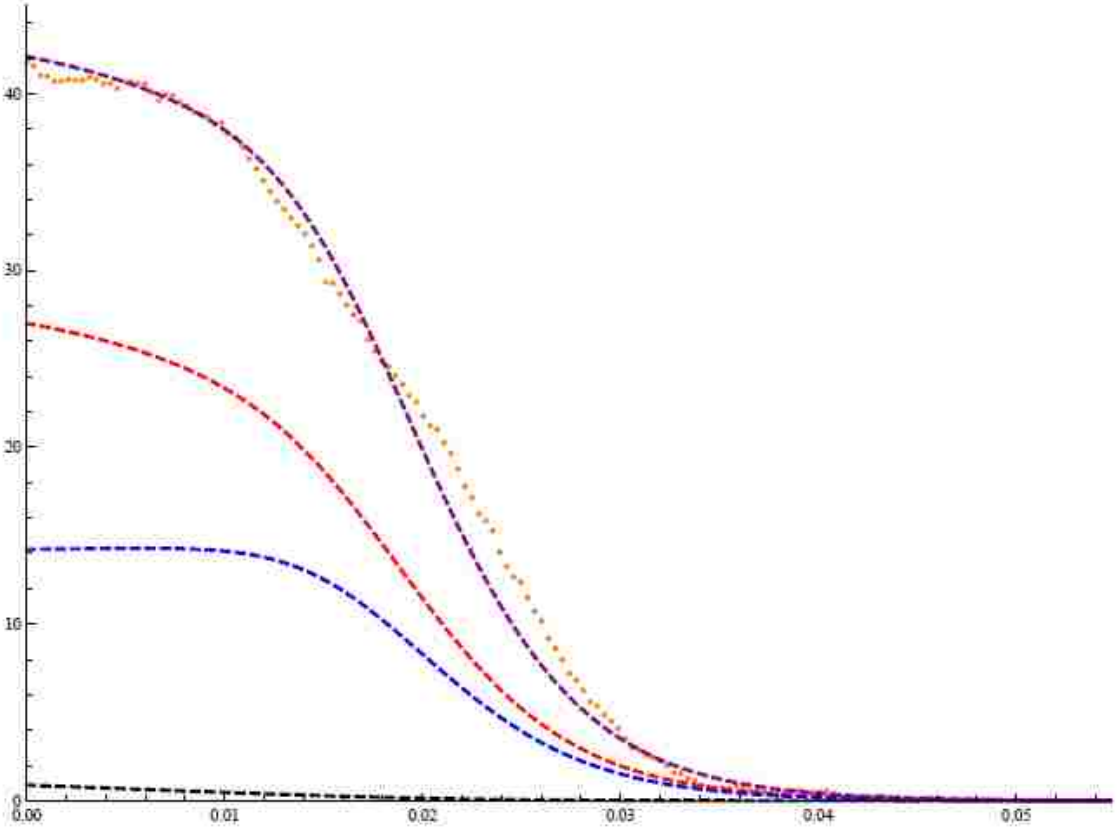


```
(* Above figure: Orange is the raw data;
Black is the solved equilibrium concentration;
Red is the Strongly Bound contribution;
Blue is the Weakly Bound contribution;
Purple is the Total Concentration Curve *)


(* To export the results *)

Export["AR1_2sitePIT_112hrsSim15.csv", Sim015];
Export["AR1_2sitePIT_112hrsSim16.csv", Sim016];
Export["AR1_2sitePIT_112hrsSim17.csv", Sim017];
Export["AR1_2sitePIT_112hrsSim19.csv", Sim019];
```

REFERENCES

1. **Hines, M.A. and P. Guyot-Sionnest, *Synthesis and Characterization of Strongly Luminescing ZnS-Capped CdSe Nanocrystals.* J. Phys. Chem., 1996. 100: p. 468.**
2. **Xie, R.G., et al., *Synthesis and characterization of highly luminescent CdSe-Core CdS/Zn0.5Cd0.5S/ZnS multishell nanocrystals.* J. Am. Chem. Soc., 2005. 127: p. 7480.**
3. **Susumu, K., et al., *Enhancing the stability and biological functionalities of quantum dots via compact multifunctional ligands.* J. Am. Chem. Soc., 2007. 129: p. 13987.**
4. **Medintz, I.L., et al., *Quantum dot bioconjugates for imaging, labelling and sensing.* Nat. Mater., 2005. 4: p. 435.**
5. **Wang, D.S., et al., *Superparamagnetic Fe2O3 Beads-CdSe/ZnS quantum dots core-shell nanocomposite particles for cell separation.* Nano Lett., 2004. 4: p. 409.**
6. **Mattoussi, H., et al., *Self-assembly of CdSe-ZnS quantum dot bioconjugates using an engineered recombinant protein.* J. Am. Chem. Soc., 2000. 122: p. 12142.**
7. **Colvin, V.L., M.C. Schlamp, and A.P. Alivisatos, *LIGHT-EMITTING-DIODES MADE FROM CADMIUM SELENIDE NANOCRYSTALS AND A SEMICONDUCTING POLYMER.* Nature, 1994. 370: p. 354.**
8. **McDonald, S.A., et al., *Solution-processed PbS quantum dot infrared photodetectors and photovoltaics.* Nat. Mater., 2005. 4: p. 138.**
9. **Klein, D.L., et al., *A single-electron transistor made from a cadmium selenide nanocrystal.* Nature, 1997. 389: p. 699.**
10. **Talapin, D.V. and C.B. Murray, *PbSe nanocrystal solids for n- and p-channel thin film field-effect transistors.* Science, 2005. 310: p. 86.**
11. **Somers, R.C., M.G. Bawendi, and D. D. G. Nocera, *CdSe nanocrystal based chem-/bio-sensors.* Chem. Soc. Rev., 2007. 36: p. 579.**
12. **Liu, Y.S., et al., *pH-sensitive photoluminescence of CdSe/ZnSe/ZnS quantum dots in human ovarian cancer cells.* J. Phys. Chem. C, 2007. 111: p. 2872.**
13. **Pinaud, F., et al., *Bioactivation and cell targeting of semiconductor CdSe/ZnS nanocrystals with phytochelatin-related peptides.* J. Am. Chem. Soc., 2004. 126: p. 6115.**
14. **Dubertret, B., et al., *In Vivo Imaging of Quantum Dots Encapsulated in Phospolipid Micelles* Science, 2002. 298: p. 1759.**
15. **Hoang, H.T., et al., *Analysis of single quantum-dot mobility inside 1D nanochannel devices.* Nanotech., 2011. 22: p. 275201.**
16. **Wu, Y., et al., *The development of quantum dot calibration beads and quantitative multicolor bioassays in flow cytometry and microscopy.* Anal. Biochem., 2007. 364: p. 180.**
17. **Tsay, J.M., S. Doose, and S. Weiss, *Rotational and Translational Diffusion of Peptide-Coated CdSe/CdS/ZnS Nanorods Studied by Fluorescence Correlation Spectroscopy.* J. Am. Chem. Soc., 2006. 128: p. 1639.**

18. **Manna, L., E.C. Scher, and A.P. Alivisatos, *Synthesis of Soluble and Processable Rod-, Arrow-, Teardrop-, and Tetrapod-Shaped CdSe Nanocrystals* J. Am. Chem. Soc., 2000. 122: p. 12700.**
19. **Piruska, A., et al., *Nanofluidics in chemical analysis.* Chem. Soc. Rev., 2010. 39: p. 1060.**
20. **Schoch, R.B., J. Han, and P. Renaud, *Transport phenomena in nanofluidics.* Rev. Mod. Phys., 2008. 80: p. 839.**
21. **Pappaert, K., et al., *Measurements of diffusion coefficients in 1-D micro- and nanochannels using shear-driven flows.* Lab Chip, 2005. 5: p. 1104-1110.**
22. **Srikar, R., A.L. Yarin, and C.M. Megaridis, *Fluidic delivery of homogeneous solutions through carbon tube bundles.* Nanotechnology, 2009. 20(27): p. 275706.**
23. **Griffiths, S.K. and R.H. Nilson, *Optimization of charged species separation by autogenous electric field-flow fractionation in nano-scale channels.* ELECTROPHORESIS, 2010. 31: p. 832-842.**
24. **Verbridge, S.S., et al., *Suspended glass nanochannels coupled with microstructures for single molecule detection.* J. Appl. Phys., 2005. 97: p. 124317.**
25. **Han, J., S.W. Turner, and H.G. Craighead, *Entropic Trapping and Escape of Long DNA Molecules at Submicron Size Constriction.* Phys. Rev. Lett., 1999. 83: p. 1688-1691.**
26. **Stavis, S.M., et al., *Single molecule studies of quantum dot conjugates in a submicrometer fluidic channel.* Lab Chip, 2005. 5: p. 337-343.**
27. **Reisner, W., et al., *Statics and Dynamics of Single DNA Molecules Confined in Nanochannels.* Phys. Rev. Lett., 2005. 94: p. 196101.**
28. **Schoch, R.B., A. Bertsch, and P. Renaud, *pH-Controlled Diffusion of Proteins with Different pI Values Across a Nanochannel on a Chip.* Nano Lett., 2006. 6(3): p. 543–547**
29. **Stavis, S.M., J. Geist, and M. Gaitan, *Separation and metrology of nanoparticles by nanofluidic size exclusion.* Lab on a Chip, 2010. 10: p. 2618-2621.**
30. **Oh, Y.J., et al., *Effect of wall–molecule interactions on electrokinetic transport of charged molecules in nanofluidic channels during FET flow control* Lab on a Chip, 2009. 9: p. 1601-1608.**
31. **Han, J. and H.G. Craighead, *Separation of Long DNA Molecules in a Microfabricated Entropic Trap Array.* Science, 2000. 288: p. 1026-1029**
32. **Schoch, R.B., H.v. Lintel, and P. Renaud, *Effect of the surface charge on ion transport through nanoslits.* Phys. Fluids, 2005. 17: p. 100604.**
33. **Bai, J.G., W.H. Yeo, and J.H. Chung, *Nanostructured biosensing platform—shadow edge lithography for high-throughput nanofabrication.* Lab Chip, 2009. 9: p. 449.**
34. **Cao, H., et al., *Fabrication of 10 nm enclosed nanofluidic channels.* Appl. Phys. Lett., 2002. 81: p. 174.**
35. **Chou, S.Y., P.R. Krauss, and P.J. Renstrom, *Imprint of sub-25 nm vias and trenches in polymers.* Appl. Phys. Lett., 1995. 67: p. 3114.**

36. Li, M., et al., Appl. Phys. Lett., 2000. 76: p. 673.
37. Zaumseil, J., et al., Nano Lett., 2003. 3: p. 1223.
38. Czaplewski, D.A., et al., *Nanofluidic channels with elliptical cross sections formed using a nonlithographic process.* Appl. Phys. Lett., 2003. 83: p. 4836.
39. Fan, R., et al., *Fabrication of Silica Nanotube Arrays from Vertical Silicon Nanowire Templates.* J. Am. Chem. Soc., 2003. 125: p. 5254.
40. Fan, R., et al., *DNA Translocation in Inorganic Nanotubes.* Nano Lett., 2005. 5: p. 1633.
41. Kievsky, Y.Y., et al., *Dynamics of molecular diffusion of rhodamine 6G in silica nanochannels.* J. Chem. Phys., 2008. 128: p. 151102.
42. Kievsky, Y. and I. Sokolov, *Self-Assembly of Uniform Nanoporous Silica Fibers.* IEEE Trans. Nanotech., 2005. 4: p. 490.
43. Khare, R., M.D. Graham, and J.J.d. Pablo, *Cross-Stream Migration of Flexible Molecules in a Nanochannel.* Phys. Rev. Lett., 2006. 96: p. 224505.
44. Keffer, D., A.V. McCormick, and H.T. Davis, *Unidirectional and single-file diffusion in AlPO4-5: Molecular dynamics investigations.* Mol. Phys., 1996. 87: p. 367.
45. Gruener, S. and P. Huber, *Knudsen Diffusion in Silicon Nanochannels.* Phys. Rev. Lett., 2008. 100: p. 064502.
46. Yamaguchi, A., et al., *Diffusion of Metal Complexes Inside of Silica-Surfactant Nanochannels within a Porous Alumina Membrane.* J. Phys. Chem. B, 2008. 112: p. 2024.
47. Fu, Y., et al., J. Phys. Chem. B, 2006. 110: p. 9164.
48. Etienne, M., et al., Chem. Mater., 2007. 19: p. 844.
49. Bottcher, H., P. Slowik, and W. Suss, *Sol-gel carrier systems for controlled drug delivery.* J. Sol-Gel Sci. Tech., 1998. 13: p. 277.
50. Chithrani, B.D. and W.C.W. Chan, *Elucidating the Mechanism of Cellular Uptake and Removal of Protein-Coated Gold Nanoparticles of Different Sizes and Shapes.* Nano Lett., 2007. 7: p. 1542.
51. Hibara, A., et al., *Nanochannels on a Fused-Silica Microchip and Liquid Properties Investigation by Time-Resolved Fluorescence Measurements.* Anal. Chem., 2002. 74: p. 6170.
52. Holt, J.K., et al., *Fast Mass Transport Through Sub-2-Nanometer Carbon Nanotubes.* Science, 2006. 312: p. 1034.
53. Hinds, B.J., et al., *Aligned multiwalled carbon nanotube membranes* Science, 2004. 303: p. 62.
54. Srikar, R., A.L. Yarin, and C.M. Megaridis, *Fluidic delivery of homogeneous solutions through carbon tube bundles.* Nanotech., 2009. 20: p. 275706.
55. Anderson, J.L. and J.A. Quinn, *Restricted transport in small pores.* Biophys. J., 1974. 14: p. 130.
56. Brenner, H. and L.J. Gaydos, *The constrained brownian movement of spherical particles in cylindrical pores of comparable radius: Models of the diffusive and convective transport of solute molecules in membranes and porous media.* J. Coll. Inter. Sci., 1977. 58: p. 312.

57. Okazaki, M. and K. Toriyama, *Inhomogeneous Distribution and Collective Diffusion of Solution Molecules in the Nanochannel of Mesoporous Silica.* J. Phys. Chem. B, 2003. 107: p. 7654.

58. Das, A., et al., *Single-File Diffusion of Confined Water Inside SWNTs: An NMR Study.* ACS Nano, 2010. 4: p. 1687.

59. Majolino, D., et al., *Water Diffusion in Nanoporous Glass: An NMR Study at Different Hydration Levels.* J. Phys. Chem. B, 2008. 112: p. 3927.

60. Meersmann, T., et al., *Exploring Single-File Diffusion in One-Dimensional Nanochannels by Laser-Polarized 129Xe NMR Spectroscopy.* J. Phys. Chem. A, 2000. 104: p. 11665.

61. Banerjee, A. and K.D. Kihm, *Experimental verification of near-wall hindered diffusion for the Brownian motion of nanoparticles using evanescent wave microscopy.* Phys. Rev. E, 2005. 72: p. 042101.

62. Hinze, G., G. Diezemann, and T. Basché, *Rotational Correlation Functions of Single Molecules.* Phys. Rev. Lett., 2004. 93: p. 203001.

63. Tatarkova, S.A. and D.A. Berk, *Probing single DNA mobility with fluorescence correlation microscopy.* Phys. Rev. E, 2005. 71: p. 041913.

64. Sullivan, K.D. and E.B. Brown, *Multiphoton fluorescence recovery after photobleaching in bounded systems.* Phys. Rev. E, 2011. 83: p. 051916.

65. Ortega, A. and J.G.d.l. Torre, *Hydrodynamic properties of rodlike and disklike particles in dilute solution* J. Chem. Phys., 2003. 119: p. 9914.

66. Goldman, A.J., R.G. Cox, and H. Brenner, *Slow viscous motion of a sphere parallel to a plane wall-I motion through a quiescent fluid* Chem. Eng. Sci., 1967. 22: p. 637.

67. Choi, C.K., C.H. Margraves, and K.D. Kihm, *Examination of near-wall hindered Brownian diffusion of nanoparticles: experimental comparison to theories by Brenner (1961) and Goldman et al (1967).* Phys. Fluids, 2007. 19: p. 103305.

68. Schoch, R.B., A. Bertsch, and P. Renaud, *pH-Controlled Diffusion of Proteins with Different pI Values Across a Nanochannel on a Chip.* Nano Lett., 2006. 6: p. 543

69. Ajdari, A. and L. Bocquet, *Giant Amplification of Interfacially Driven Transport by Hydrodynamic Slip: Diffusio-Osmosis and Beyond.* Phys. Rev. Lett., 2006. 96: p. 186102.

70. Karnik, R., et al., *Diffusion-Limited Patterning of Molecules in Nanofluidic Channels.* Nano Lett., 2006. 6: p. 1735.

71. Durand, N.F., et al., *Direct measurement of effective diffusion coefficients in nanochannels using steady-state dispersion effects.* Appl. Phys. Lett., 2007. 91: p. 203106.

72. Williams, D.B. and C.B. Carter, eds. *Transmission Electron Microscopy*. Basics I. 1996, Plenum Press: New York.

73. Mikroskopie, C.Z., *LSM 510 Laser Scanning Microscope*, in *Operating Manual*. 1998, Carl Zeiss Mikroskopie.

74. Brennan, J.G., et al., *The preparation of large semiconductor clusters via the pyrolysis of a molecular precursor.* J. Am. Chem. Soc., 1989. 111: p. 4141.

75. **Rossetti, R., et al.,** ***Size effects in the excited electronic states of small colloidal CdS crystallites.*** **J. Chem. Phys., 1984. 80: p. 4464.**
76. **Pavesi, L., et al.,** ***Optical gain in silicon nanocrystals.*** **Nature, 2000. 408: p. 440.**
77. **Law, M., J. Goldberger, and P.D. Yang,** ***Semiconductor nanowires and nanotubes.*** **ANNUAL REVIEW OF MATERIALS RESEARCH, 2004. 34: p. 83.**
78. **Greenham, N.C., X.G. Peng, and A.P. Alivisatos,** ***Charge separation and transport in conjugated-polymer/semiconductor-nanocrystal composites studied by photoluminescence quenching and photoconductivity*** **PHYSICAL REVIEW B, 1996. 54: p. 17628.**
79. **Nozik, A.J.,** ***Quantum dot solar cells.*** **PHYSICA E-LOW-DIMENSIONAL SYSTEMS & NANOSTRUCTURES, 2002. 14: p. 115.**
80. **McDonald, S.A., et al.,** ***Solution-processed PbS quantum dot infrared photodetectors and photovoltaics*** **Nat. Mater., 2005. 4: p. 138.**
81. **Jeltsch, K.F., et al.,** ***Efficiency Enhanced Hybrid Solar Cells Using a Blend of Quantum Dots and Nanorods.*** **Advanced Functional Materials, 2012. 22: p. 397.**
82. **Lovric, J., et al.,** ***Differences in subcellular distribution and toxicity of green and red emitting CdTe quantum dots.*** **JOURNAL OF MOLECULAR MEDICINE-JMM, 2005. 83: p. 377.**
83. **Tan, W.H., et al.,** ***Bionanotechnology based on silica nanoparticles.*** **Medical Research Reviews, 2004. 24: p. 621.**
84. **Sharrna, P., et al.,** ***Nanoparticles for bioimaging.*** **ADVANCES IN COLLOID AND INTERFACE SCIENCE, 2006. 123: p. 471.**
85. **Peng, X.G., et al.,** ***Shape control of CdSe nanocrystals.*** **Nature, 2000. 404: p. 59.**
86. **Dabbousi, B.O., et al.,** ***(CdSe)ZnS core-shell quantum dots: Synthesis and characterization of a size series of highly luminescent nanocrystallites.*** **JOURNAL OF PHYSICAL CHEMISTRY B, 1997. 101: p. 9463.**
87. **Yoffe, A.D.,** ***Semiconductor quantum dots and related systems: electronic, optical, luminescence and related properties of low dimensional systems.*** **Advances in Physics, 2001. 50: p. 1.**
88. **Bawendi, M.G., M.L. Steigerwald, and L.E. Brus,** ***The Quantum Mechanics of Larger Semiconductor Clusters*** **Annu. Rev. Phys. Chem., 1990. 41: p. 477.**
89. **Glotzer, S.C. and M.J. Solomon,** ***Anisotropy of building blocks and their assembly into complex structures.*** **Nature Materials, 2007. 6: p. 557.**
90. **Talapin, D.V., et al.,** ***CdSe and CdSe/CdS Nanorod Solids.*** **J. Am. Chem. Soc., 2004. 126: p. 12984.**
91. **Dabbousi, B.O., et al.,** ***Langmuir-Blodgett Manipulation of Size-Selected CdSe Nanocrystallites.*** **Chem. Mater., 1994. 6: p. 216.**
92. **Fritz, K.P., et al.,** ***Structural characterization of CdSe nanorods*** **J. Cryst. Gr., 2006. 293.**
93. **Lorenz, J.K. and A.B. Ellis, J. Am. Chem. Soc., 1998. 120: p. 10970.**
94. **Becerra, L.R., et al.,** ***Investigation of the surface morphology of capped CdSe nanocrystallites by 31P nuclear magnetic resonance*** **J. Chem. Phys., 1993. 100: p. 3297.**

95. Whitesides, G.M. and J.C. Love, *The Art of Building Small.* Sci. Am., 2001. 285: p. 32.
96. Mijatovic, D., J.C.T. Eijkel, and A. van den Berg, *Technologies for nanofluidic systems: top-down vs. bottom-up - a review.* Lab on a Chip, 2005. 5: p. 492.
97. Harnett, C.K., G.W. Coates, and H.G. Craighead, *Heat-depolymerizable polycarbonates as electron beam patternable sacrificial layers for nanofluidics.* J. Vac. Sci. Technol. B, 2001. 19: p. 2842.
98. Asoh, H., et al., *Fabrication of ideally ordered anodic porous alumina with 63 nm hole periodicity using sulfuric acid.* J. Vac. Sci. Technol. B, 2001. 19: p. 569.
99. Pearson, J.L. and D.R.S. Cumming, *A single-step process for making nanofluidic channels using electron beam lithography.* MICROELECTRONIC ENGINEERING, 2005. 78-79: p. 343.
100. Liu, C.Y., A. Datta, and Y.L. Wang, *Ordered anodic alumina nanochannels on focused-ion-beam-prepatterned aluminum surfaces* APPLIED PHYSICS LETTERS, 2001. 78: p. 120.
101. Cannon, D.M., et al., *Fabrication of single nanofluidic channels in poly(methylmethacrylate) films via focused-ion beam milling for use as molecular gates* APPLIED PHYSICS LETTERS, 2004. 85: p. 1241.
102. Thamdrup, L.H., A. Klukowska, and A. Kristensen, *Stretching DNA in polymer nanochannels fabricated by thermal imprint in PMMA.* NANOTECHNOLOGY, 2008. 19: p. 125301.
103. Liang, X.G., et al., *Single sub-20 nm wide, centimeter-long nanofluidic channel fabricated by novel nanoimprint Mold fabrication and direct imprinting.* NANO LETTERS, 2007. 7: p. 3774.
104. Black, C.T., et al., *Highly porous silicon membrane fabrication using polymer self-assembly.* J. Vac. Sci. Technol. B, 2006. 24: p. 3188.
105. Ho, R.M., et al., *Solvent-induced microdomain orientation in polystyrene-b-poly (L-lactide) diblock copolymer thin films for nanopatterning.* POLYMER, 2005. 46: p. 9362.
106. Zaidi, S.H. and S.R.J. Brueck, *MULTIPLE-EXPOSURE INTERFEROMETRIC LITHOGRAPHY.* J. Vac. Sci. Technol. B, 1993. 11: p. 658.
107. Garcia, A.L., et al., *Electrokinetic molecular separation in nanoscale fluidic channels.* Lab on a Chip, 2005. 5: p. 1271.
108. Poniewierski, A., *Ordering of hard needles at a hard wall.* Phys. Rev. E, 1993. 47: p. 3396.
109. Mao, Y., et al., *Density profile and thermodynamics of rod-like particles between parallel walls.* Mol. Phys., 1997. 92: p. 151.
110. Talbot, J., et al., *From car parking to protein adsorption: an overview of sequential adsorption processes.* Colloids and Surfaces A: Physicochem. Eng. Aspects, 2000. 165: p. 287.
111. Daniel, S.G., *The adsorption on metal surfaces of long chain polar compounds from hydrocarbon solutions.* Trans. Faraday Soc., 1951. 47: p. 1345.

112. Crisp, D.J., *The adsorption of alcohols and phenols from nonpolar solvents on to alumina.* J. Colloid Sci., 1956. 11: p. 356.
113. Kipling, J.J., ed. *Adsorption from Solutions of Non-Electrolytes*. 1965, Academic Press: London.
114. Seker, U.O.S., et al., *Assembly Kinetics of Nanocrystals via Peptide Hybridization* Langmuir, 2011. 27: p. 4867.
115. Schmitt, A., et al., *Interaction of Fibrinogen with a Solid Surfaces of Varying Charge and Hydrophobic-Hydrophilic Balance.* J. Colloid Interf. Sci., 1983. 92: p. 25.
116. Garcia de la Torre, J. and V.A. Bloomfield, *Hydrodynamic properties of comple, rigid, biological macromolecules: theory and applications.* Quarterly Rev. Biophys., 1981. 14: p. 81.
117. Schaaf, P., P. Dejardin, and A. Schmitt, *Reflectometry as a technique to study the adsorption of human fibrinogen at the silica solution interface.* Langmuir, 1987. 3: p. 1131.
118. Feder, J. and I. Giaever, J. Colloid Interf. Sci., 1980. 78: p. 144.
119. Feder, J., J. Theor. Biol., 1980. 87: p. 237.
120. Ramsden, J.J., Phys. Rev. Lett., 1993. 71: p. 295.
121. Bafaluy, F.J., et al., Phys. Rev. Lett., 1993. 70: p. 623.
122. Pagonabarraga, I. and J.M. Rubi, Phys. Rev. Lett., 1994. 73: p. 114.
123. Wojtaszczyk, P. and J.B. Avalos, Phys. Rev. Lett., 1998. 80: p. 754.
124. Liu, X., et al., J. Chromatogr. A, 2003. 988: p. 205.
125. Adamczyk, Z., J. Barbasz, and M. Ciesla, *Mechanisms of Fibrinogen Adsorption at Solid Substrates* Langmuir, 2011. 27: p. 6868.
126. Malmsten, M.J., Colloid Interface Sci., 1994. 166: p. 333.
127. Brash, J.L., et al., *Interaction of Fibrinogen with Solid Surfaces of varying charge and hydrophobic-hydrophilic balance.* J. Colloid Interf. Sci., 1983. 95: p. 28.
128. Baillou, N.D., J.C. Voegel, and A. Schmitt, *Adsorption of Human Albumin and Fibrinogen onto Heparin-like Materials.* Colloids and Surfaces, 1985. 16: p. 271.
129. Adamczyk, Z., et al., *Fibrinogen conformations and charge in electrolyte solutions derived fromDLS and dynamic viscosity measurements.* J. Colloid Interf. Sci., 2012. 385: p. 244.
130. Doolittle, R.F., Sci. Am., 1985. 245: p. 126.
131. Chithrani, B.D. and W.C.W. Chan, *Elucidating the Mechanism of Cellular uptake and removal of protein coated gold nanoparticles of different shapes and sizes.* Nano Lett., 2007. 7: p. 1542.
132. Min, Y., et al., *The role of interparticle and external forces in nanoparticle assembly.* Nat. Mater., 2008. 7: p. 527.
133. Kim, H.-Y., et al., *Van der Waals dispersion forces between dielectric nanoclusters.* Langmuir, 2007. 23: p. 1735.
134. Eisenthal, K.B., *Second Harmonic Spectroscopy of Aqueous Nano- and Microparticle Interfaces.* Chem. Rev., 2006. 106: p. 1462.
135. Ho, C.H., et al., *Optical anisotropy of ZnO nanocrystals on sapphire by thermoreflectance spectroscopy.* Optics Lett., 2007. 32: p. 2765.